

Master thesis

---

**Fine structure of the isovector giant dipole resonance in  $^{90}\text{Zr}$   
studied by gamma coincidence measurement**

ガンマ崩壊同時計測による  $^{90}\text{Zr}$  のアイソベクトル型  
巨大双極子共鳴の微細構造の研究

---



大阪大学  
OSAKA UNIVERSITY

SHOKEN NAKAMURA

FEBRUARY, 2018

DEPARTMENT OF PHYSICS  
GRADUATE SCHOOL OF SCIENCE  
OSAKA UNIVERSITY

---

## Abstract

Giant resonances (GRs) are collective and vibrational states which are observed in all the nuclei. They provide the bulk property of nuclei such as incompressibility and symmetry energy of nuclear matter. However their decay mechanism is not well understood yet.

We performed a gamma coincidence experiment to investigate the fine structure, that is related to the decay mechanism, of the isovector giant dipole resonance (IVGDR) in  $^{90}\text{Zr}$  at Research Center Nuclear Physics, Osaka university. The  $^{90}\text{Zr}$  target was excited by the inelastic scattering of a proton beam accelerated by Ring cyclotron up to 392 MeV, then the gamma ray from the IVGDR to the ground state was detected by eight large volume  $\text{LaBr}_3$  detectors. By analyzing the scattered proton with Grand Raiden magnetic spectrometer, excitation energy spectrum which covers the excitation energy of 6-30 MeV including the IVGDR was obtained. The branching ratio of the gamma decay to the ground state was deduced with a coincidence measurement between the Grand Raiden spectrometer and the large volume  $\text{LaBr}_3$  detectors. The large volume  $\text{LaBr}_3$  detectors were developed by Milano group. The author designed and constructed the gamma detector array called "Scylla". Reduced transition matrix element  $B(E1)$  and the ground state gamma decay width  $\Gamma_\gamma$  was extracted from the Coulomb excitation cross section. Combining the gamma decay branching ratio and the  $\Gamma_\gamma$ , the total decay width of the IVGDR was obtained.

Thanks to the high gamma ray detection efficiency and fast response of  $\text{LaBr}_3$  detectors, enough statistics were collected then total decay width was calculated as a function of excitation energy. This indicated the success of gamma coincidence measurement in the energy region above the particle decay threshold which was quite difficult before and suggested a new approach to the study of nuclear structure.

---

## Abstract

原子核には巨大共鳴と呼ばれる集団励起状態がある。原子核のバルクな性質が反映されるこの巨大共鳴を通して、核物質の圧縮率や対称エネルギーに関する数多くの研究がなされてきた。しかし、巨大共鳴の崩壊メカニズムやその微細構造はいまだによくわかっていない。

そこで、2018年7月、我々は大阪大学核物理研究センターにて $^{90}\text{Zr}$ のアイソベクター型巨大双極子共鳴の崩壊幅を求める実験を行った。392MeVに加速した陽子ビームを用いて $(p, p'\gamma)$ 反応により $^{90}\text{Zr}$ を巨大共鳴状態へと励起させ、そこから基底状態へ崩壊するガンマ線を $\text{LaBr}_3$ 検出器にて測定した。散乱陽子を散乱角 $0^\circ$ においてGrand Raidenスペクトロメータで解析することで巨大共鳴を含む6-30 MeV領域の励起エネルギースペクトルを得た。また、Grand Raidenとの同時計測により基底状態へのガンマ崩壊の確率を導出した。ガンマ線検出器としてはMilanoグループの開発した大型 $\text{LaBr}_3$ 検出器8台を使った。特に筆者は実験を遂行する当たって、テスト実験を行いそれに基づいて検出器架台を設計、開発してきた。さらに、クーロン励起断面積から換算遷移核率 $B(E1)$ および基底状態への $\gamma$ 崩壊幅を導出し、それとガンマ崩壊の確率から巨大共鳴の全崩壊幅を求めた。

$\text{LaBr}_3$ 検出器の高い検出効率と速い時間特性のおかげで、十分な統計を貯めることができ、巨大共鳴を含む励起エネルギー領域において全崩壊幅を励起エネルギーの関数として導出することができた。これは、従来の実験技術では困難とされてきた粒子崩壊閾値より高い励起エネルギー状態のガンマ線同時計測実験の成功を意味し、新たな核構造研究の可能性を示すものとなった。

# Contents

<b>1</b>	<b>Introduction</b>	<b>9</b>
1.1	Giant Resonances	9
1.1.1	What is a giant resonance?	9
1.1.2	Sum rule	10
1.2	Decay of GRs	12
1.2.1	The width $\Gamma$ of the resonance	12
1.2.2	Gamma decay of GRs	13
1.3	The purpose of this work	14
1.4	Experimental methods	15
1.4.1	Overview of experimental methods	15
1.4.2	Coulomb excitation	16
<b>2</b>	<b>Experimental Setup</b>	<b>20</b>
2.1	Overview of experimental setup	20
2.1.1	Beam line	20
2.1.2	Beam line polarimeter	21
2.2	Magnetic Spectrometer "Grand Raiden"	21
2.2.1	High resolution magnetic spectrometer Grand Raiden	21
2.2.2	Focal plane detector system	24
2.2.3	Sieve-slit measurements	25
2.2.4	Under-focus mode	26
2.3	$\gamma$ ray detector	27
2.3.1	Large volume LaBr <sub>3</sub> :Ce detector	27
2.3.2	Detector array "Scylla"	29
2.4	Trigger and data acquisition system	30
2.5	Targets	32
2.6	Summary of experimental conditions	33
<b>3</b>	<b>Analysis</b>	<b>34</b>
3.1	Analysis of Magnetic Spectrometer "Grand Raiden"	34
3.1.1	Beam current calibration	34
3.1.2	Track reconstruction	34
3.1.3	Efficiency of the VDCs	35
3.1.4	Calibration of the scattering angle and determination of the solid angle	36
3.1.5	Optical correction and energy calibration	38
3.1.6	Background subtraction	39
3.2	Analysis of $\gamma$ ray detectors	42
3.2.1	$\gamma$ ray energy calibration	42
3.2.2	Background subtraction	42
3.2.3	Estimation of the number of gamma ray using Geant4 simulation code	44
3.2.4	Confirmation of the simulated results and correction factor	47

---

<b>4</b>	<b>Results</b>	<b>52</b>
4.1	Extraction of B(E1) . . . . .	52
4.1.1	Double differential cross section of $(p, p')$ at zero degree . . . . .	52
4.1.2	Result of B(E1) . . . . .	53
4.2	$\gamma$ rays from the GDR . . . . .	57
4.2.1	Branching ratio of ground state $\gamma$ decay . . . . .	57
4.2.2	Total decay width . . . . .	59
<b>5</b>	<b>Discussion</b>	<b>61</b>
5.1	Binning effect . . . . .	61
5.2	Total decay width . . . . .	61
5.3	Isospin splitting . . . . .	62
<b>6</b>	<b>Summary and Outlook</b>	<b>64</b>
<b>A</b>	<b>Formalism of coulomb excitation</b>	<b>65</b>
A.1	Nuclear optical potential . . . . .	65
<b>B</b>	<b>Data table</b>	<b>66</b>
B.1	Grand Raiden spectrometer . . . . .	66
B.2	LaBr <sub>3</sub> detectors . . . . .	67
B.3	Coincidence data . . . . .	67

# List of Tables

2.1	Design specification of the Grand Raiden spectrometer. . . . .	22
2.2	Properties of the vertical drift chamber. . . . .	25
2.3	Basic performance of LaBr <sub>3</sub> and NaI. . . . .	28
2.4	List of targets. . . . .	32
2.5	Summary of experimental conditions. . . . .	33
3.1	Parameters for the excitation energy calibration of Grand Raiden spectrometer. The upper is the one before the tuning and the lower is the one after the tuning. . . . .	39
3.2	The population of the magnetic substates in 1 <sup>+</sup> state at 15.11 MeV in <sup>12</sup> C. [TAM00] . . . . .	49
3.3	Variables entering into Eq.(3.14). . . . .	50
4.1	Variables entering into Eq.(4.1), and their values. . . . .	52
4.2	Variables entering into Eq.(4.4). . . . .	57
B.1	Parameters for optical correction of $\theta_c$ . . . . .	66
B.2	Parameters for optical correction of $y_c$ . . . . .	66
B.3	Parameters for energy calibration of LaBr <sub>3</sub> detectors. . . . .	67

# List of Figures

1.1	Photo-absorption cross-section for $^{124}\text{Sn}$ . [BER75]	9
1.2	Schematic representation of various collective modes drawn referencing [HAR01]. Orange, light blue and gray indicate protons, neutrons and both of them, respectively.	10
1.3	Integrated photo-absorption cross-section in units of TRK sum rule [BER75].	12
1.4	Schematic view of the decay process of a GR. [HAR01]	12
1.5	The ground state gamma coincidence yield for 84 MeV/u $^{17}\text{O}$ scattering on $^{208}\text{Pb}$ .	13
1.6	Coulomb excitation cross section obtained from $(p, p')$ data. [TAM11] Small peaks are observed in the low energy region of the GR.	14
1.7	$^{90}\text{Zr}$ level scheme. The red arrow indicates the neutron decay and the vertical black arrow represents the E1 transition.	15
1.8	Simplified experimental setup.	16
1.9	The projectile is scattered by coulomb interaction with the target nucleus.	17
1.10	The virtual photon number per solid angle for $E_\gamma=16$ MeV caused by 392 MeV protons scattered on $^{90}\text{Zr}$ .	18
2.1	Overview of the RCNP cyclotron facility.	20
2.2	The top view of horizontally placed BLP.	21
2.3	Overview of Grand Raiden and focal plane detector system in zero degree measurement.	22
2.4	Setups around the scattering chamber in the zero degree mode and in the finite angle mode are drawn. The sieve-slit is explained in the Sec.2.2.3.	23
2.5	Layout of the GR detector system.	24
2.6	The structure of VDC. The dotted lines indicate paths of the liberated electrons by the charged particles.	24
2.7	Design of a sieve-slit.	26
2.8	Vertical ion optics for off-focus mode.	27
2.9	Large volume $\text{LaBr}_3$ detector and the crystal [GIA13].	27
2.10	Internal BG in $\text{LaBr}_3$ .	29
2.11	Sideview of Scylla with $\text{LaBr}_3$ detectors.	29
2.12	Scylla top view	30
2.13	DAQ diagram for Grand Raiden.	31
2.14	DAQ diagram for $\text{LaBr}_3$ .	31
2.15	DAQ diagram for coincidence logic.	32
2.16	Target ladder with targets and a viewer.	33
3.1	Drift time to length conversion.	35
3.2	Tracking efficiency as a function of the excitation energy. Horizontal uncertainty is large due to the less accuracy of the position determined by the plastic scintillator.	36
3.3	Coordinate system at the target position.	36
3.4	Coordinate system at the focal plane.	37
3.5	Horizontal scattering angle at the target position.	37
3.6	Scattering angle distribution in the E398 experiment [OUI17].	38

3.7	Optical correction of Grand Raiden spectrometer . . . . .	38
3.8	Excitation energy spectrum in $^{12}\text{C}(p, p')$ at zero degree after optical and kinematical corrections, and energy calibration. . . . .	39
3.9	The left (right) panel is the corrected (uncorrected) spectrum of vertical position $y$ for the $^{12}\text{C}(p, p')$ . The data of $^{90}\text{Zr}$ target was difficult to see the difference due to the bad S/N ratio. . . . .	40
3.10	Corrected vertical position distribution for different excitation energy in the $^{90}\text{Zr}(p, p')$ . . . . .	41
3.11	Excitation energy spectrum in $^{90}\text{Zr}$ gated on the background (black) and true (red) events. Above the excitation energy of 20 MeV, the narrower gate was applied (see Fig.3.10). Therefore the number of event . . . . .	41
3.12	Excitation energy spectrum in $^{90}\text{Zr}(p, p')$ after background subtraction. . . . .	42
3.13	LaBr <sub>3</sub> timing spectrum for slot number 1. . . . .	43
3.14	Gamma ray spectra gated on each timing gate. . . . .	43
3.15	Gamma ray spectrum after BG subtraction . . . . .	43
3.16	Coincidence matrix between Grand Raiden and LaBr <sub>3</sub> in the $^{90}\text{Zr}(p, p')$ . . . . .	44
3.17	Ground state gamma decay energy spectrum. . . . .	44
3.18	Geometry in Geant4 simulation. The geometry was loaded through the CADMesh[POO12]. 45	
3.19	Fitting result in the case of 15.11 MeV gamma ray from the carbon target. The data is summed up by all of detectors, slot 1-8. . . . .	46
3.20	Trend of fitting parameter $b$ for the gamma rays from the $1^+$ state at 15.11 MeV in $^{12}\text{C}$ . . . . .	47
3.21	The right panel is the data from [GIA13] and the left panel is the current simulated efficiency. . . . .	47
3.22	Gamma ray spectrum of $^{60}\text{Co}$ taken by the slot number 1. . . . .	48
3.23	Comparison between the simulated efficiency and the experimental data. . . . .	49
3.24	The angular distribution of emitted gamma ray from the $1^+$ state at 15.11 MeV in $^{12}\text{C}$ . . . . .	50
3.25	Trend of correction factor for slot number 1. . . . .	51
3.26	Averaged correction factor for each slot number. . . . .	51
4.1	Double differential cross section in $^{90}\text{Zr}(p, p')$ at zero degree and full angular acceptance of the spectrometer. . . . .	53
4.2	Distribution of the averaged number of virtual photons in $^{90}\text{Zr}(p, p')$ in $\theta_{cm} = 0-3$ degree. . . . .	54
4.3	Separation of the E1 excitation cross section in $^{90}\text{Zr}$ by MDA [IWA12]. . . . .	55
4.4	BG distribution in $^{96}\text{Mo}(p, p')$ at zero degree by MDA [MAR13]. . . . .	55
4.5	B(E1) in $^{90}\text{Zr}$ obtained from a cross section of coulomb excitation. . . . .	56
4.6	Comparison between the preset resulted photo-absorption cross section and that from the $(\gamma, xn)$ experiment that is shaded with light orange.[BER75] . . . . .	57
4.7	Branching ratio of the ground state gamma decay. . . . .	58
4.8	Zoomed branching ratio of the ground state gamma decay. . . . .	58
4.9	Total decay width in the IVGDR of $^{90}\text{Zr}$ . . . . .	59
4.10	Total decay width in the IVGDR of $^{90}\text{Zr}$ zoomed in the lower energy region. . . . .	60
5.1	Total decay width in $^{90}\text{Zr}$ and double differential cross section as a function of the excitation energy. . . . .	62
5.2	Cross section of $^{89}\text{Y}(p, \gamma)$ reaction. Fine structure in the 14-18 MeV is the isobaric analog states of $^{90}\text{Y}$ . [HAS73] . . . . .	63
5.3	Cross section of $^{90}\text{Zr}(e, e'p)$ reaction. $(\gamma, p)$ means $(e, e'p)$ and $(\gamma, p_0)$ is obtained from the data of $^{89}\text{Y}(p, \gamma)$ . $(\gamma, n)$ cross section is plotted together for comparison. [SHO75] . . . . .	63
B.1	Fitting result in $^{90}\text{Zr}(p, p'\gamma)$ . The horizontal axis is gamma ray energy in MeV and the vertical axis is the counts/200 keV. . . . .	69

---

# Chapter 1

## Introduction

### 1.1 Giant Resonances

#### 1.1.1 What is a giant resonance?

Giant resonance (GR) is a collective and vibrational mode of nuclei. If a nucleus is excited in an appropriate condition, it can vibrate. The GR is a general property of the nuclear matter and is not a characteristic phenomenon of some specific nuclei. Actually the GR is observed in the nucleus in a broad mass range of  $A=3\sim 238$  [BER75]. That indicates that studying about GRs is a powerful tool to investigate properties of nuclear matter such as incompressibility and symmetry energy. For example, our group has deduced the electric dipole polarizability by using the spectrum of GRs and estimated the neutron skin thickness in  $^{208}\text{Pb}$  [TAM11].

Historically, GRs were observed in the research of photo-nuclear reactions. One of the experimental data is shown in Fig.1.1 and the large bump in Fig.1.1 corresponds to the GR. This large bump was understood by Goldhaber and Teller in 1948 [GOL48] as a vibrational mode in which neutrons and protons are oscillating in the opposite phase, that is called the isovector giant dipole resonance (IVGDR).

Besides the IVGDR, other types of GRs exist and they are classified with their quantum numbers, transfer angular momentum  $\Delta L$ , spin transfer  $\Delta S$  and isospin transfer  $\Delta T$ . Fig.1.2 shows the classification of GRs.

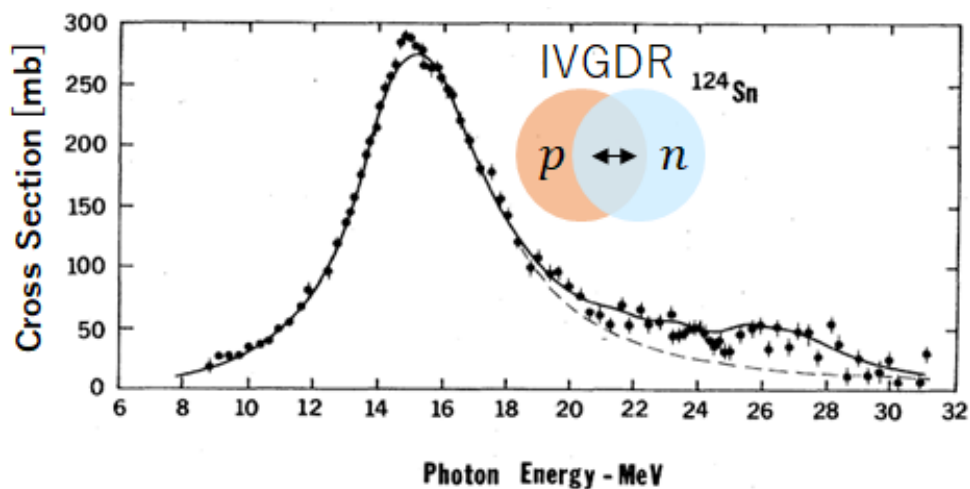


Figure 1.1: Photo-absorption cross-section for  $^{124}\text{Sn}$ . [BER75]

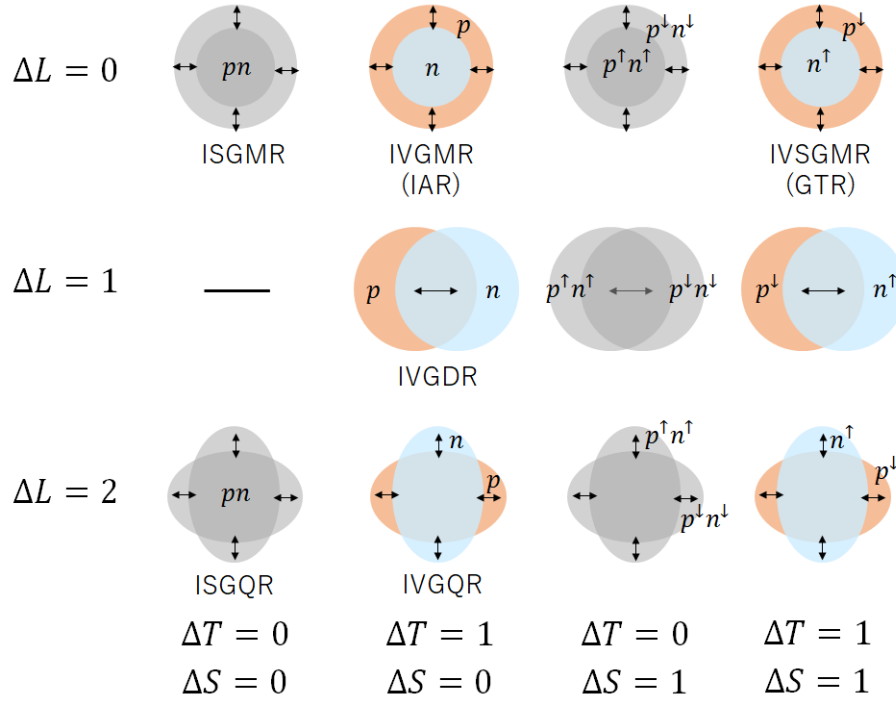


Figure 1.2: Schematic representation of various collective modes drawn referencing [HAR01]. Orange, light blue and gray indicate protons, neutrons and both of them, respectively.

### 1.1.2 Sum rule

The reason why we call this collective modes as giant resonance is that these modes exhaust most of the transition strength. Here I will show how to get the total transition strength, sum rule. First, I define a transition operator  $\hat{F}$  and the hamiltonian of the system  $\hat{H}$  given by,

$$\begin{aligned}\hat{H} &= \hat{T} + \hat{V} \\ &= \sum_k^A \frac{\hat{p}_k^2}{2m} + \hat{V}(\hat{r}_1, \dots, \hat{r}_A).\end{aligned}\quad (1.1)$$

If the interaction  $\hat{V}$  is the function of only  $r$ , it commutes with the operator  $\hat{F}$ , namely  $[\hat{H}, \hat{F}] = 0$ . By using the completeness of states  $\sum_f |\psi_f\rangle \langle \psi_f| = 1$ , the energy weighted sum rule is defined as,

$$\begin{aligned}S_1 &= \sum_f |\langle \psi_f | \hat{F} | \psi_i \rangle|^2 (E_f - E_i) \\ &= \frac{1}{2} \langle \psi_i | [\hat{F}, [\hat{H}, \hat{F}]] | \psi_i \rangle,\end{aligned}\quad (1.2)$$

where  $|\psi_{i(f)}\rangle$  and  $E_{i(f)}$  are the initial (final) state and their energy eigenvalues, respectively. Next I will show the result of E1 transition strength as one of examples. Here the operator must be modified in order to remove the spurious motion of the center of mass of the nucleus. Consequently the E1 operator is given by,

$$\hat{F}(E1) = e \left[ \frac{N}{A} \sum_i^Z r_{p_i} Y_1^0(p_i) - \frac{Z}{A} \sum_i^N r_{n_i} Y_1^0(n_i) \right], \quad (1.3)$$

where the  $p_i(n_i)$  denotes the  $i$ th proton (neutron) and  $Y_\lambda^\mu$  is the spherical harmonics. By using the commutator relation  $[\hat{x}, \hat{p}^2] = -2i\hbar$ , the energy weighted sum rule  $S_1(E1)$  is given by,

$$S_1(E1) = \frac{3}{4\pi} \frac{e^2 \hbar^2}{2m} \frac{NZ}{A}. \quad (1.4)$$

Moreover this sum rule can be rewritten in other ways, namely the reduced transition probability and the photo-absorption cross section. They are formalized by,

$$\begin{aligned} B(\pi l) &= \frac{1}{2l_i + 1} \left| \langle \psi_{l_f} \parallel \hat{F}_l \parallel \psi_{l_i} \rangle \right|^2 \\ &= \frac{2l + 1}{2l_i + 1} \sum_{m_i, m_f} \left| \langle \psi_{l_f m_f} \mid \hat{F}_l^m \mid \psi_{l_i m_i} \rangle \right|^2, \end{aligned} \quad (1.5)$$

$$\sigma_\gamma^{\pi l}(E_\gamma) = \frac{(2\pi)^3 (l + 1)}{l[(2l + 1)!!]^2} \left( \frac{E_\gamma}{\hbar c} \right)^{2l-1} \frac{dB(\pi l)}{dE_\gamma}, \quad (1.6)$$

where  $l_{i(f)}$  and  $m_{i(f)}$  represent the orbital angular momentum and its z-component of the initial (final) state. From Eq.1.2, Eq.1.4 and Eq.1.5, the sum rule in the  $B(E1)$  expression is given,

$$\begin{aligned} \int (E - E_0) \frac{dB(E1)}{dE} dE &\simeq \sum_f \frac{E_f - E_i}{2l_i + 1} \left| \langle \psi_{l_f} \parallel \hat{F}_1 \parallel \psi_{l_i} \rangle \right|^2 \\ &= \sum_{l_f} \sum_{m_i, m_f} \frac{2\lambda + 1}{2l_i + 1} (E_f - E_i) \left| \langle \psi_{l_f m_f} \mid \hat{F}_\lambda \mid \psi_{l_i m_i} \rangle \right|^2 \\ &= \frac{3}{2l_i + 1} \sum_{m_i} \frac{1}{2} \langle \psi_{l_i m_i} \mid [\hat{F}, [\hat{H}, \hat{F}]] \mid \psi_{l_i m_i} \rangle \\ &= \frac{9}{4\pi} \frac{e^2 \hbar^2}{2m} \frac{NZ}{A} \\ &= 14.9 \cdot \frac{NZ}{A} \text{ MeV e}^2 \text{ fm}^2. \end{aligned} \quad (1.7)$$

From Eq.1.2, Eq.1.4 and Eq.1.6, one can rewrite the sum rule in terms of the photo-absorption cross section  $\sigma_\gamma^{E1}(E_\gamma)$ ,

$$\begin{aligned} \int \sigma_\gamma^{E1}(E_\gamma) dE_\gamma &= \frac{16\pi^3}{9\hbar c} \times \int (E - E_0) \frac{dB(E1)}{dE} dE \\ &= 2\pi^2 \frac{\hbar e^2}{mc} \frac{NZ}{A} \\ &\simeq 60 \cdot \frac{NZ}{A} \text{ MeV} \cdot \text{mb}. \end{aligned} \quad (1.8)$$

This result is known as the Thomas-Reich-Kuhn (TRK) sum rule. Up to here I didn't assume any specific model except  $V$  is the function of only  $r$ , that means the sum rule is a general consequence of quantum mechanics. This value can be one of powerful references to confirm experimental result. As I mentioned above, GRs exhaust most of this transition strength. If you integrate the cross section of GRs, it is expected to be almost same as the sum rule (Fig.1.3). Strictly speaking, however, the above sum rule must be modified because the nucleon-nucleon interaction depends on the charge and momentum of nucleons. Taking into account the correction factor  $\kappa$ , the sum rule for the photo-absorption cross section is rewritten as,

$$S_1(E1) = 2\pi^2 \frac{\hbar e^2}{mc} \frac{NZ}{A} (1 + \kappa) \text{ MeV} \cdot \text{fm}^2. \quad (1.9)$$

Experimentally, the correction factor  $\kappa$  was deduced to be  $\sim 0.2$  [BER75]. However this story is not always the case. For example, the Gamow Teller transition strength is not occupied fully by GR strength, that consumes just roughly 60% of all strength. This is known as the "Gamow Teller quenching problem" and there are still plenty of discussions about this.

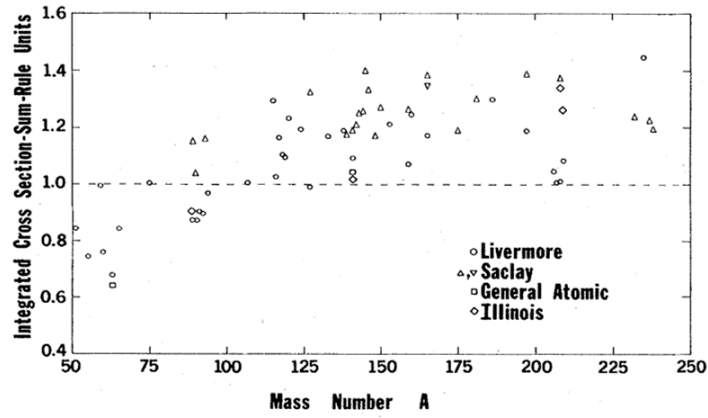


Figure 1.3: Integrated photo-absorption cross-section in units of TRK sum rule [BER75].

## 1.2 Decay of GRs

### 1.2.1 The width $\Gamma$ of the resonance

The large width of the GRs indicates that the GRs decay into other states immediately. Most of the GRs lie above the particle decay threshold. Thus the main decay channel is the particle decay and especially the neutron decay is dominant in heavy nuclei because the proton decay is suppressed by the Coulomb barrier. This is why the  $(\gamma, xn)$  cross section is often regarded as the photo absorption cross section in the region of the excitation energy of GRs.

Microscopically, the decay process consists of the following three components,

$$\Gamma = \Delta\Gamma + \Gamma^\uparrow + \Gamma^\downarrow, \quad (1.10)$$

where  $\Gamma$  is the total decay width of GRs.  $\Delta\Gamma$  is called the Landau damping which describes the coupling of collective particle hole states with the non-collective particle-hole states in the same excitation energy region.  $\Gamma^\uparrow$  is called escape width which describes the decay width for a particle emission.  $\Gamma^\downarrow$  is called spreading width which describes the damping into the more complex multiparticle-multihole configurations finally reaching the compound nucleus. Fig.1.4 shows a schematic view of the GR decay. Since the collective 1p-1h state is the entrance to the damping into the other more complex states, the 1p-1h state is called the doorway state (2p-2h is called the hallway state). There exists particle decay process not only from the doorway state but also from the pre-equilibrium states before reaching the compound nucleus. Such a process is indicated as  $\Gamma^\downarrow$  in Fig.1.4.

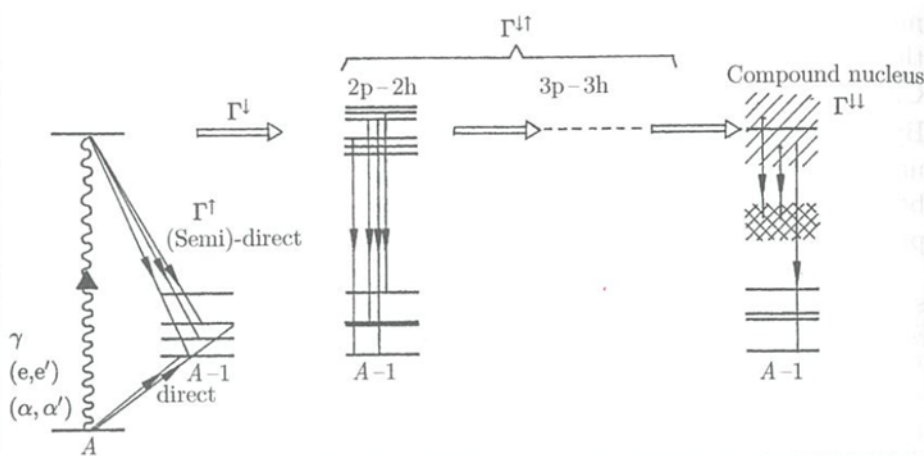


Figure 1.4: Schematic view of the decay process of a GR. [HAR01]

A measurement of particle decay provides the decay mechanism of GRs. For example, the energy spectrum of decay neutron from the GRs in  $^{90}\text{Zr}$  was studied [BLO94]. They compared the neutron energy spectra with the theoretical calculation based on the statistical decay model, that is related to the decay from the compound nucleus. Then they concluded that the escape width is a small fraction of total decay width, 5-10% in  $^{90}\text{Zr}$ . Nowadays, it is known that the spreading width is dominant for heavy nuclei and other components like Landau damping and escape width is the minor contributions.

### 1.2.2 Gamma decay of GRs

In addition to the particle decay mentioned above section, the gamma decay is another possible decay channel and it can reveal different aspects of GRs. The experimental difficulty is its extremely small decay probability because the GRs appears above the particle emission threshold. Early work about the gamma decay from the IVGDR was done by Beene *et al.* [BEE90]. They excited the target nucleus  $^{208}\text{Pb}$  by an  $^{17}\text{O}$  beam. The gamma rays were measured with a coincidence between the NaI gamma ray detectors and the silicon detectors which were used for the detection of scattered  $^{17}\text{O}$  particles. The obtained cross section of gamma decay to the ground state is shown in Fig.1.5.

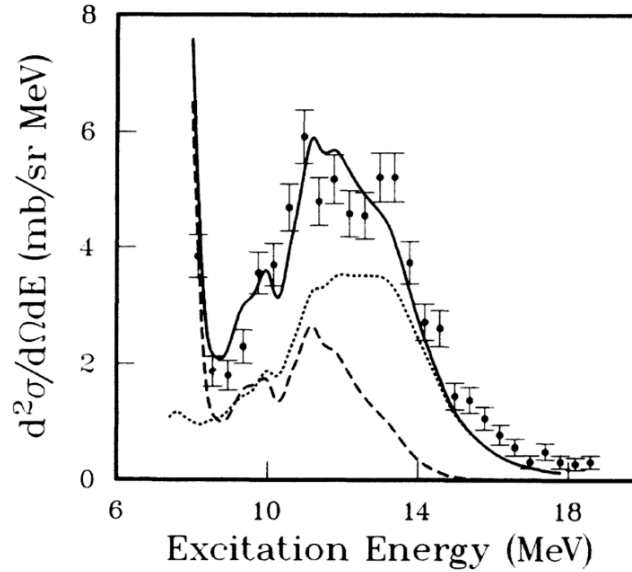


Figure 1.5: The ground state gamma coincidence yield for 84 MeV/u  $^{17}\text{O}$  scattering on  $^{208}\text{Pb}$ , compared with the theoretical calculations. See the text for the detail [BEE90].

They explained the spectrum by fitting the data with

$$\sigma_{x,x'\gamma_0}(E) = \sigma_{x,x'}(E) \left[ \frac{\Gamma_{\gamma_0}}{\Gamma} + \frac{\Gamma^\downarrow}{\Gamma} B_{CN}(E) \right], \quad (1.11)$$

where  $\Gamma_{\gamma_0}$  is the width of the direct gamma decay to the ground state from the doorway state and  $B_{CN}(E)$  is the gamma decay branching ratio from the compound nucleus. Total width gamma was obtained from the photo-absorption data. Here it is assumed that the direct gamma decay branching ratio  $\frac{\Gamma_{\gamma_0}}{\Gamma}$  is constant, namely independent of the excitation energy. The solid curve is the full result of calculations using Eq.1.11, the dotted curve gives the separate contribution of the first (direct) term in Eq.1.11 and the dashed line gives the contribution of the second (compound) term in Eq.1.11 [BEE90]. Since for heavy nuclei  $\Gamma^\downarrow$  is much bigger than  $\Gamma^\uparrow$ , they assumed  $\frac{\Gamma^\downarrow}{\Gamma}$  to be unity.  $B_{CN}(E)$  was derived by a statistical decay model of the compound nucleus (CN). The compound nucleus gamma decay is normally negligible but  $^{208}\text{Pb}$  showed different behavior. Since the  $^{208}\text{Pb}$  is doubly magic nucleus

and the excitation energy is relatively lower, the density of state for neutron decay is small. Thus the contribution from the CN is not so small. As increasing the excitation energy, the density of state for neutron decay is increased and the gamma decay probability from the CN,  $B_{CN}(E)$  decreases (dashed line in Fig.1.5). They also discussed the isospin mixing in the ISGQR in  $^{208}\text{Pb}$  via the same experiment [BEE90].

Another motivation for the research about gamma decay is the fact that the recent high energy resolution experiment indicated the fine structure of GRs [TAM11]. If the GR has internal structure in the large bump, the decay behavior should be accordingly changed. Thus, the message is that studying the gamma decay is a powerful tool to investigate the decay mechanism and the fine structure of GRs.

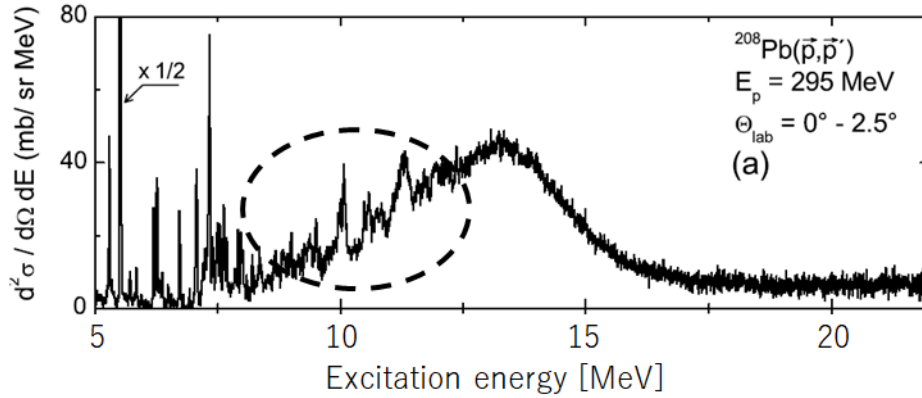


Figure 1.6: Coulomb excitation cross section obtained from  $(p, p')$  data.[TAM11] Small peaks are observed in the low energy region of the GR.

### 1.3 The purpose of this work

An early work about the gamma decay of the IVGDR in  $^{208}\text{Pb}$  done by Beene et al. [BEE90] was presented in the previous section. However, they couldn't observe the IVGDR peak separately because of the bad energy resolution of detectors for the scattered particles. Therefore they assumed that the gamma decay branching ratio is constant over the range of the IVGDR. This assumption is never obvious because the internal fine structure in the IVGDR was indicated by Tamii et al. [TAM11].

In order to investigate the fine structure of the IVGDR, experimental difficulties need to be overcome. The experimental key points were

- clean GDR spectrum
- an efficient gamma ray detection system.

These conditions were implemented by recent technical developments, a proton inelastic scattering at forward angles [TAM09] and the large volume  $\text{LaBr}_3$  detector [GIA13]. Detailed explanation about the experimental setup will be given in the following section. These developments allow us to research the hidden structure of the IVGDR in more detail. One of approaches is to study the energy dependence of the gamma decay branching ratio on the excitation energy. Moreover, we aimed to deduce the total decay width of the IVGDR as a function of the excitation energy. Those studies have never been done before.

Lastly, this thesis was devoted to present

- a technical development for a gamma coincidence measurement
- a deduction of the branching ratio the ground state gamma decay from the IVGDR and interpretation of the results.

## 1.4 Experimental methods

### 1.4.1 Overview of experimental methods

In the present experiment  $^{90}\text{Zr}$  was chosen as the main target for several reasons.

1. High neutron separation energy

The neutron separation energy in  $^{90}\text{Zr}$  is 11.97 MeV and the two neutron separation energy is 21.29 MeV. This is thought to be a big advantage because the neutron decay channel may be restricted then the gamma decay probability can be increased.

2. Neutron magic number

The number of neutrons in  $^{90}\text{Zr}$  is 50 which is the magic number. The theoretical calculation can be performed with less uncertainty.

3. Decay to excited states

The first and second excited states are  $1^+$  at 1.761 MeV and  $2^+$  at 2.186 MeV (Fig.1.7). The E1 gamma decay from the IVGDR to those excited states is also possible, and it can tell further information. However, if those states lay at small excitation energy, the analysis will be complicated because the separation of the ground state decay and the decays to those low lying excited states will be difficult.

4. Different isospin states in GDR

The isospin-upper GDR is predicted around excitation energy of 20-22 MeV. The neutron decay to the ground state of daughter nucleus from the isospin-upper state is isospin forbidden (Fig.1.7). This can change the gamma decay probability drastically.

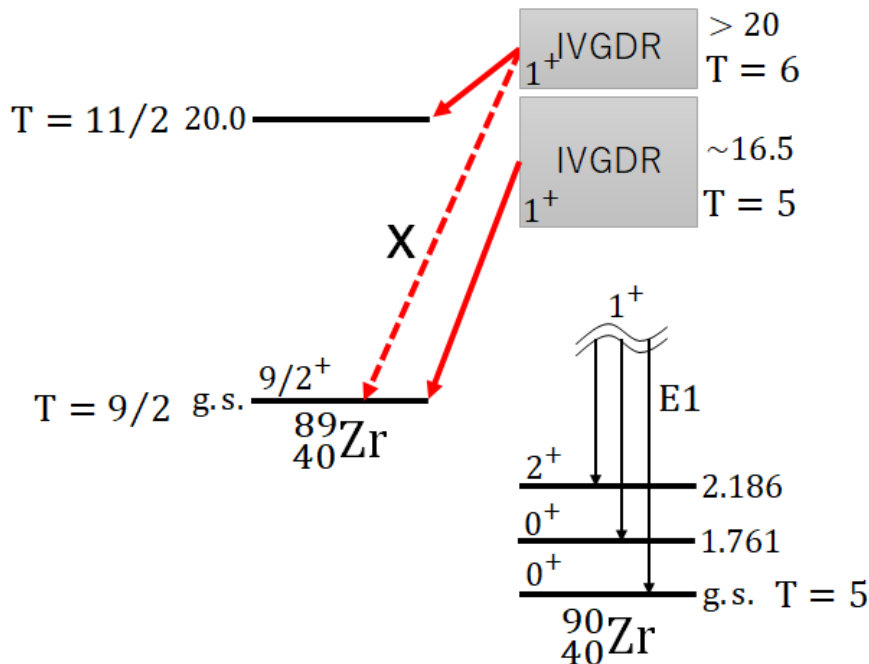


Figure 1.7:  $^{90}\text{Zr}$  level scheme. The red arrow indicates the neutron decay and the vertical black arrow represents the E1 transition.

The  $^{90}\text{Zr}$  target was excited by a proton beam through a Coulomb excitation. The detailed explanation about the Coulomb excitation will be given in the following section. The scattered proton was bent by Grand Raiden magnetic spectrometer and was detected by Multi Wire Drift Chamber (MWDC), then the excitation energy spectrum of  $^{90}\text{Zr}$  was obtained. The gamma ray from the excited zirconium was detected by  $\text{LaBr}_3:\text{Ce}$  detectors. The experiment was performed with a coincidence between

gamma ray detectors LaBr<sub>3</sub>:Ce and the Grand Raiden spectrometer. A simplified experimental setup is depicted in Fig.1.8.

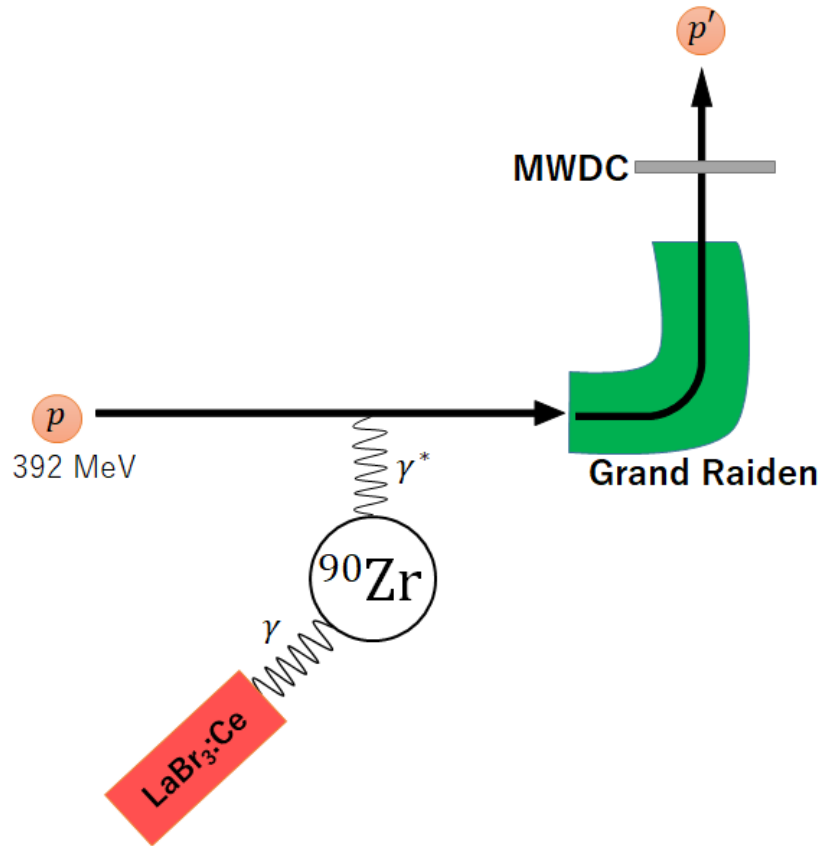


Figure 1.8: Simplified experimental setup.

#### 1.4.2 Coulomb excitation

The purpose of this section is to formulate the virtual photon method to deduce the reduced matrix element such as  $B(E1)$  from the  $(p, p')$  experiment. The Coulomb excitation cross section which is obtained from the experimental data directly consists of the reaction mechanism part and the intrinsic nuclear structure part of the target nucleus. Our interest is the nuclear structure, so the reaction mechanism part is calculated based on the model and then the nuclear structure part, the reduced matrix element, is extracted. One of the method to extract the structure from the coulomb excitation experiment is known as the virtual photon method. This model assumes that the virtual photon is exchanged between the incident particle and the target nucleus and the virtual photon excites the target nucleus. Therefore the reaction part is described as the number of virtual photons.

Let us start from calculating the scattering amplitude of the coulomb excitation. Consider a situation in which the field of the projectile, nucleus 1, excites the target, nucleus 2. The direction of the two nuclei is along the  $z$ -axis. Then in the first order perturbation theory, Distorted Wave Born Approximation (DWBA) provides the following scattering amplitude.

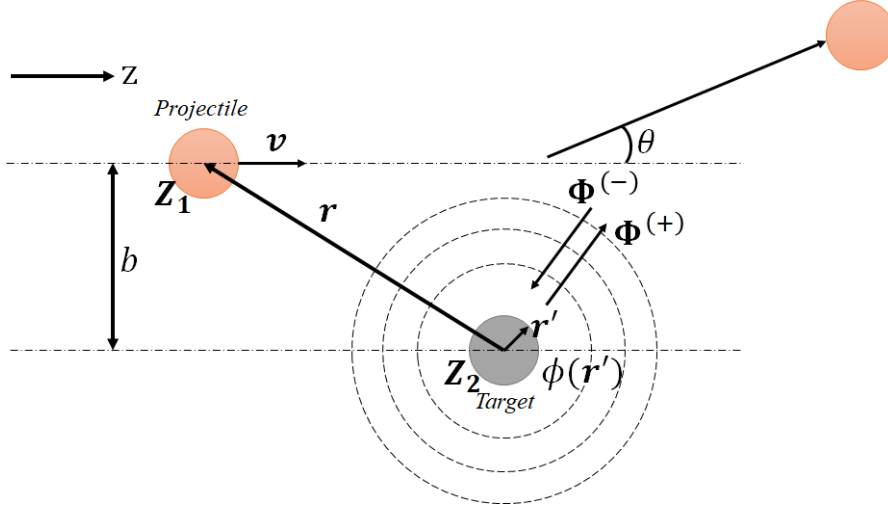


Figure 1.9: The projectile is scattered by coulomb interaction with the target nucleus.

$$f(\theta) = \frac{ik}{2\pi\hbar v} \int dr dr' \langle \Phi_{\mathbf{k}'}^{(-)}(\mathbf{r}) \phi_f(\mathbf{r}') | V_{int}(\mathbf{r}, \mathbf{r}') | \Phi_{\mathbf{k}}^{(+)}(\mathbf{r}) \phi_i(\mathbf{r}') \rangle, \quad (1.12)$$

where  $\theta$  is the polar scattering angle with respect to the beam direction,  $\mathbf{r}$  is the distance between the two nuclei,  $\mathbf{r}'$  is the internal coordinate of target nucleus,  $\Phi_{\mathbf{k}'}^{(-)}(\mathbf{r})$  and  $\Phi_{\mathbf{k}}^{(+)}(\mathbf{r})$  are the incoming and outgoing distorted waves, and  $\phi_{i(f)}(\mathbf{r}')$  is the initial (final) wave function of the target nucleus, respectively. At intermediate bombarding energies, we can apply eikonal wave functions for distorted waves. As a result the product of the outgoing scattered wave and the complex conjugate of the incoming scattered wave is given by

$$\Phi_{\mathbf{k}'}^{(-)*}(\mathbf{r}) \Phi_{\mathbf{k}}^{(+)}(\mathbf{r}) = \exp \left\{ -i \mathbf{q} \cdot \mathbf{r} - \frac{i}{\hbar v} \int U_N^{opt}(z', b) dz' + i \Psi_C(b) \right\} \quad (1.13)$$

where  $\mathbf{q} \equiv \mathbf{k}' - \mathbf{k}$ ,  $b$  is the impact parameter,  $U_N^{opt}$  is the nuclear optical potential and

$$\Psi_C(b) = 2 \frac{Z_1 Z_2 e^2}{\hbar v} \ln(kb), \quad (1.14)$$

that is the Coulomb phase. The detailed explanation about the nuclear optical potential is given in appendix. The interaction potential  $V_{int}$  is represented as

$$\begin{aligned} V_{int}(\mathbf{r}, \mathbf{r}') &= \frac{v^\mu}{c^2} j_\mu(\mathbf{r}') \frac{e^{i\kappa|\mathbf{r}-\mathbf{r}'|}}{|\mathbf{r}-\mathbf{r}'|} \\ &= \frac{v^\mu}{c^2} j_\mu(\mathbf{r}') \cdot 4\pi i \kappa \sum_{lm} j_l(\kappa r_{<}) Y_{lm}^*(\hat{\mathbf{r}}_{<}) h_l(\kappa r_{>}) Y_{lm}(\hat{\mathbf{r}}_{>}), \end{aligned} \quad (1.15)$$

where  $\kappa = \frac{\omega}{c}$  and  $j_\mu(\mathbf{r}')$  is the charge four-current for the intrinsic excitation of target nucleus by an energy of  $\hbar\omega$ .  $r_{>}(r_{<})$  refers to either  $r$  or  $r'$  that has the larger (smaller) magnitude.  $j_l$  is the Spherical  $l$ th Bessel function and  $h_l$  is the  $l$ th Hankel function. Inserting Eq.(1.13) and Eq.(1.15) in Eq.(1.12), one gets

$$\begin{aligned} f(\theta) &= i \frac{Z_1 e k}{\gamma \hbar v} \sum_{\pi l m} i^m \left( \frac{\omega}{c} \right)^l \sqrt{2l+1} e^{-im\phi} \Omega_m(q) G_{\pi l m} \left( \frac{c}{v} \right) \\ &\quad \times \langle I_f M_f | O(\pi l, -m) | I_i M_i \rangle, \end{aligned} \quad (1.16)$$

where  $\langle I_f M_f | O(\pi l, -m) | I_i M_i \rangle$  is the transition matrix, and  $G_{\pi l m}$  (the Winther-Alder relativistic function) and  $\Omega_m(q)$  are defined by,

$$G_{Elm} \left( \frac{c}{v} \right) = i^{\lambda+\mu} \frac{\sqrt{16\pi}}{\lambda(2\lambda+1)!!} \left( \frac{(\lambda-\mu)!}{(\lambda+\mu)!} \right)^{\frac{1}{2}} \left( \left( \frac{c}{v} \right)^2 - 1 \right)^{-\frac{1}{2}} \times \left\{ \frac{(\lambda+1)(\lambda+\mu)}{2\lambda+1} P_{\lambda-1}^{\mu} \left( \frac{c}{v} \right) - \frac{\lambda(\lambda-\mu+1)}{2\lambda+1} P_{\lambda+1}^{\mu} \left( \frac{c}{v} \right) \right\}, \quad (1.17)$$

$$G_{Mlm} \left( \frac{c}{v} \right) = i^{\lambda+\mu+1} \frac{\sqrt{16\pi}}{\lambda(2\lambda+1)!!} \left( \frac{(\lambda-\mu)!}{(\lambda+\mu)!} \right)^{\frac{1}{2}} \left( \left( \frac{c}{v} \right)^2 - 1 \right)^{-\frac{1}{2}} \mu P_{\lambda}^{\mu} \left( \frac{c}{v} \right), \quad (1.18)$$

$$\Omega_m(q) = \int_0^{\infty} db b J_m(qb) K_m \left( \frac{\omega b}{\gamma v} \right) \exp \{ i\chi(b) \}, \quad (1.19)$$

where  $q = 2k \sin \left( \frac{\theta}{2} \right)$  is the momentum transfer.  $K_m$  is the  $m$ th modified Bessel function and

$$\chi(b) = -\frac{1}{\hbar v} \int_0^{\infty} U_N^{opt}(z', b) dz' + \Psi_C(b) \quad (1.20)$$

is the eikonal phase. On the other hand in terms of the photo-absorption cross section the Coulomb excitation cross section is given by

$$\frac{d^2\sigma}{d\Omega dE_{\gamma}} = \frac{1}{E_{\gamma}} \sum_{\pi\lambda} \frac{dn_{\pi\lambda}}{d\Omega} \sigma_{\gamma}^{\pi\lambda}(E_{\gamma}), \quad (1.21)$$

where  $dn_{\pi\lambda}/d\Omega$  is the virtual photon number and  $\sigma_{\gamma}^{\pi\lambda}(E_{\gamma})$  is the photo-absorption cross section given by

$$\sigma_{\gamma}^{\pi\lambda}(E_{\gamma}) = \frac{(2\pi)^3 (\lambda+1)}{\lambda \{(2\lambda+1)!!\}^2} \left( \frac{E_{\gamma}}{\hbar c} \right)^{2\lambda-1} \frac{dB(\pi\lambda)}{dE_{\gamma}}. \quad (1.22)$$

Comparing Eq.1.21 with the coulomb excitation cross section obtained from the scattering amplitude ( $\frac{d^2\sigma}{d\Omega dE_{\gamma}} = |f(\theta)|^2$ ), one finds

$$\frac{dn_{\pi\lambda}}{d\Omega} = Z_1^2 \alpha \left( \frac{\omega k}{\gamma v} \right)^2 \frac{\lambda(2\lambda+1)!!^2}{(2\pi)^3 (\lambda+1)} \sum_m |G_{\pi l m}|^2 |\Omega_m(q)|^2, \quad (1.23)$$

where  $\alpha$  is the finestructure constant. Examples of the calculation are shown in Fig.1.10.

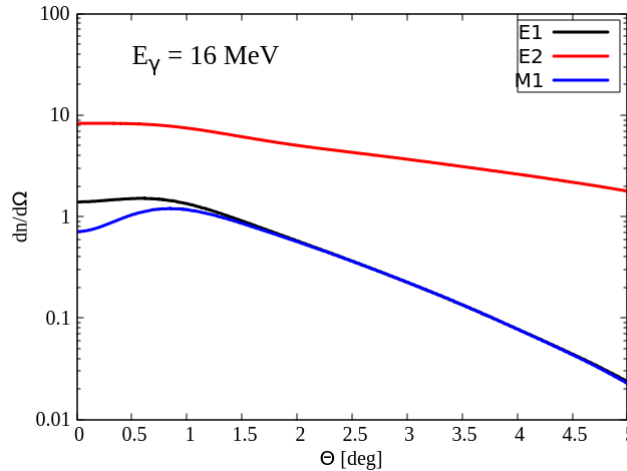


Figure 1.10: The virtual photon number per solid angle for  $E_{\gamma}=16$  MeV caused by 392 MeV protons scattered on  $^{90}\text{Zr}$ .

As can be seen, the virtual photon numbers become large at forward scattering angle, thus the Coulomb excitation cross section is enhanced at forward angle. In case of the GDR, namely the E1 transition, the reduced matrix element is given by

$$\frac{dB(E1)}{dE} = \frac{9\hbar c}{16\pi^3} \frac{d^2\sigma}{d\Omega dE} \times \frac{1}{\frac{dn_{E1}}{d\Omega}}. \quad (1.24)$$

## Chapter 2

# Experimental Setup

## 2.1 Overview of experimental setup

### 2.1.1 Beam line

We performed the experiment at the WS course in RCNP. The WS course is the specialized beam line for high energy resolution experiments by light ion scattering. Fig.2.1 shows an overview of the RCNP facility. First, a proton beam was accelerated by K140 Azimuthally Varying Field (AVF) cyclotron up to 65 MeV. Then it was injected to the K400 Ring cyclotron and was accelerated up to 392 MeV. The accelerated proton beam was transported to the WS course and bombarded the target in a scattering chamber with an intensity of 1-3 nA. The scattered protons were analyzed by the Grand Raiden magnetic spectrometer and were detected by drift chambers at the focal plane.

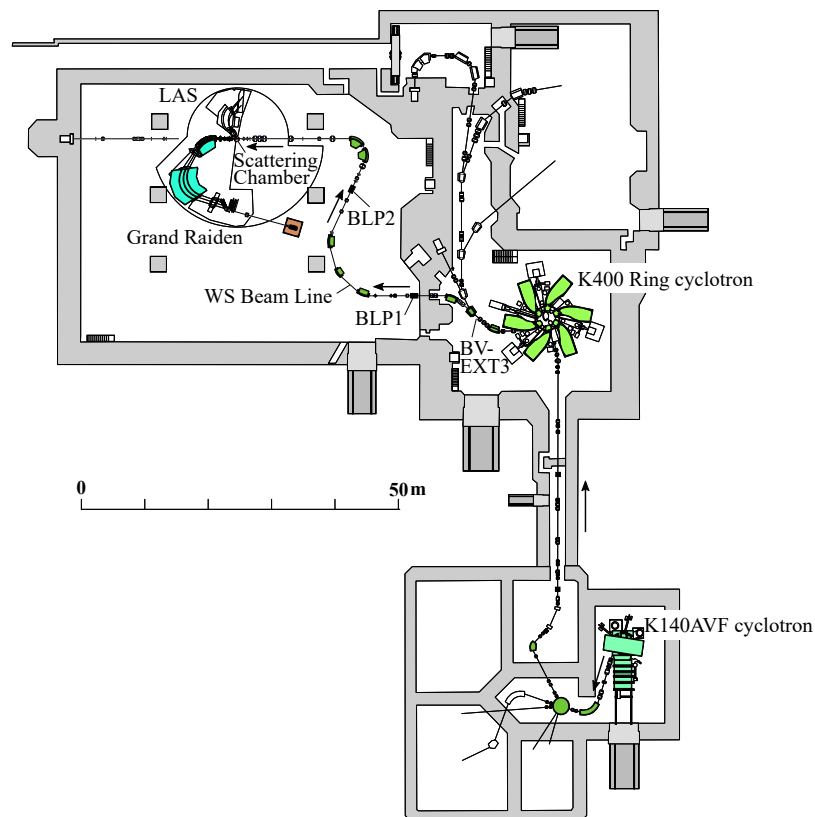


Figure 2.1: Overview of the RCNP cyclotron facility.

### 2.1.2 Beam line polarimeter

The beam line polarimeter (BLP) is a detector system placed at the WS beam line to monitor a beam profile, such as beam current and polarization (see Fig.2.1). The layout of a horizontally placed BLP (L-L' and R-R') is shown in Fig.2.2. The horizontally (vertically) placed BLP consists of two pairs of two plastic detectors in a horizontal (vertical) plane. The pairs in vertically placed BLP are named with U and D. A thin aramid target with a thickness of  $4 \mu\text{m}$  was periodically inserted into the beam for short times (1 s out of 10 s). Aramid has little thermal deformation. Therefore the target thickness is stable during the beam irradiation. Plastic scintillator detectors were set at scattering and recoiling angles of  $17.0^\circ$  and  $69.7^\circ$  to detect elastically scattering hydrogen with a coincidence between two detectors. Since in this experiment unpolarized proton beam was used, we just extracted the beam current from the detected number of events by the four pairs, L, R, U and D. The detailed analysis is described in 3.1.1.

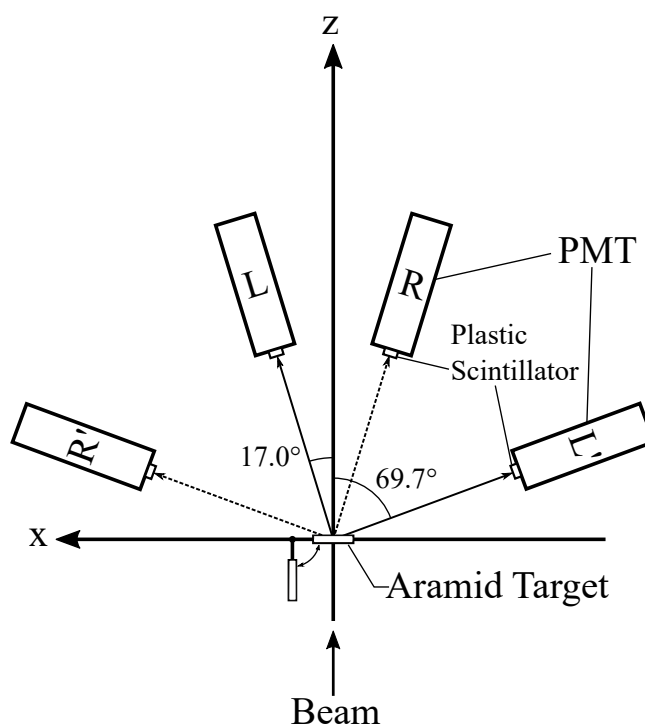


Figure 2.2: The top view of horizontally placed BLP.

## 2.2 Magnetic Spectrometer "Grand Raiden"

### 2.2.1 High resolution magnetic spectrometer Grand Raiden

The Grand Raiden spectrometer is a high energy resolution magnetic spectrometer (Fig.2.3) which consists of Q1-SX-Q2-D1-D2 magnets, where D is a dipole, Q is a quadrupole, SX is a sextupole magnet, respectively. This spectrometer allows us to analyze the momentum of scattered particles with a high momentum-resolution power of  $p/\Delta p \sim 37000$  and a momentum acceptance of  $\pm 2.5\%$ . Other detailed parameters are summarized in Tab.2.1[FUJ99]. In the zero degree measurement, a primary beam was transported to the beam dump which was located 12 m downstream of focal plane detectors and was shielded by iron and concrete to reduce the backgrounds for the focal plane detectors and the  $\gamma$  ray detectors. Inside the beam dump, the beam current was monitored by the 0deg Faraday cup. During the finite angle measurements the primary beam was stopped at Q1FC placed at just after the Q1 magnet (Fig.2.4).

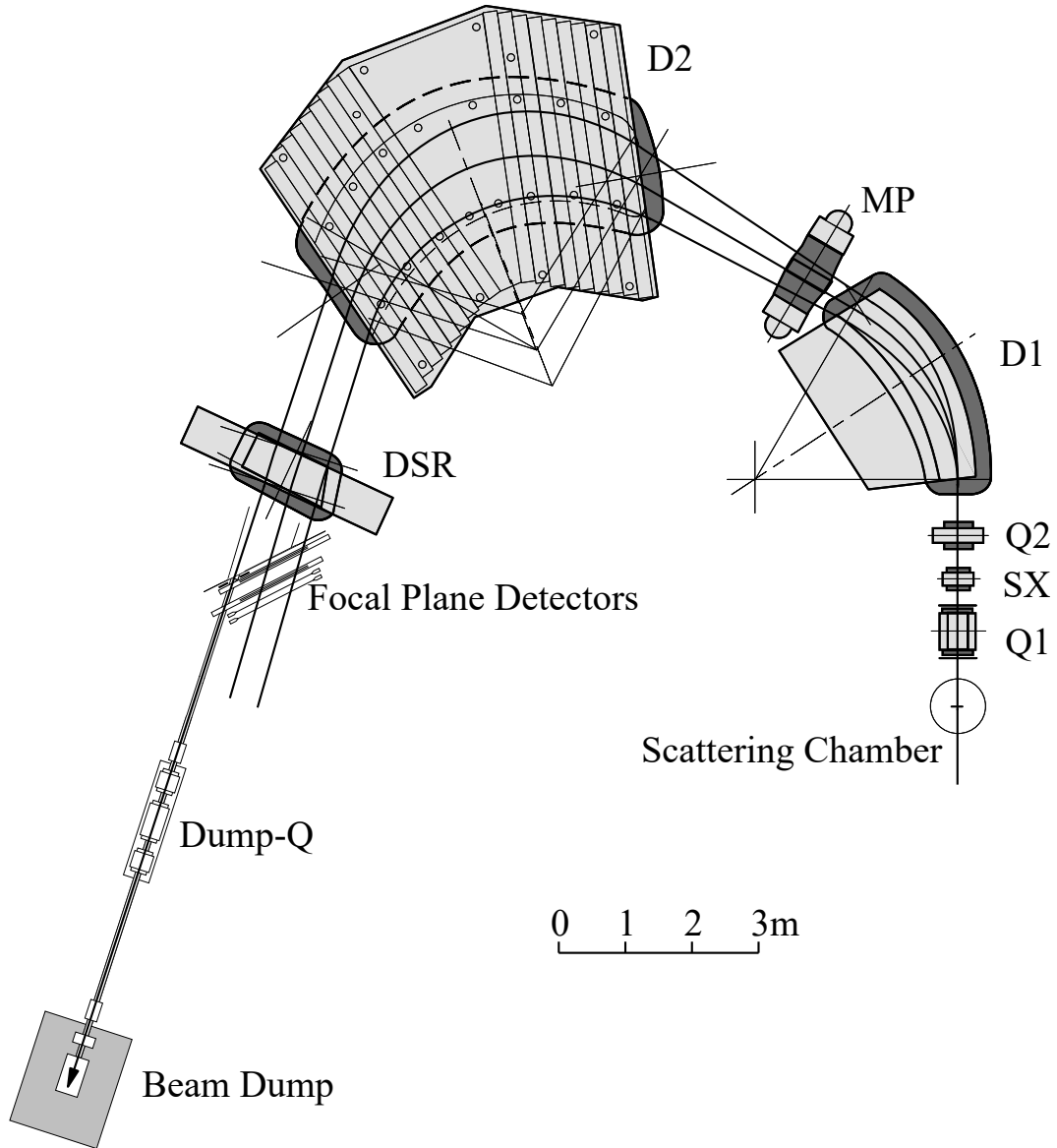


Figure 2.3: Overview of Grand Raiden and focal plane detector system in zero degree measurement.

Table 2.1: Design specification of the Grand Raiden spectrometer.

Configuration	Q1-SX-Q2-D1-D2
Mean orbit radius	3 m
Total deflecting angle	162°
Tilting angle of focal line	45.0°
Maximum magnetic rigidity	5.4 Tm
Vertical magnification	5.98
Horizontal magnification	-0.417
Momentum dispersion	15451 mm
Momentum range	5%
Momentum resolution	37076
Acceptance of horizontal angle	$\pm 20$ mrad
Acceptance of vertical angle	$\pm 70$ mrad

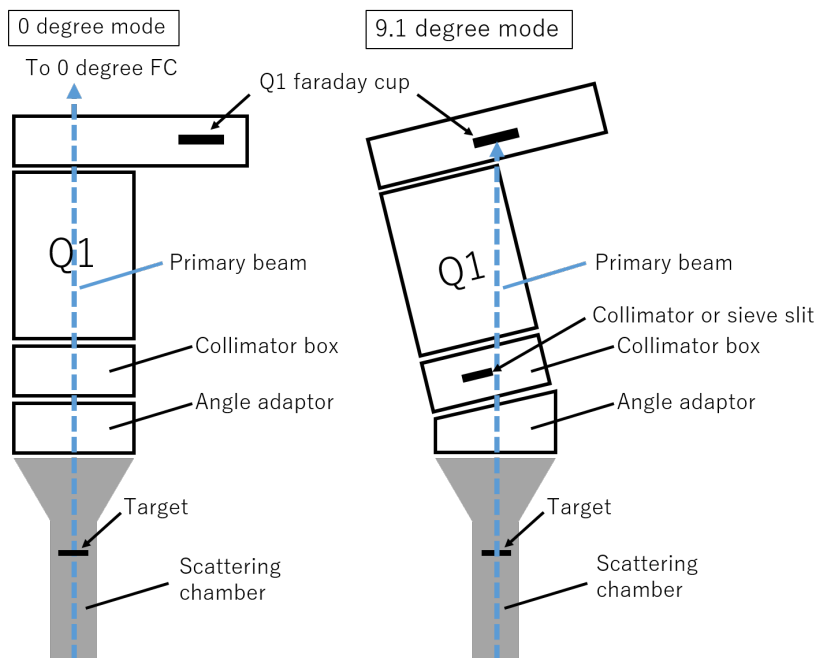


Figure 2.4: Setups around the scattering chamber in the zero degree mode and in the finite angle mode are drawn. The sieve-slit is explained in the Sec.2.2.3.

2.2.2 Focal plane detector system

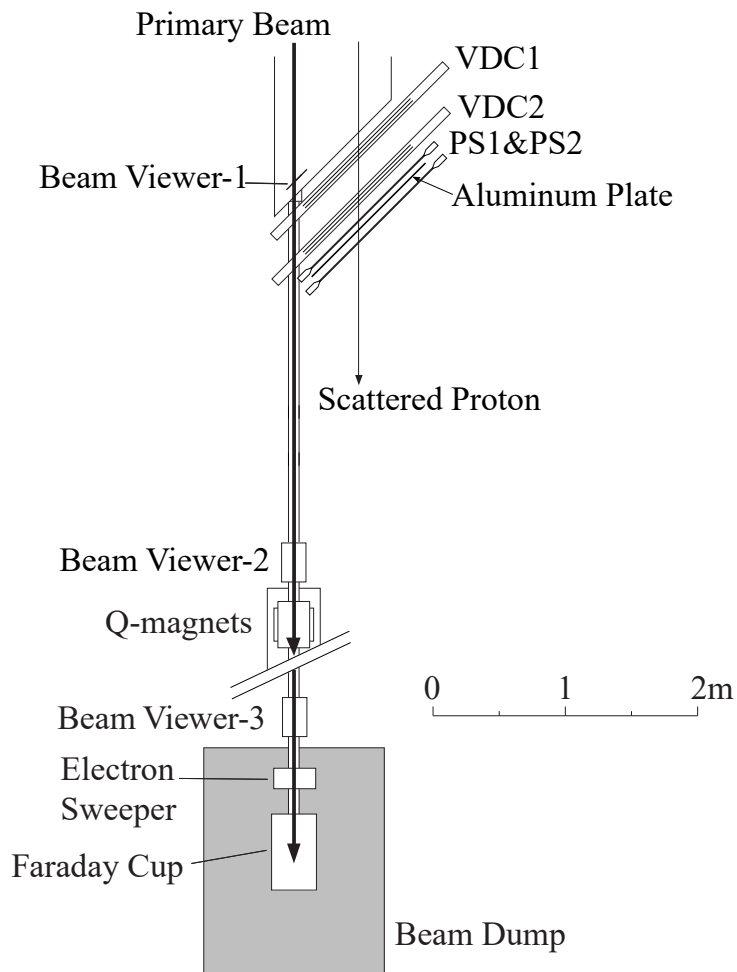


Figure 2.5: Layout of the GR detector system.

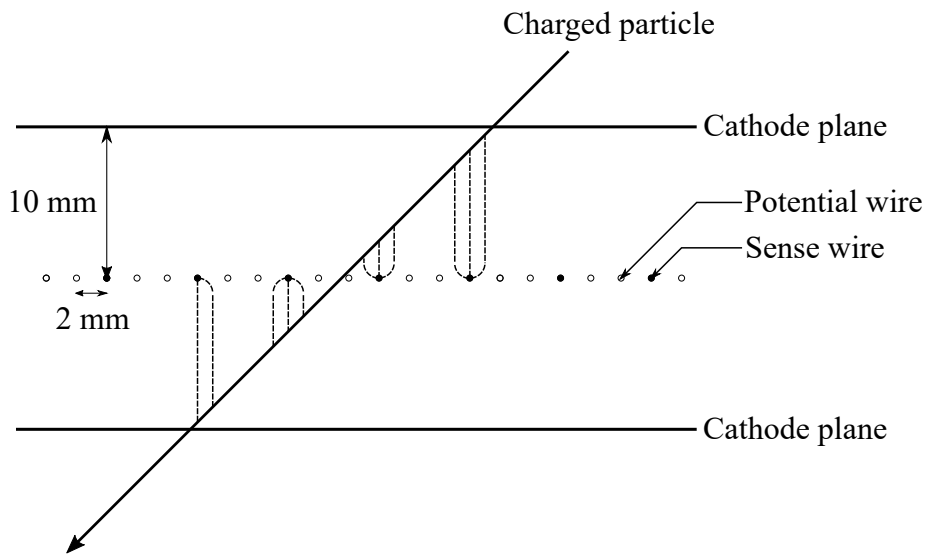


Figure 2.6: The structure of VDC. The dotted lines indicate paths of the liberated electrons by the charged particles.

Focal plane detector system consists of two multiwire drift chambers, of Vertical Drift type (VDC1,2) and two plastic scintillators (PS1,2) of 10 mm thickness (see Fig.2.5). Two plastic scintillators were used for the three purposes: energy loss detection for particle identification, generation of trigger signals for the data acquisition and a start signal for the timing of VDCs. The particle identification was performed by measuring the time of flight and the energy deposit in the plastic scintillators. VDCs were used to track the scattered particle and then to calculate the momentum and the scattering angle at the target position. Schematic view of the VDC is shown in Fig.2.6. Specifications of VDCs are summarized in Tab.2.2. Each VDC has two sets of wire planes (X and U), which are sandwiched between three cathode planes. While wires in each X plane are stretched perpendicularly to the dispersion direction of the GR spectrometer, wires in each U plane are tilted by an angle of  $48.19^\circ$ .

A high voltage of -5.75 kV was applied to each cathode plane after optimization for the maximum efficiency. -0.3 kV was applied as a potential voltage which played a role to increase the efficiency by changing the electric field of VDC and guiding the electrons to the direction of the anode wires. VDCs were filled by a mixture gas of argon (70%) and isobutane (30%) and a small amount of isopropyl alcohol. Argon is the main gas to be ionized and isobutane is the quencher gas to absorb photons from excited argon gas. Organic quencher gas like isobutane can result in the formation of polymers which accumulate on the anode and cathode of the detector after irradiation. This causes a continuous discharge of detector. In order to avoid this problem, isopropyl alcohol was added. Isopropyl alcohol is ionized by the charge exchange with isobutane ions and doesn't make polymers.

Electrons liberated by passing charged particles drift to the anode wires along the electric field which is vertical to the cathode plane and the anode plane (2.6). The drift time of electrons was measured and used to reconstruct the tracking of particles. The detailed analysis to convert the drift time to the position of particles will be discussed in 3.1.2. For example, we can know the horizontal position of particles from X plane. A combination of a X plane and an U plane provides a two dimensional position of particles. By connecting two points at VDC1 and VDC2, we can reconstruct a three dimensional tracking of particles.

Table 2.2: Properties of the vertical drift chamber.

Wire configuration	X( $0^\circ$ ), U( $48.19^\circ$ )
Active area, $\text{mm}^2$	$1150^W \times 120^H$
Number of sense wires	192(X), 208(U)
Anode cathode gap	10 mm
Anode wire spacing	2 mm
Sense wire spacing	6 mm(X), 4 mm(U)
Applied voltage	-5.75 kV(cath.), -0.3 kV(pot.)
Entrance and exit window	12.5 $\mu\text{m}$ carbon aramid film
Sense wires	20 $\mu\text{m}$ $\phi$ gold-plated tungsten wire
Potential wires	50 $\mu\text{m}$ $\phi$ gold-plated beryllium-copper wire
Cathode	10 $\mu\text{m}$ carbon-aramid film
Gas mixture	argon(70%)+isobutane(30%)+isopropyl alcohol

### 2.2.3 Sieve-slit measurements

During the finite angle measurement, sieve-slit measurements were performed to calibrate the scattering angle at the target position. The sieve-slit is a stainless plate which has 25 small holes (Fig.2.7). The sieve-slit was placed at the entrance of the Grand Raiden spectrometer instead of the collimator (Fig.2.4). If we know the distance between the target and the sieve-slit, we can calculate the scattering angles for each hole. The analysis for the calibration of the scattering angle is discussed in Sec.3.1.4.

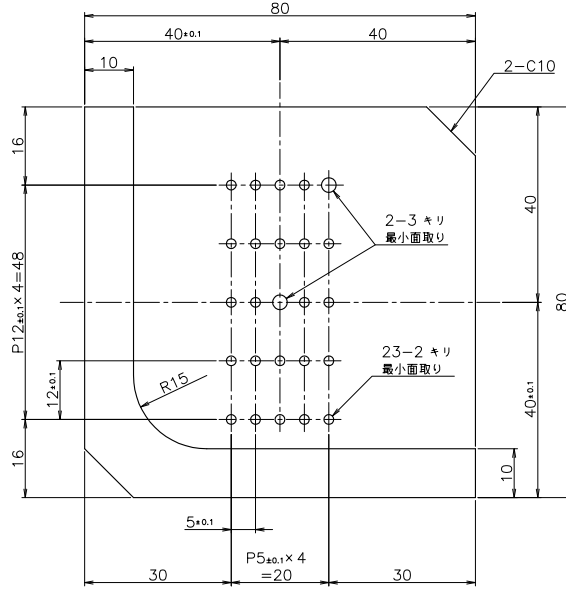


Figure 2.7: Design of a sieve-slit. The diameter of each hole is 2 mm ,while that of the center hole is 3 mm. The thickness is 5 mm.

## 2.2.4 Under-focus mode

In order to reduce additional backgrounds, no collimator to define the solid angle was used at the entrance of Grand Raiden in the measurement of zero degree mode. Therefore it was necessary to determine the scattering angle at the target position by reconstructing from the tracking information at focal plane detectors with a small uncertainty. However, the resolution of vertical scattering angle is worse than  $1^\circ$  in the normal focus mode. We can achieve better angle resolution by adjusting the Q1 magnet. Vertical ion optics of Grand Raiden for different vertical focus mode are drawn in Fig.2.8. This time we applied a mild under focus mode, under which the vertical focus point is moved to downstream, by reducing the Q1 magnet by 6% relative to the normal focus mode. Under this condition the vertical scattering angle  $\phi$  at the target position is reflected on the vertical position  $y$  at the focal plane coordinate. In terms of the transfer matrix, normal focus mode corresponds to making the matrix element  $(y|\phi)$  zero. Here the matrix elements are defined by

$$\begin{pmatrix} y_d \\ \phi_d \end{pmatrix} = \begin{pmatrix} (y|y) & (y|\phi) \\ (\phi|y) & (\phi|\phi) \end{pmatrix} \begin{pmatrix} y_t \\ \phi_t \end{pmatrix}, \quad (2.1)$$

where  $d$  denotes the coordinate at the focal plane detector and  $t$  denotes at the target position. These coordinate systems are defined visually in Fig.3.3 and Fig.3.4. Determination of a transfer matrix should be one due to the Liouville's theorem. Since the vertical magnification  $(y|y)$  is 5.98 in the normal focus mode, the magnification for vertical scattering angle  $(\phi|\phi)$  becomes  $\frac{1}{(y|y)} \sim 0.17$  at the vertical focusing point and this fact results in worse resolution in vertical scattering angle. Changing the Q1 magnetic field means that changing the  $(y|\phi)$  to finite value because the vertical scattering angle  $\phi_t$  affects the  $y_d$  as seen in Fig.2.8.

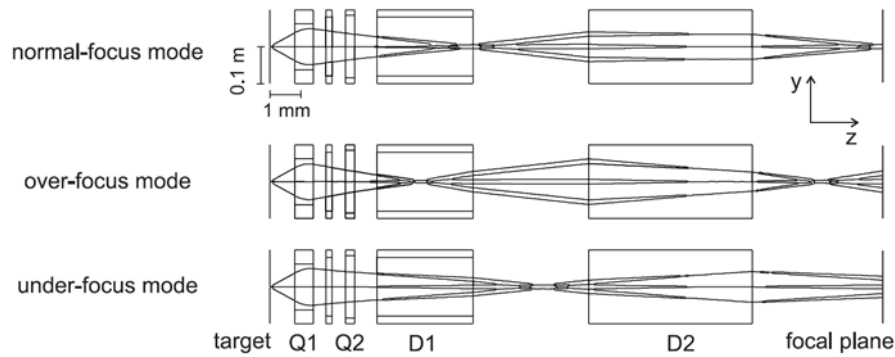


Figure 2.8: By changing the magnetic field of Q1, the vertical focus point is moved in the z direction.

## 2.3 $\gamma$ ray detector

### 2.3.1 Large volume $\text{LaBr}_3\text{:Ce}$ detector



Figure 2.9: Large volume  $\text{LaBr}_3$  detector and the crystal [GIA13].

We used eight large volume  $\text{LaBr}_3\text{:Ce}$  detectors which were developed by Milano group (Fig.2.9) [GIA13]. The  $\text{LaBr}_3\text{:Ce}$  is a cerium-doped inorganic scintillator made of lantham and bromine, where cerium is used to increases the light emission efficiency. The first small size of  $\text{LaBr}_3$  crystal became available in 2001 then the crystal manufacturer Sain-Gobain succeeded in growing up large volume crystals in 2008. Milano group studied the properties of this large volume  $\text{LaBr}_3$  crystal with a few types of voltage dividers and developed the best combination of the crystal and the divider and the PMT then summarized the results in [GIA13]. Nowadays this large volume  $\text{LaBr}_3$  detector is known as "HECTOR". The crystal has a cylindrical shape with  $\phi 89 \text{ mm} \times L 203 \text{ mm}$ . Because of the remarkable properties deccribed below, this large volume  $\text{LaBr}_3$  detector was chosen as gamma ray detector for this experiment.

- **Good energy resolution**

$\text{LaBr}_3$  has the best energy resolution among the all scintillators, typically 3% for 662 keV gamma ray and it is the only scintillator able to separate the full energy peak from the first escape peak, up to at least 25 MeV gamma ray. Though we are interested in the ground state gamma decay from the GDR in this experiment, there should be other cascade decay channels. If the energy resolution was not good enough, it would be impossible to separate the ground state decay peak from other decay channels, then the uncertainty in the results will be larger.

- **Good timing resolution** LaBr<sub>3</sub> is famous for its fast timing resolution (Tab.2.3). In general the larger a crystal become, the worse a timing resolution is because of the reflection of photons in a crystal. In spite of its large volume, this HECTOR still keeps the timing resolution less than 1 nsec. Such a fast response makes the detector possible to stand high count rate measurements. Of course, this property is also determined by the attached PMT, but it is guaranteed by Milano group that the HECTOR works well up to a count rate of 200 k Hz [GIA13].
- **High efficiency**  
LaBr<sub>3</sub> has relatively high material density:5.1 g/cm<sup>3</sup> and atomic number, which makes the gamma ray efficiency higher. In addition to that, the large volume of crystal increases the efficiency. Due to not only the small branching ratio of ground state gamma decay from the GDR but also the energy of gamma ray:>10 MeV, detection is quite difficult. Therefore the high efficiency is a really important property for this experiment.

Though the basic performance of the LaBr<sub>3</sub> detector is well summarized in [GIA13], we checked the performance of LaBr<sub>3</sub> detectors with gamma ray sources before the beam time. Results are summarized in Tab.2.3 with the value of typical NaI detector for comparison.

Table 2.3: Basic performance of LaBr<sub>3</sub> and NaI.

Detector	Energy resolution @662keV	Decay time	Absolute efficiency@662keV (source at 200 mm)
LaBr <sub>3</sub>	3.2%	0.07 $\mu$ sec	0.018
NaI[KNO10]	10%	0.23 $\mu$ sec	-

Moreover this LaBr<sub>3</sub> detector is assured a good linearity up to 25 MeV gamma ray and a durability for the neutron radiation. These extreme properties never be satisfied by other kind of detectors. For example, the germanium detector doesn't have enough efficiency (the material density is almost same as LaBr<sub>3</sub> but it's difficult to obtain large volume one) and the time response is worse than LaBr<sub>3</sub>. Additionally the germanium detector is damaged by the neutron radiation. The NaI detector doesn't have enough timing resolution and its efficiency is worse than LaBr<sub>3</sub> due to the smaller material density:3.67 g/cm<sup>3</sup> and smaller atomic number.

Another interesting characteristics of LaBr<sub>3</sub> is the internal radioactivity. Even without any radioactive sources, several peaks are seen in energy spectrum (Fig.2.10). The activity below 1.5 MeV is coming from the decay of <sup>138</sup>La and the structure above 1.5 MeV is from the alpha decay chain of <sup>227</sup>Ac. The peak around 1.4 MeV is the sum of a 1436 keV gamma ray from the excited state of <sup>138</sup>Ba and a 32 keV X-ray in <sup>138</sup>Ba after an electron capture process. Strictly speaking, 1.46 MeV gamma rays that are from an excited state of <sup>40</sup>Ar after an EC are also contained in the 1.4 MeV peak. The trapezoid-shaped continuum around 700 keV corresponds to the sum of a 789 keV gamma ray from the excited state of <sup>138</sup>Ce after beta decay of <sup>138</sup>La and a following beta-ray with a 255 keV endpoint energy.

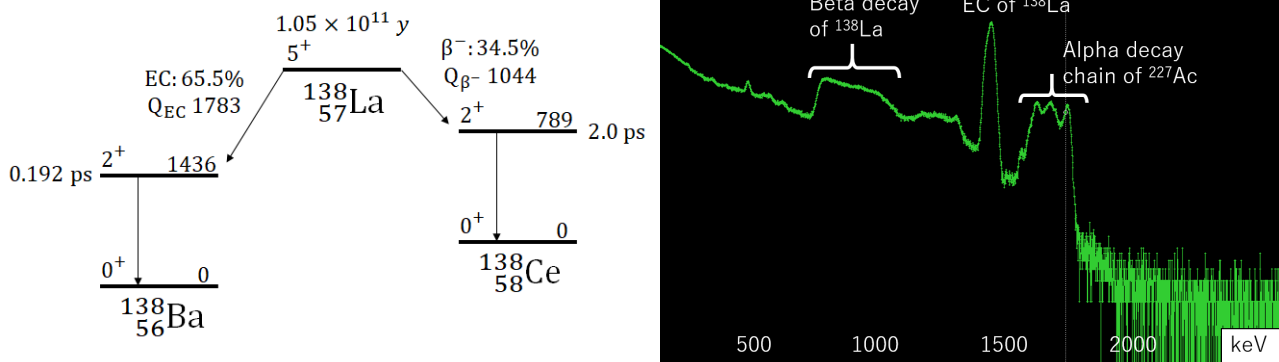


Figure 2.10: Decay scheme of  $^{138}\text{La}$  and an energy spectrum of  $\text{LaBr}_3$  itself without any radioactive sources. The horizontal axis of the energy spectrum is scaled for gamma ray energy, while the structure above 1.5 MeV is associated with alpha decay chain of  $^{227}\text{Ac}$ , not a gamma decay. Thus the real alpha decay energy should be larger than this scaled energy.

### 2.3.2 Detector array "Scylla"

A supporting frame for  $\text{LaBr}_3$  detectors named "Scylla" (Supporting construction for  $\gamma$ -ray-detecting large  $\text{LaBr}_3$  array) was constructed (Fig.2.11).

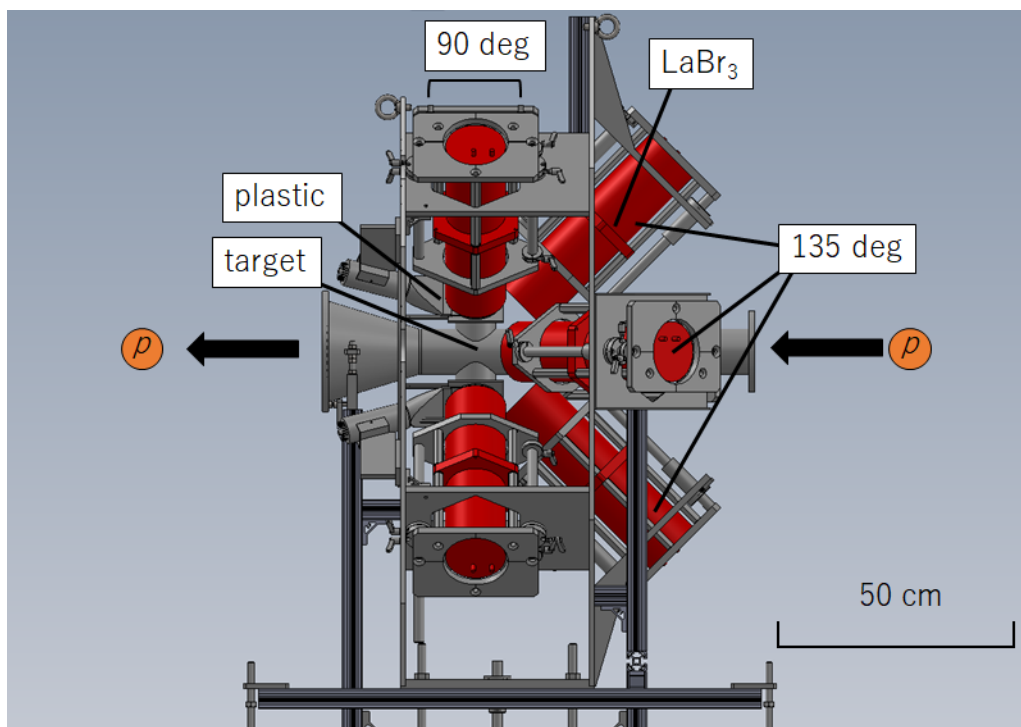


Figure 2.11: Sideview of Scylla with  $\text{LaBr}_3$  detectors.

Four detectors were placed at  $90^\circ$  with respect to the beam direction and another four detectors were placed at  $135^\circ$  (Fig.2.12). Each detector was assigned to the slot number, 1-4 for detectors at  $90^\circ$  and 5-8 for detectors at  $135^\circ$ . The distance from the target to the detector was adjustable and the minimum distance from the target to the surface of the detector was 137 mm for  $90^\circ$  and 135 mm for  $135^\circ$ . The covered solid angle was 20% of  $4\pi$  when detectors were set at the minimum distance. In addition to the  $\text{LaBr}_3$  detectors, four veto plastic scintillators were also placed in front of the  $90^\circ$  detectors to reject charged particle backgrounds. The thickness of the plastic scintillator was 2 mm and

the size was almost same as the diameter of the  $\text{LaBr}_3$ . The material name was EJ212. Furthermore, a lead absorber with a thickness of 2 mm and a copper absorber with a thickness of 4 mm were inserted in front of the plastic detector for  $90^\circ$  and in front of the  $\text{LaBr}_3$  detector for  $135^\circ$  to reduce low energy photons. The copper absorbers were used to absorb the X-rays from the lead absorber.

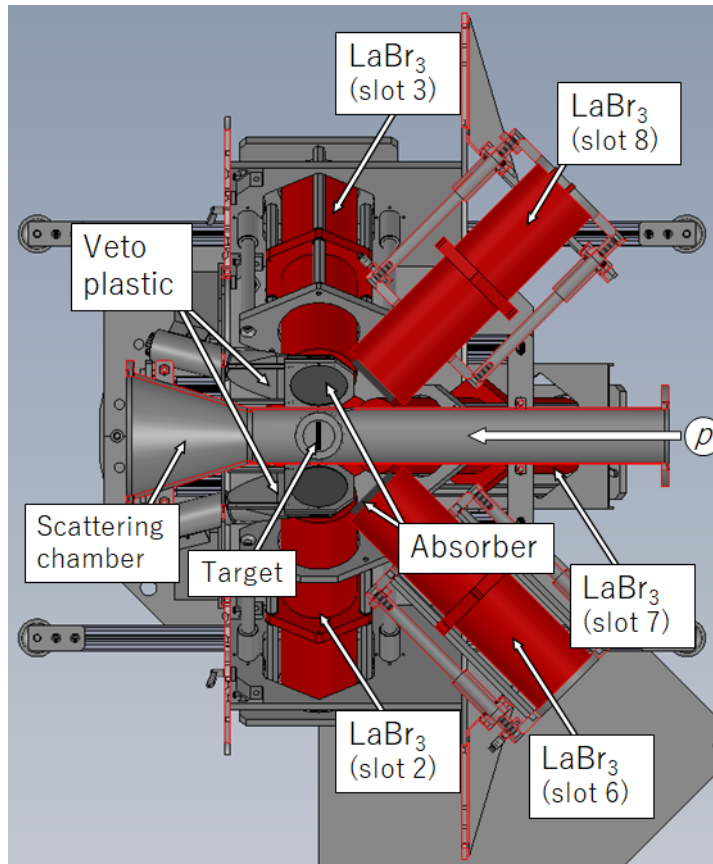


Figure 2.12: Top view of Scylla.

## 2.4 Trigger and data acquisition system

The data taking system consists of mainly two parts, Grand Raiden DAQ and  $\text{LaBr}_3$  DAQ.

Two plastic scintillators (GR plastic 1 and 2) which were placed at backwards of VDCs were used to produce a trigger for DAQ related with Grand Raiden spectrometer. Two PMTs (L and R) were attached on the both side of each scintillator and the output signal from each PMT was divided into two signals. One of two was used for ADC and the other one was for TDC and trigger. The trigger for Grand Raiden named "GR trigger" was generated with a coincidence between four PMTs (GR plastic 1L, 1R, 2L and 2R) (Fig.2.13).

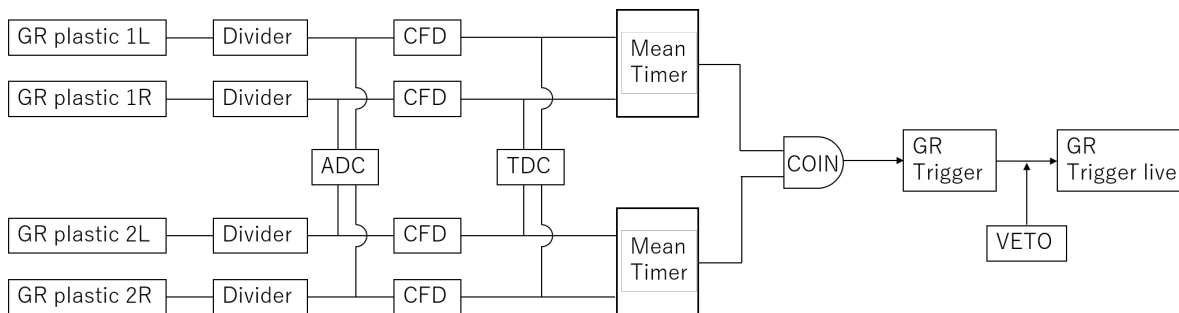


Figure 2.13: DAQ diagram for Grand Raiden.

DAQ diagram for LaBr<sub>3</sub> detector is a bit complicated. The charge information was taken by three different circuits. They are QDC, ADC and a combination of QTC and TDC. The QDC module which is a default setup in the WS course recorded integrated charge of the attenuated pulse from PMTs of each LaBr<sub>3</sub> detector. The ADC module recorded the height of the pulse which was shaped and amplified by LaBr<sub>3</sub>-PRO module that is dedicated for a LaBr<sub>3</sub> detector and was developed by the Milano group. LaBr<sub>3</sub>-PRO outputted a logic signal for timing information and a shaped analog signal for charge information. The QTC module converts the analogue pulse to the logic signal whose width is proportional to the charge of the pulse. Then the width between the leading edge and the trailing edge of the logic signal was recorded by TDC. From the leading edge information, we can know the timing information also. The QTC requires only a TDC module that works faster than ADC and QDC, so the dead time of DAQ will be shorter than the case of ADC and QDC. However this QTC method is still under development because the proportionality between the charge and the width of output logic signal is not confirmed well. Actually, in this time ADC data, namely data taken through LaBr<sub>3</sub>-PRO were used for the analysis because its energy resolution was the best in the three methods.

The logic output signals from 8ch LaBr<sub>3</sub>-PRO were sent to the logic module and an OR signal was generated if at least one of the detectors had a signal. This trigger was named as "LaBr<sub>3</sub> trigger".

Note that a circuit to produce a busy signal is omitted in these diagrams. A busy signal was produced in GR DAQ system and LaBr<sub>3</sub> DAQ system respectively. As a result "GR (LaBr<sub>3</sub>) trigger live" which was survived after a busy circuit was generated and was sent to a coincidence module together(Fig.2.15).

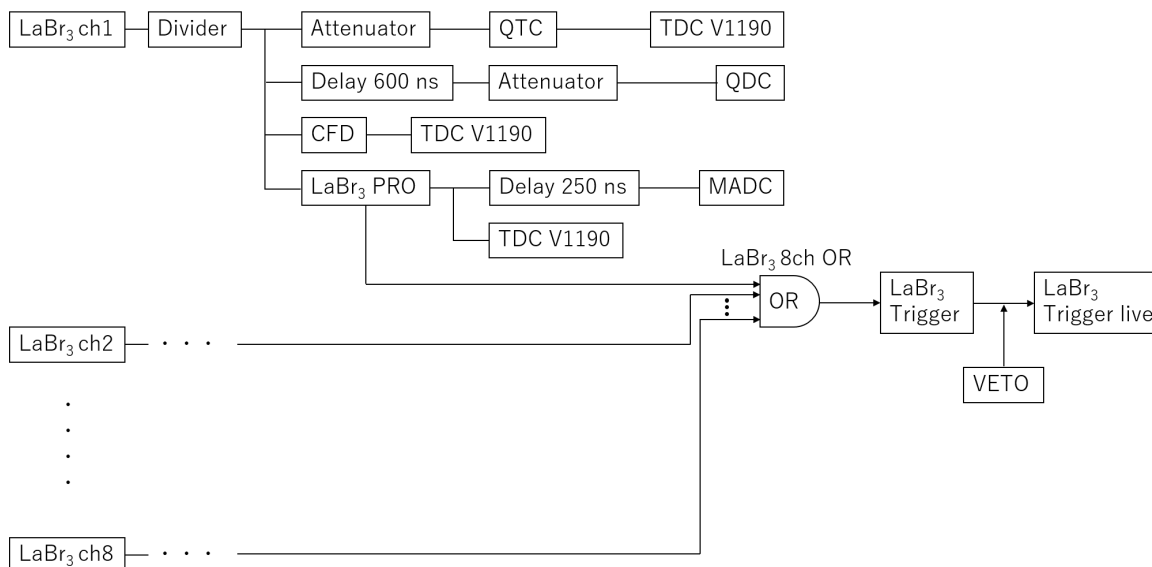


Figure 2.14: DAQ diagram for LaBr<sub>3</sub>.

"GR trigger live" and "LaBr<sub>3</sub> trigger live" were input to a logic module together. If only "GR (LaBr<sub>3</sub>) trigger live" was input, "GR (LaBr<sub>3</sub>) single" signal was generated. The "GR (LaBr<sub>3</sub>) single" signal was pre-scaled by 1/n (m) not to occupy the DAQ system and to have an efficient data acquisition of a coincidence trigger. If "GR trigger live" and "LaBr<sub>3</sub> trigger live" were input simultaneously, a "GR-LaBr<sub>3</sub> coin" trigger was generated. This signal was not pre-scaled. In total three types of triggers were produced, they are "GR single sampling" and "LaBr<sub>3</sub> single sampling" and "GR-LaBr<sub>3</sub> coin". These three triggers are mutually exclusive.

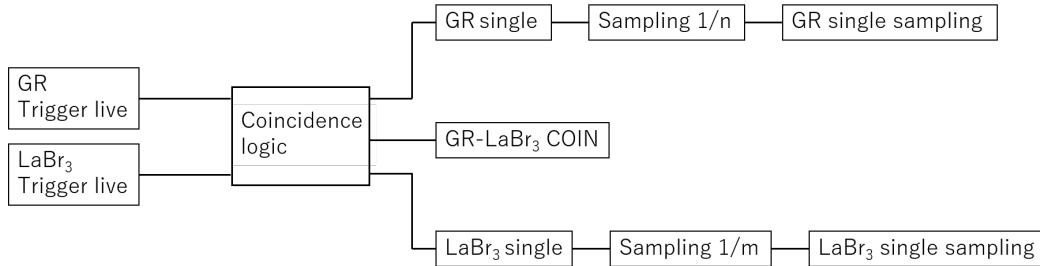


Figure 2.15: DAQ diagram for coincidence logic.

## 2.5 Targets

A metallic self-supporting foil of <sup>90</sup>Zr with a thickness of 20.0 mg/cm<sup>2</sup> was used as the main target. Actually, in the proposal we planned to use a 4 mg/cm<sup>2</sup> thickness target to minimize the energy straggling in the target, but at the beginning of the experiment we decided to use the main target to the 20 mg/cm<sup>2</sup> thickness target in order to earn more statistics. The thicker target makes the energy resolution worse due to the energy straggling in the target. In case of the 392 MeV proton beam, the energy straggling width is 46 keV for sigma in a <sup>90</sup>Zr target with a thickness of 20 mg/cm<sup>2</sup>. In the present experiment the beam energy spread was 100 keV, so the energy resolution would be 110 keV for in sigma, but it was acceptable because we planned to analyze the data with a 200 keV strip of excitation energy. In case of <sup>12</sup>C, the the energy resolution resulted in 115 keV in sigma ideally. <sup>12</sup>C and <sup>28</sup>Si were used as reference targets to calibrate the gamma ray energy and the efficiency of the LaBr<sub>3</sub> detectors. On the top of the target ladder, the viewer was set to monitor the beam position. The target ladder was tilted by 22.5° in order not to stand in the path of gammas ray to the LaBr<sub>3</sub> detectors at 90°.

The target ladder and the target chamber were made of aluminum in order to reduce backgrounds for gamma ray detectors due to activation. The height of the target ladder was remotely controlled during the experiment.

Table 2.4: List of targets.

Target	Thickness (mg/cm <sup>2</sup> )	Enrichment (%)
<sup>90</sup> Zr	20	97.65
<sup>90</sup> Zr	4	97.65
<sup>12</sup> C	29	nat.
<sup>28</sup> Si	11	nat.
<sup>196</sup> Au	1.68	nat.



Figure 2.16: Target ladder with targets and a viewer.

## 2.6 Summary of experimental conditions

First of all, beam tuning and starting up of the detectors were done in the finite angle mode ( $9.1^\circ$ ) of Grand Raiden. The elastic scattering from  $^{197}\text{Au}$  was measured in order to check the energy resolution, while the elastic scattering from  $^{90}\text{Zr}$  was taken for the target thickness calibration. These calibration runs were performed during the finite angle measurements.

After completing these preparation processes, Grand Raiden was rotated to zero degrees and we started the main measurements. Total measurement time for the main target:  $^{90}\text{Zr}$  was 70 hours. The length of each run was typically 1 hour. Calibration data with  $^{12}\text{C}$  was measured for 30 minutes every 6 hours. At both the beginning and the end of the beam time, data with  $^{28}\text{Si}$  were also taken for calibration of the energy and the efficiency of the  $\text{LaBr}_3$  detectors.

Overall experimental conditions are summarized in Tab 2.5.

Table 2.5: Summary of experimental conditions.

Target	Purpose	GR angle	Collimator	Beam intensity
$^{90}\text{Zr}$	main	$0^\circ$	no	1-3 nA
$^{90}\text{Zr}$	elastic	$9.1^\circ$	LR 20 mrad, UD 30 mrad	0.1 nA
$^{12}\text{C}$	calibration	$0^\circ$	no	1-3 nA
$^{28}\text{Si}$	calibration	$0^\circ$	no	1-3 nA
$^{196}\text{Au}$	elastic	$9.1^\circ$	LR 20 mrad, UD 30 mrad	0.1 nA

## Chapter 3

# Analysis

### 3.1 Analysis of Magnetic Spectrometer "Grand Raiden"

#### 3.1.1 Beam current calibration

The total beam current was obtained from the number of events detected by the BLP. The relationship between the beam current and the number of events in BLP was studied at the finite angle measurement and at that time the beam was stopped at Q1FC placed just after the Q1 magnet. The BLP and the Q1FC were away but we can assume that a transmission between them was almost 100% because if it was not 100%, it would be impossible to perform a zero degree measurement due to too much backgrounds. The BLP consists of four pairs (L,R,U,D) of plastic detectors (Fig.2.2) and counted the number of coincided events in each pair. Then the sum of the number of events  $N_{BLP} = N_L + N_R + N_U + N_D$  is expected to be proportional to the number of the beam particle  $N_{total}$ . The quantity of current per event counted by BLP  $q$  is given by

$$n = \frac{N_{total}}{N_{BLP}}. \quad (3.1)$$

During a calibration run,  $N_{total}$  was  $1.596 \times 10^{12}$  and  $N_{BLP}$  was 1000. Then  $n = 1.596 \times 10^9$ . The total beam current can be calculated from only the BLP data without putting Q1FC.

$$N_{beam} = n \times N_{BLP} \times \frac{T_{BLPout}}{T_{BLPin}}, \quad (3.2)$$

where the  $T_{BLPin(out)}$  is the total time when the BLP1 was (not) inserted into the beam. I analyzed data which the BLP was not inserted because the BLP may affect the beam profile and change the background structure at focal plane detector. This leads to the wrong estimation of background when analyzing the Grand Raiden data.

#### 3.1.2 Track reconstruction

The first step of the data analysis of Grand Raiden spectrometer is to reconstruct the track of protons. As explained in the experimental setup section, the drift time of electrons liberated by charged particles was recorded. A typical drift time distribution is shown in the upper left panel of Fig.3.1. The reason why the drift time distribution is not flat is that the electric field is stronger around the anode wires and thus the drift time of electrons which were liberated around the anode wires is much shorter than electrons liberated away from the anode wires. The drift time is almost proportional to the drift length because the VDC is designed to make the electric field constant except for the small region around the wires. The right panel of Fig.3.1 shows the relationship between the drift time and the drift length. After the drift time to the length conversion, a drift length which was distributed uniformly was obtained (see the left lower panel of Fig.3.1). Once the drift length was obtained in each plane, we could determine the intersection points of the path and the anode plane

by a least squares fit to the drift lengths of hit wires. Then the three dimensional complete tracking of the particles was calculated from the intersection points.

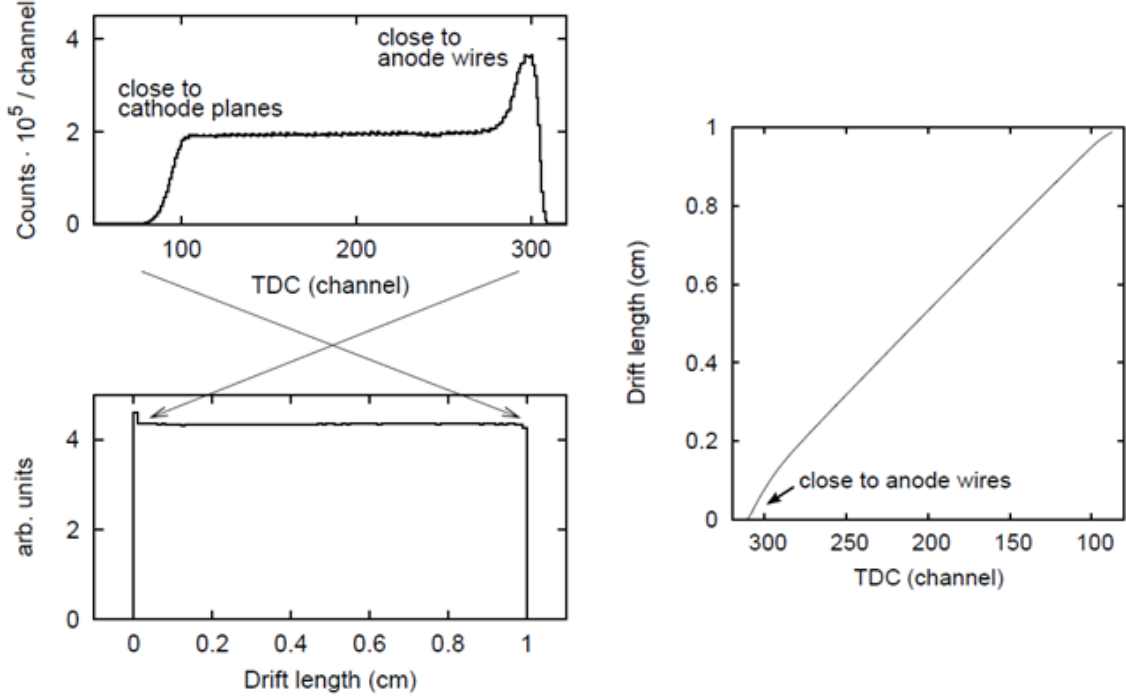


Figure 3.1: Drift time to length conversion.

### 3.1.3 Efficiency of the VDCs

The detection efficiency of the VDCs was calculated for each plane as the ratio between the number of events which were succeeded in detection by all the four wire planes and the number of events which were succeeded in detection by the other three planes. Here, "success" means that at least three wires had a signal in each plane. For instance, the detection efficiency of the X1 plane was calculated by

$$\epsilon_{X1} = \frac{N_{X1,U1,X2,U2}}{N_{X1,U1,X2,U2} + N_{U1,X2,U2}}, \quad (3.3)$$

where  $N_{X1,U1,X2,U2}$  is the number of events in which the position by the four planes were successfully determined and  $N_{U1,X2,U2}$  is the number of events which were failed to determine the position by the X1 but were successfully determined the position by the U1, X2 and U2. Furthermore, in this analysis, only events which were applied a gate of particle identification with the plastic detectors at the focal plane were used in order to exclude the background events. The tracking efficiency was calculated by multiplying the detection efficiency of each plane because all of them were necessary to reconstruct a track.

$$\epsilon_{total} = \epsilon_{X1} \times \epsilon_{U1} \times \epsilon_{X2} \times \epsilon_{U2} \quad (3.4)$$

A typical detection efficiency for each plane was 97-98% and a tracking efficiency was 89% on average during the experiment.

A dependence of the tracking efficiency on the position (momentum of scattered particles) was studied. The VDCs were not available to select a specific region of excitation energy when checking its efficiency because four of planes were necessary for reconstruction (if we used VDCs, the efficiency would be 100%). Plastic detectors at the focal plane was used to cut a position of the particles. The result is shown in Fig.3.2. The tracking efficiency is flat but is slightly decreasing above 25 MeV.

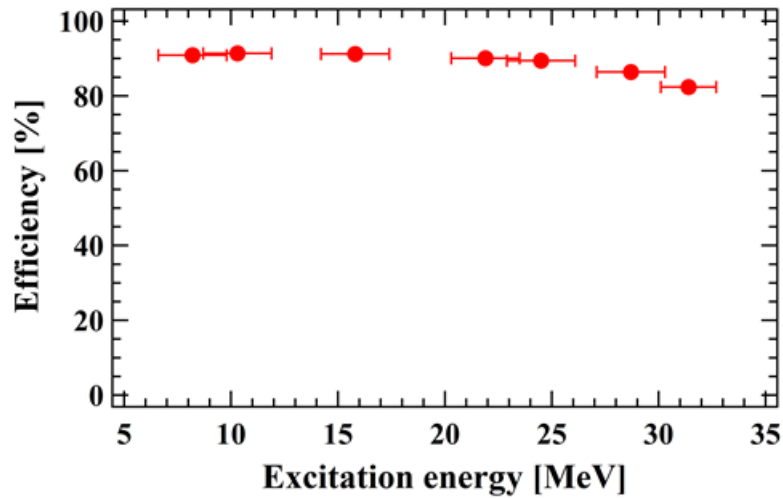


Figure 3.2: Tracking efficiency as a function of the excitation energy. Horizontal uncertainty is large due to the less accuracy of the position determined by the plastic scintillator.

### 3.1.4 Calibration of the scattering angle and determination of the solid angle

The coordinate systems at the target position and at the focal plane were defined as shown in Fig.3.3 and Fig.3.4. Currently, the scattering at the target position was partially calibrated. Just the horizontal scattering angle  $\theta$  was calibrated using the data of the sieve slit measurements. The scattering angle was determined with a multidimensional least squares fit

$$\theta_t = \sum_{i,j}^2 (\theta | x^i \theta^j ) x_d^i \theta_d^j. \quad (3.5)$$

The calibrated horizontal scattering angle is shown in Fig.3.5.

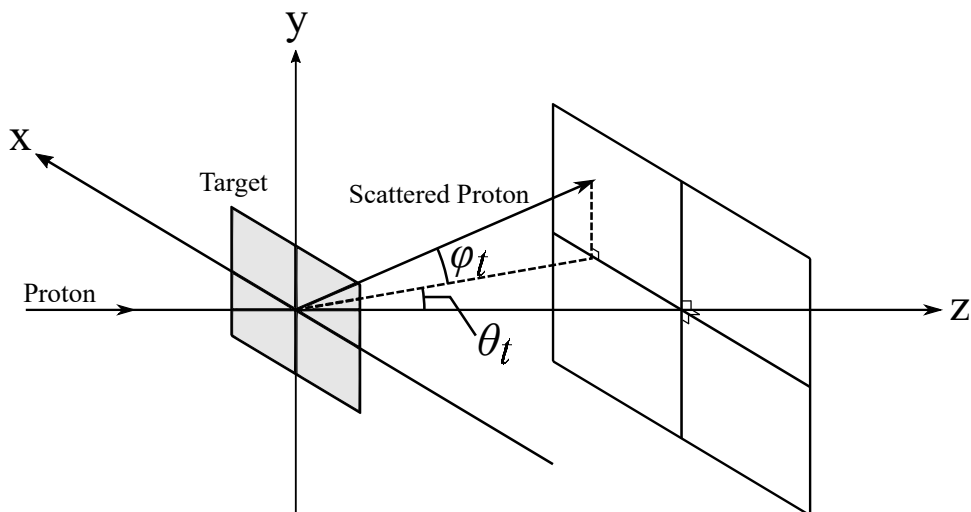


Figure 3.3: Coordinate system at the target position.

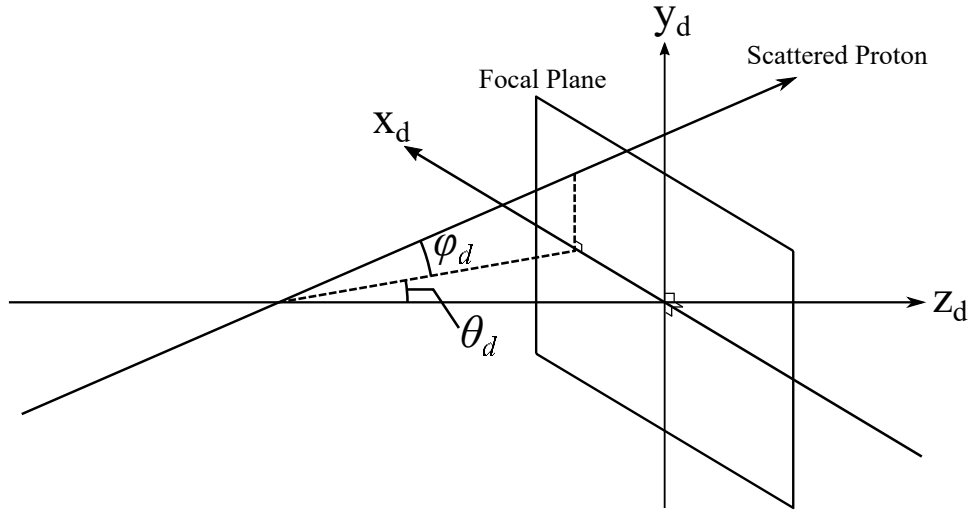


Figure 3.4: Coordinate system at the focal plane.

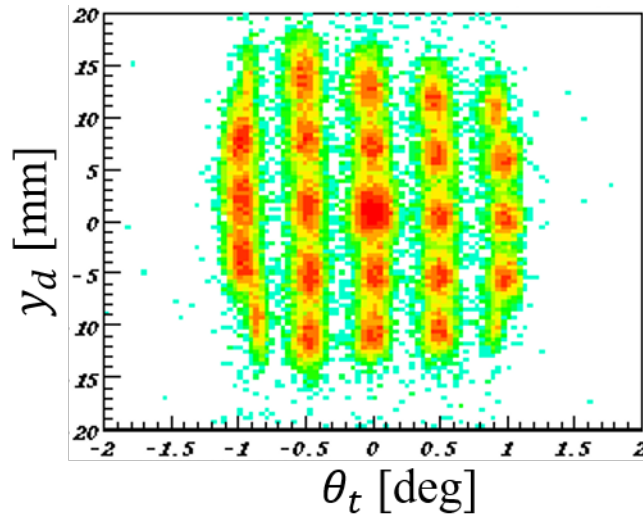


Figure 3.5: Horizontal scattering angle at the target position.

The calibration of the vertical scattering angle  $\phi$  is more complicated because it depends on not only the  $y$  but also horizontal parameters  $x$  and  $\theta$ . In the current analysis, I didn't calibrate the scattering angle  $\phi$  yet. Temporarily, the solid angle was obtained from another experiment (E398) whose experimental condition such as the beam energy and the scattering angle was the same as in our case [OUI17]. This assumption was verified from the fact that the differential cross sections of the  $1^+$  state at 15.11 MeV in  $^{12}\text{C}$  calculated from our experimental data and E398 were consistent. The solid angle of the full acceptance in  $\theta=0^\circ$  at the E398 experiment is shown in Fig.3.6.

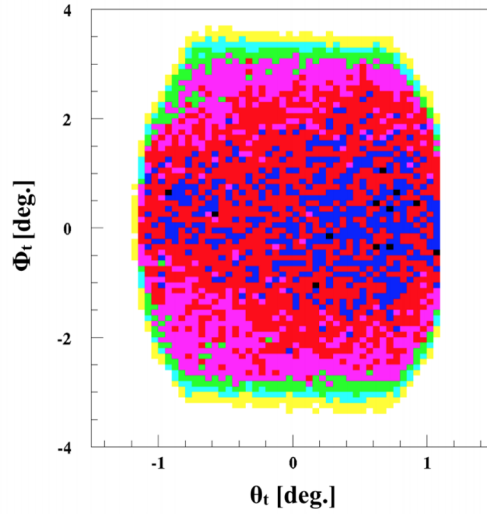


Figure 3.6: Scattering angle distribution in the E398 experiment[OUI17].

### 3.1.5 Optical correction and energy calibration

Ideally the scattered protons are focused horizontally at the focal plane in the mild under focus mode. In other words, the horizontal position  $x_d$  should be independent from the horizontal scattering angle  $\theta_t$  at the focal plane. However in reality, that's not the case because the higher order aberration is still remaining. Additionally, the kinematical correction is also required because we are in the laboratory system, namely the energy of the scattered protons depends on the scattering angle even if the proton is scattered with the same Q value. A two-dimensional histogram of the horizontal position  $x_d$  and the horizontal scattering angle  $\theta_t$  in  $^{12}\text{C}(p, p')$  without any corrections is shown in the left panel of Fig.3.7. An optical and kinematical correction was performed by the following equation

$$x_c = x_d + \sum_i^2 \sum_j^4 (x|x^i \theta^j) x_d^i \theta_t^j, \quad (3.6)$$

where  $c$  denotes the corrected position and other notations for  $x$  and  $\theta$  are defined in Fig.3.3 and Fig.3.4. The corrected histogram is shown in the right panel of Fig.3.7.

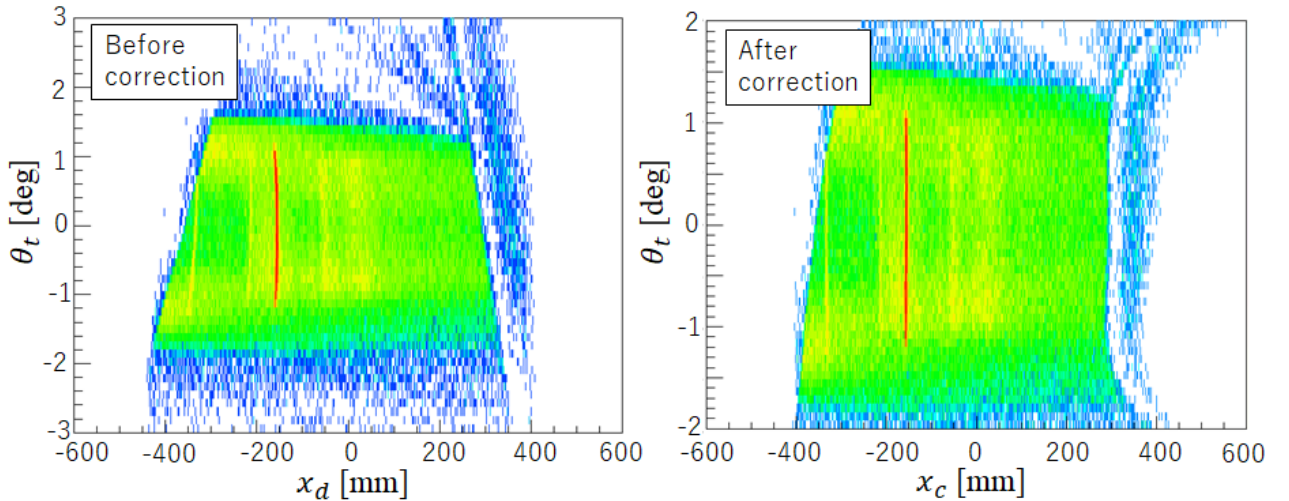


Figure 3.7: Comparison of the correlation between the horizontal position  $x$  before and after the correction in  $^{12}\text{C}(p, p')$ . The red locus at around  $x_d = -200$  mm is the  $1^+$  state at 15.11 MeV.

The data of the carbon target has several discrete states and they were used for the calibration of the excitation energy. The corrected horizontal position  $x_c$  was converted into the excitation energy by

$$Ex[\text{MeV}] = a + b \cdot x_c + c \cdot x_c^2. \quad (3.7)$$

Two different parameter sets were deduced for the above equation because the magnetic field of Grand Raiden was tuned once again to reduce the backgrounds during the measurement. The results are summarized in Tab.3.1.

Table 3.1: Parameters for the excitation energy calibration of Grand Raiden spectrometer. The upper is the one before the tuning and the lower is the one after the tuning.

	a	b	c
Before	22.641	0.04086	-0.0000039
After	21.534	0.04122	-0.0000016

Fig.3.8 shows the excitation energy spectrum in  $^{12}\text{C}(p, p')$  at zero degree after the energy calibration. The energy resolution was 200 keV in FWHM for the peak at 15.11 MeV. This resolution was worse than expected, but currently the excitation energy spectrum was divided into 1 MeV strips for the gamma ray analysis, thus this resolution was acceptable. Note that this figure contains only the true events. How to estimate and subtract background events is discussed in the following section.

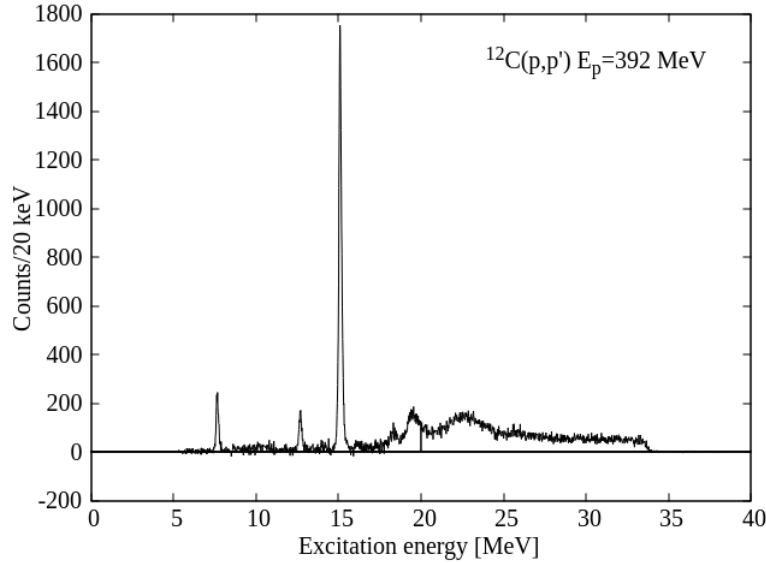


Figure 3.8: Excitation energy spectrum in  $^{12}\text{C}(p, p')$  at zero degree after optical and kinematical corrections, and energy calibration.

### 3.1.6 Background subtraction

Even after the beam tuning, background events still exist due to the multiple scattering in the target. This background events distributed homogeneously in the  $y$  direction, while the true events were focused at the center in the  $y$  direction of the focal plane coordinate. However, in case of under focus mode, the vertical focus point is shifted to downstream. In other words, the vertical position at the VDCs,  $y_d$  correlates with the vertical angle  $\phi_d$ . In order to distinguish the focused events from other events clearly, the vertical position  $y_d$  must be corrected. In reality,  $y_d$  depends not only  $\phi_d$  but also the  $x_d$  because of the complex ion optics of Grand Raiden spectrometer. Finally the  $y_d$  was

corrected by

$$y_c = y_d + \sum_{i,j}^2 (y|x^i\phi^j)x_d^i\phi_d^j. \tag{3.8}$$

Fitted parameters are summarized in appendix. Fig.3.9 shows a comparison between the vertical position distributions before the correction and after the correction. The central peak in the lower-right panel contains both of the true events and the background events, while the flat structure originates in the background events.

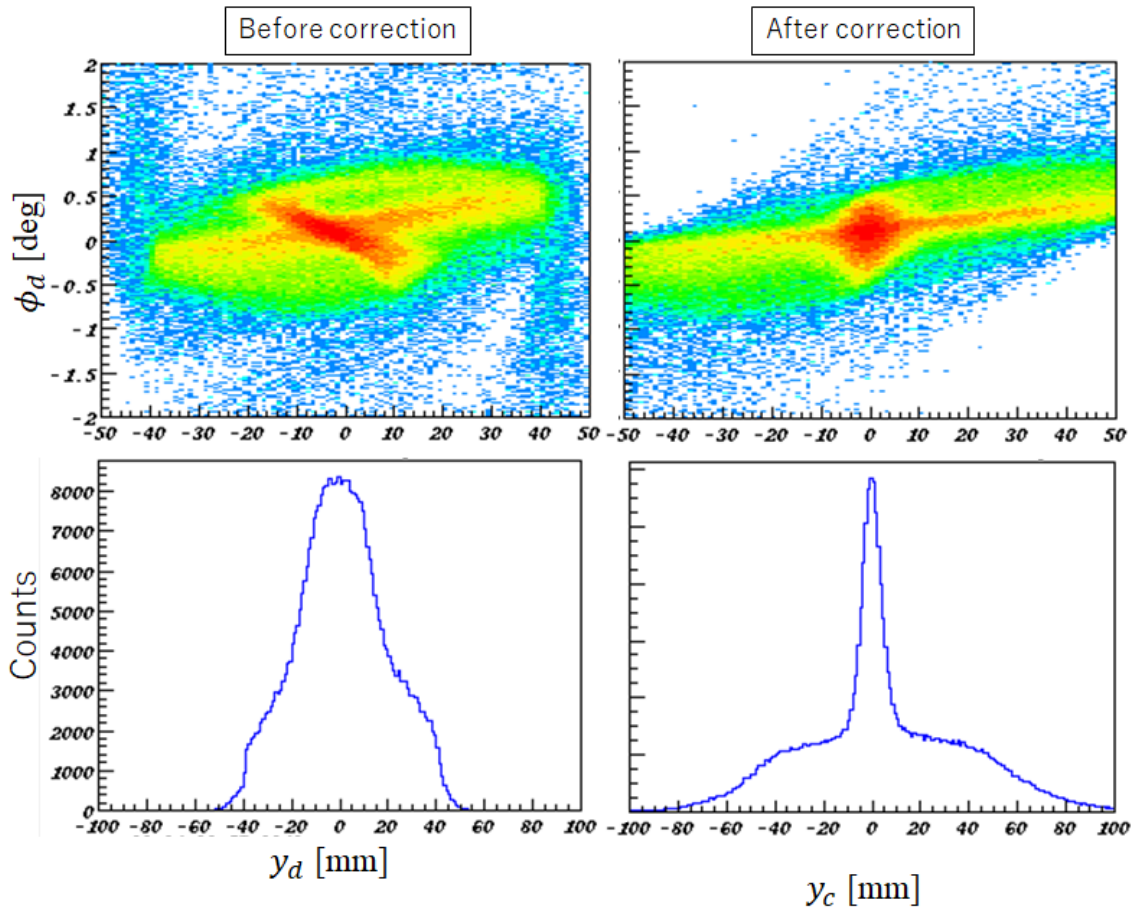


Figure 3.9: The left (right) panel is the corrected (uncorrected) spectrum of vertical position  $y$  for the  $^{12}\text{C}(p, p')$ . The data of  $^{90}\text{Zr}$  target was difficult to see the difference due to the bad S/N ratio.

The dependence of vertical position distribution upon the excitation energy was also studied. The results are shown in Fig.3.10. The distributions depends on the excitation energy, so different gates for true and background events were defined for each excitation energy region. Gates for the background events are drawn in Fig.3.10 with gray bands and gates for the the true events are drawn with pink bands. Each gray band has a half width of pink bands, thus taking a sum of both side bands, the number of backgrounds was estimated. Then the number of true events are extracted by subtracting the background events. The excitation energy spectra gated on each region are shown in Fig.3.11. Fig.3.12 shows the excitation energy spectrum which is subtracted background events.

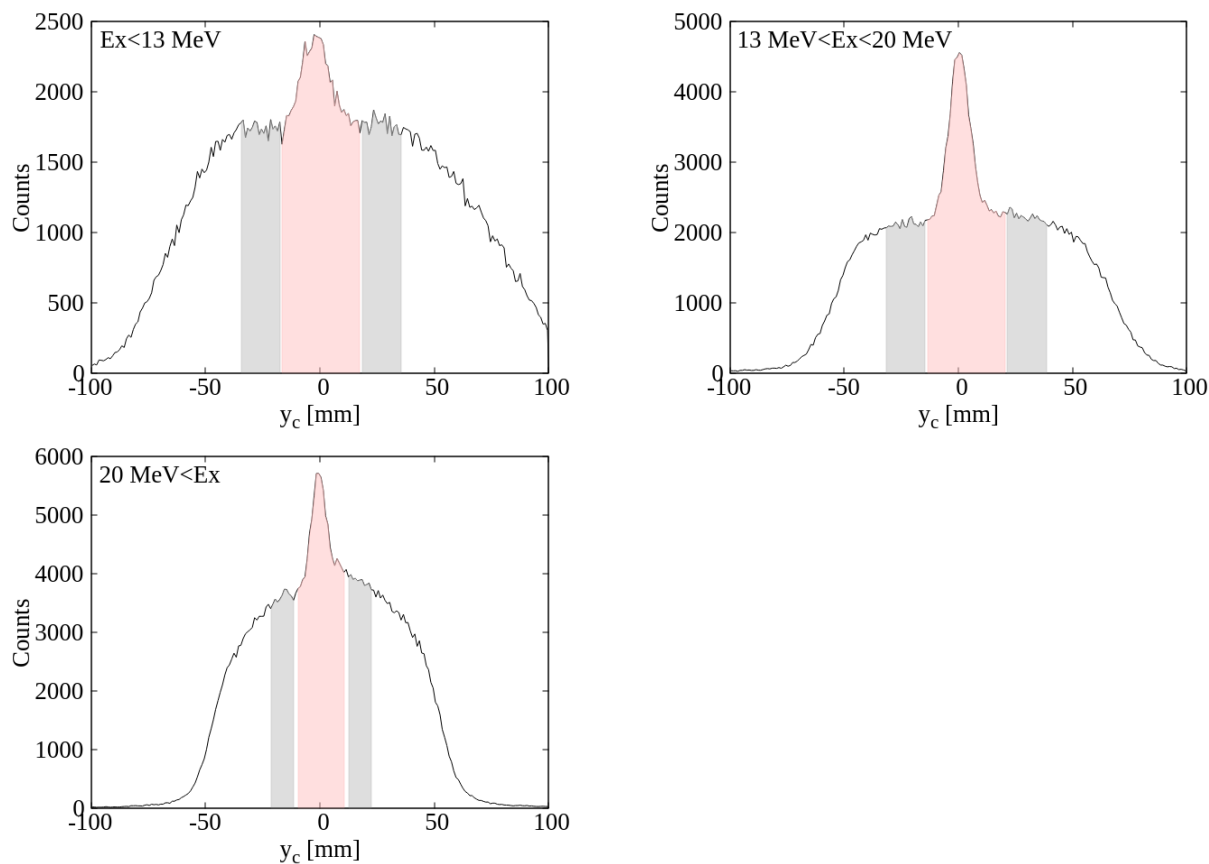


Figure 3.10: Corrected vertical position distribution for different excitation energy in the  $^{90}\text{Zr}(p, p')$ .

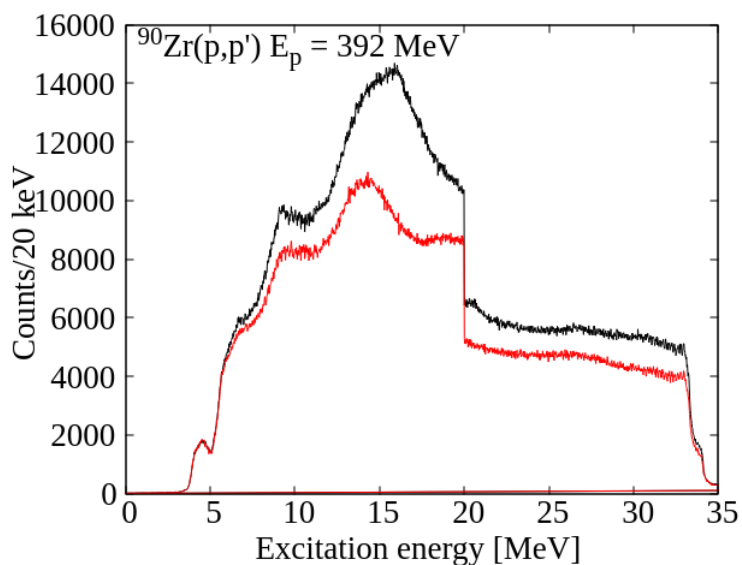


Figure 3.11: Excitation energy spectrum in  $^{90}\text{Zr}$  gated on the background (black) and true (red) events. Above the excitation energy of 20 MeV, the narrower gate was applied (see Fig.3.10). Therefore the number of event

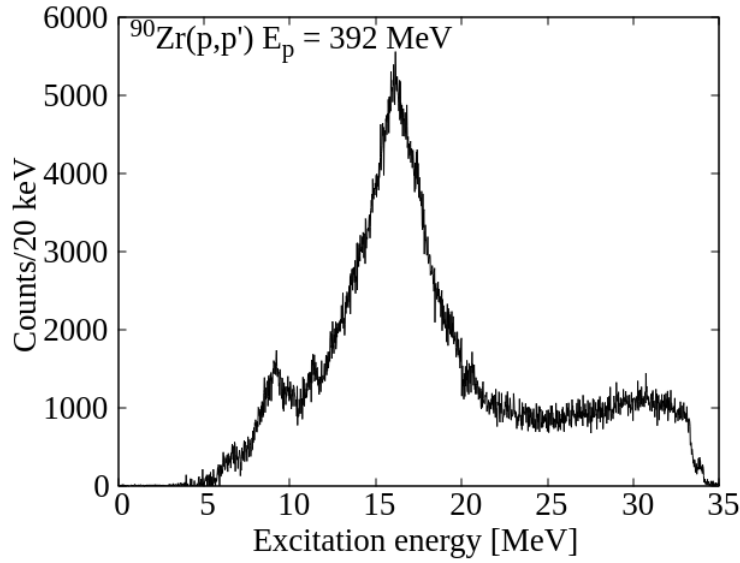


Figure 3.12: Excitation energy spectrum in  $^{90}\text{Zr}(p, p')$  after background subtraction.

## 3.2 Analysis of $\gamma$ ray detectors

### 3.2.1 $\gamma$ ray energy calibration

Energy for gamma rays in the  $\text{LaBr}_3$  detectors was calibrated with the data of gamma ray sources,  $^{137}\text{Cs}$  and  $^{60}\text{Co}$ . In the beginning of analysis, the gamma ray energy was calibrated with only these radioactive sources. However these gamma rays cover just up to 1.3 MeV, so this calibration data was not applicable in the high energy region.

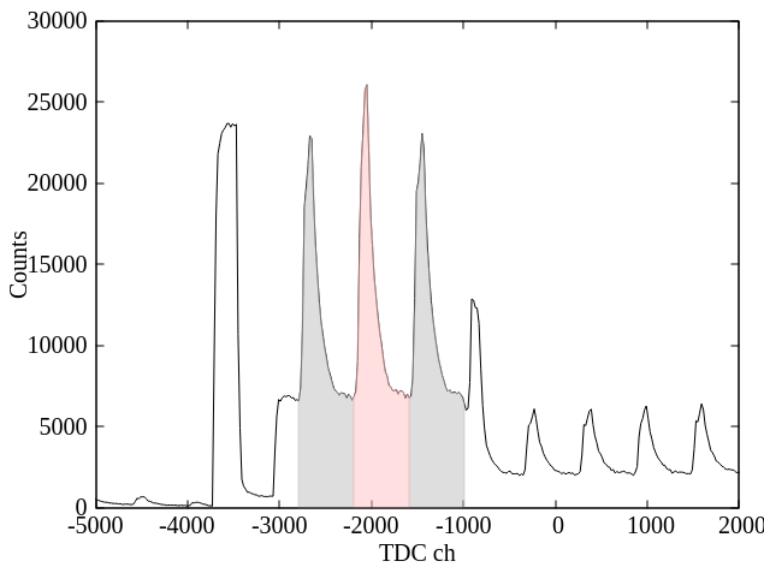
The data of the carbon target was used to calibrate the high energy region gamma ray. The  $1^+$  state at 15.11 MeV in  $^{12}\text{C}$  is populated strongly by  $(p, p')$  at zero degree and decays to the ground state directly following the gamma ray with the probability of 88.3% [KEL17]. Due to the small statistics, it was impossible to separate the photo peak from the single escape peak and the double escape peak. A response function of the  $\text{LaBr}_3$  detectors simulated by Geant4 code was used to get the channel of the 15.11 MeV peak. Finally the gamma ray energy was calibrated by the following quadratic function,

$$E_\gamma[\text{MeV}] = a + b \cdot \text{ADC}[\text{ch}] + c \cdot \text{ADC}[\text{ch}]^2. \quad (3.9)$$

The parameter sets are summarized in appendix.

### 3.2.2 Background subtraction

Coincidence data between  $\text{LaBr}_3$  and Grand Raiden were taken with a coincidence width of 150 nsec which included three beam bunches(Fig.3.13). In Fig.3.13, three major peaks correspond to self-triggered events. The trigger for  $\text{LaBr}_3$  DAQ was generated by OR trigger from eight  $\text{LaBr}_3$  detectors. Other minor peaks are the events triggered by other  $\text{LaBr}_3$  detectors. The center peak in Fig.3.13 painted with pink is the prompt events, while the side peaks painted with gray are the randomly coincided events, namely background events. Gamma ray was emitted immediately (of the order of  $< \text{fs}$ ) after the excitation of the nucleus compared with the cyclotron frequency (of the order of 10 ns), so the true gamma decay events are existed in the prompt peak. However the prompt peak contains not only true gamma decay events but also background events. Taking an average of both random coincidence peaks, the number of background events was estimated. Then the number of truly coincided gamma rays was obtained by subtracting the averaged number of random coincidence events from the prompt events.

Figure 3.13: LaBr<sub>3</sub> timing spectrum for slot number 1.

For example, the gamma ray spectra from the  $1^+$  state at 15.11 MeV in  $^{12}\text{C}$  taken by the LaBr<sub>3</sub> detector at the slot number 1 with each timing gate are depicted in Fig.3.14. The red (blue) spectrum is the events gated on the left (right) random coincidence events in Fig.3.13. Fig.3.15 is the gamma ray energy spectrum after the background subtraction.

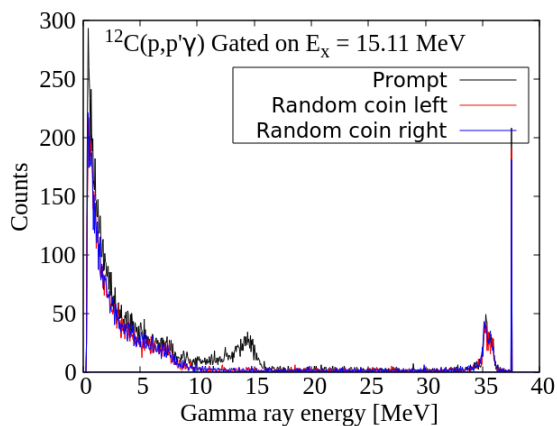


Figure 3.14: Gamma ray spectra gated on each timing gate.

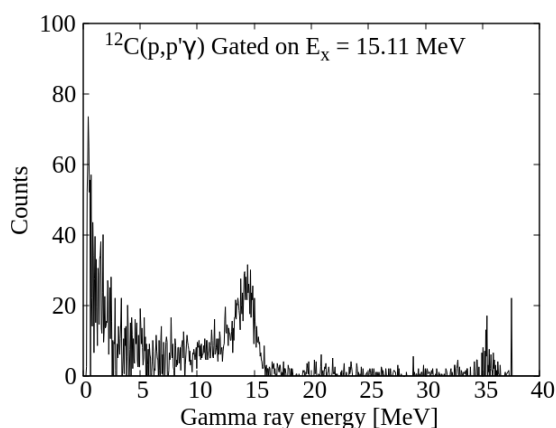


Figure 3.15: Gamma ray spectrum after BG subtraction

Two dimensional coincidence matrix in  $^{90}\text{Zr}(p, p')$  between Grand Raiden spectrometer and LaBr<sub>3</sub> detectors after BG subtraction is shown in Fig.3.16. The diagonal region indicates the ground state decay gamma rays. By selecting this diagonal region and then projecting onto the x axis, gamma ray energy spectrum for ground state decay was obtained (Fig.3.17).

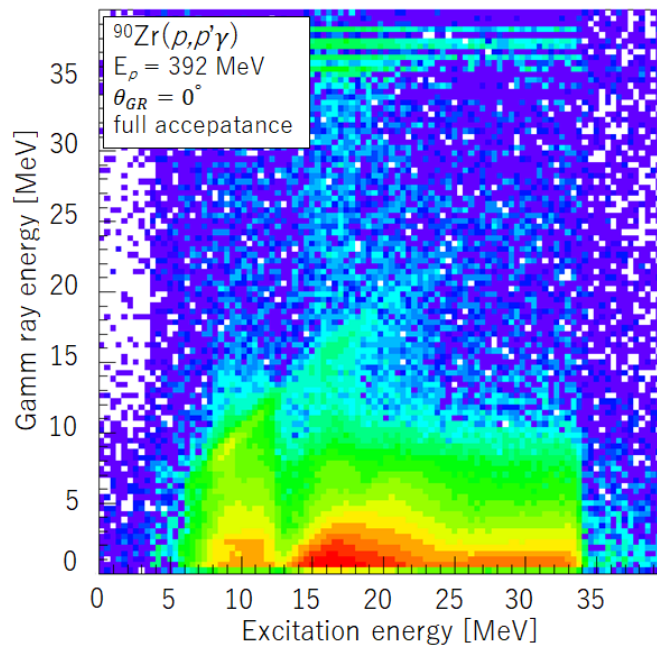


Figure 3.16: Coincidence matrix between Grand Raiden and LaBr<sub>3</sub> in the  $^{90}\text{Zr}(p, p'\gamma)$ .

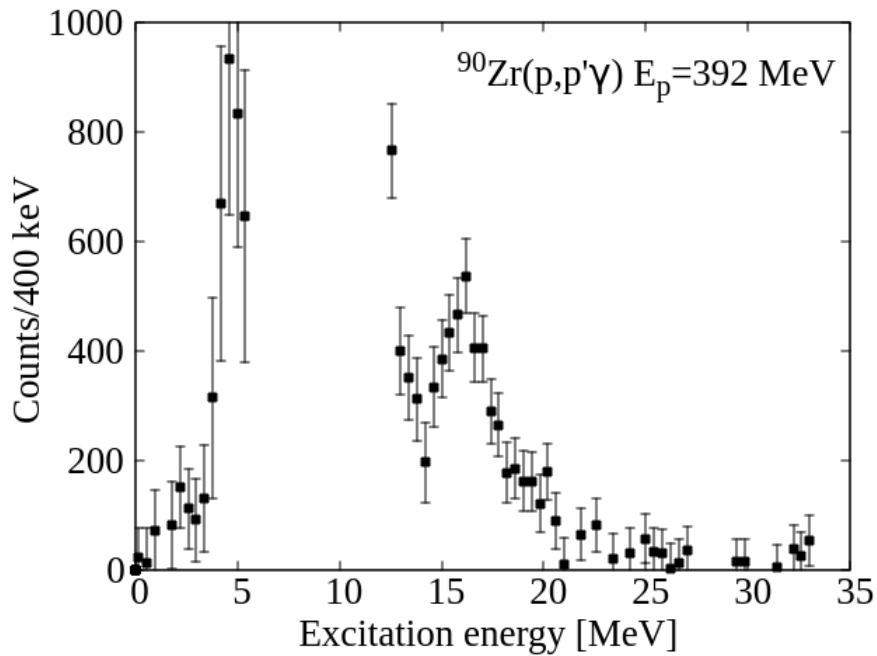


Figure 3.17: Ground state gamma decay energy spectrum.

### 3.2.3 Estimation of the number of gamma ray using Geant4 simulation code

In order to estimate the number of emitted gamma rays, a response function of the LaBr<sub>3</sub> detector was simulated by Geant4 simulation code [AGO03] [ALL06] [ALL16]. Geant4 is a toolkit for the Monte Carlo simulation of the passage of particles through matter. The simulated geometry is shown in Fig.3.18. Experimental condition was almost reproduced just except for veto plastic detectors which were installed between a LaBr<sub>3</sub> detector at 90° and an absorber. Since now we are interested in the high

energy gamma ray which is equal to the excitation energy of the GDR, the effect of plastic scintillators is expected to be negligible (less than  $10^{-2}$ ).

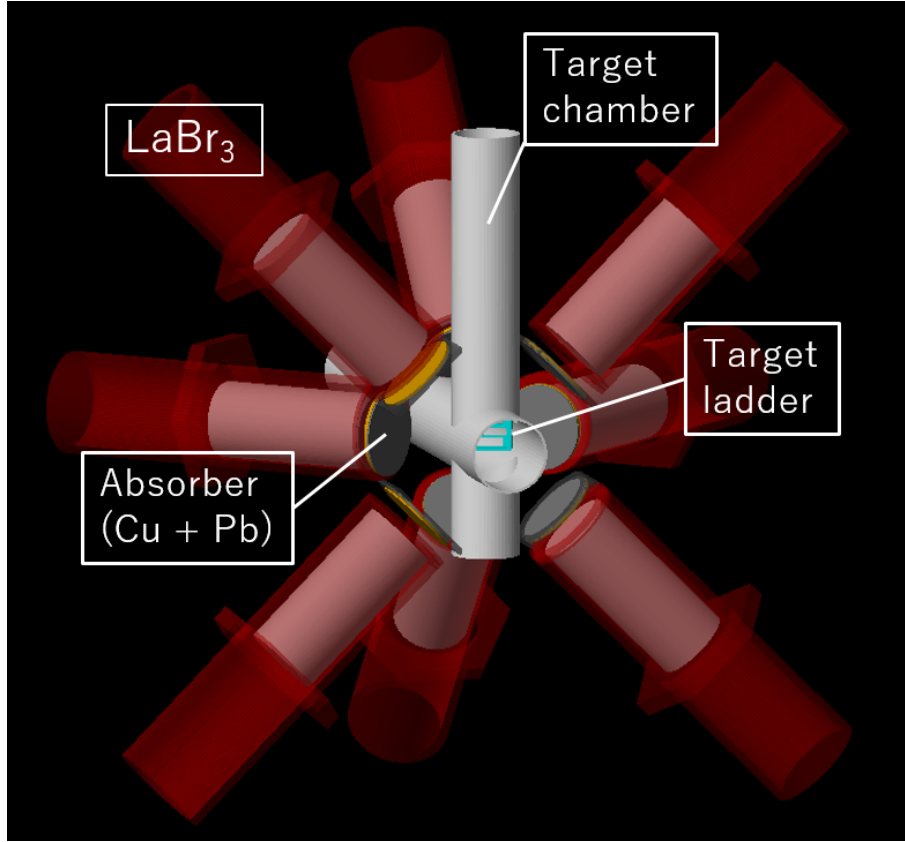


Figure 3.18: Geometry in Geant4 simulation. The geometry was loaded through the CADMesh[[POO12](#)].

At first a response function  $h(E, E')$  was simulated with infinitely good intrinsic resolution of the  $\text{LaBr}_3$  detectors (Fig.3.19). Here,  $E$  is the energy of emitted gamma ray from the target nucleus and  $E'$  is the detected energy in the  $\text{LaBr}_3$ , namely the horizontal axis in the energy spectrum. Then this simulated spectrum  $h(E, E')$  was fitted to the experimental data convoluting with a gaussian  $g(E, E', b)$ , where  $b$  is a fitting parameter which is related to the width of the gaussian by,

$$FWHM(b, E') = \sqrt{a + bE' + cE'^2}. \quad (3.10)$$

Parameters  $a$  and  $c$  in Eq.3.10 are constants, they are 400 and  $28 \times 10^{-6}$  in keV, respectively[[GIA13](#)]. Physical meaning of " $a$ " is the noise that is irrelevant with the detected energy and " $b$ " comes from the statistical fluctuation and the " $c$ " represents the gain drift effects. In addition to the fitting parameter  $b$ , a scaling factor  $s$  was also introduced to adjust the height of fitting function. Finally, the fitting function  $f(E)$  was given by

$$f(E) = s \times \int g(E, E', b)h(E, E')dE'. \quad (3.11)$$

For example, one of the fitting results in  $^{12}\text{C}(p, p')$  is shown in Fig.3.19. The fitting area was from 10 MeV to 17 MeV.

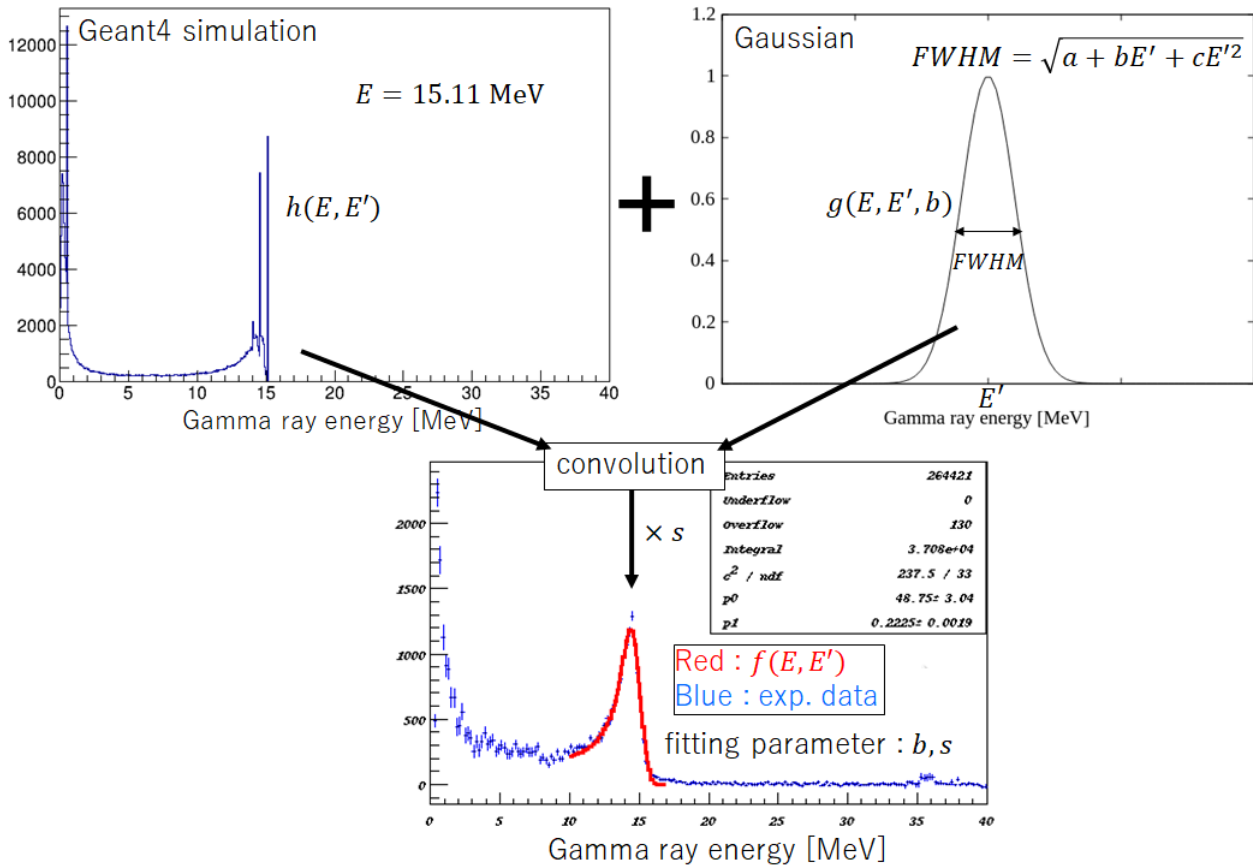


Figure 3.19: Fitting result in the case of 15.11 MeV gamma ray from the carbon target. The data is summed up by all of detectors, slot 1-8.

The number of emitted gamma ray from the target nucleus was calculated by multiplying the number of simulated gamma ray by scaling factor  $s$ . The rightness of this simulation code was studied by comparing the detection efficiency of gamma rays with experimental data and the result in the paper published by Milano group [GIA13].

### Determination of fitting parameter $b$

Fitting of gamma rays from the GDR was not straightforward due to the small statistics. Therefore, I limited the range of the fitting parameter  $b$  based on the data of the carbon target. Fitting of carbon data was performed with small uncertainty as seen in Fig.3.19, and its dependence upon the runs was studied. First, the fitting parameter  $b$  for the gamma ray from the  $1^+$  state at 15.11 MeV in carbon was studied for each run. Fig.3.20 shows the trend of the parameter  $b$  during the experiment. According to this result, the upper limit and the lower limit of parameter  $b$  were determined as 130 and 40, respectively. Gamma rays from the GDR in  $^{90}\text{Zr}$  was analyzed within this range of parameter. It seems that the parameter  $b$  changes systematically. One of possible reasons is the gain shift caused by one or some of  $\text{LaBr}_3$  detectors because the data is analyzed after summing up by all of detectors, slot 1-8.

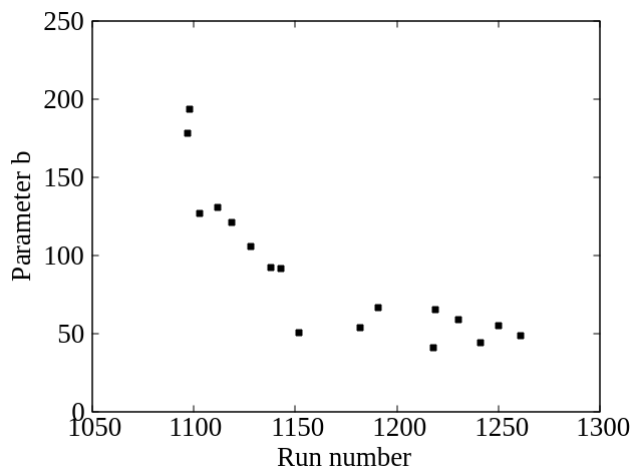


Figure 3.20: Trend of fitting parameter  $b$  for the gamma rays from the  $1^+$  state at 15.11 MeV in  $^{12}\text{C}$ .

When we summed up the gamma ray data at the different angles, the Doppler shift may affect the energy resolution. However, in this experiment the effect of the Doppler shift was negligible because the target nucleus was much heavier than the projectile and the scattering angle was restricted to the extremely forward angles. For example, in case of the 15.11 MeV gamma ray in  $^{12}\text{C}(p, p'\gamma)$ , the energy difference between the detected energy at  $90^\circ$  and the detected energy at the  $135^\circ$  is just 50 keV, much less than 1%. Compared with the typical energy resolution of the LaBr<sub>3</sub> detector during this experiment, 4% at 15.11 MeV, the Doppler shift effect was enough small to be ignored.

### 3.2.4 Confirmation of the simulated results and correction factor

#### Comparison with the paper

In order to confirm the reliability of the simulation code, my simulated efficiency and the simulated efficiency by Milano group was compared (Fig.3.21). Here, the efficiency indicates the photo peak efficiency even if there are single and double escape peaks. In this simulation, the gamma ray was emitted at 20 cm away from the surface of the detector and any absorbers and a scattering chamber were not included.

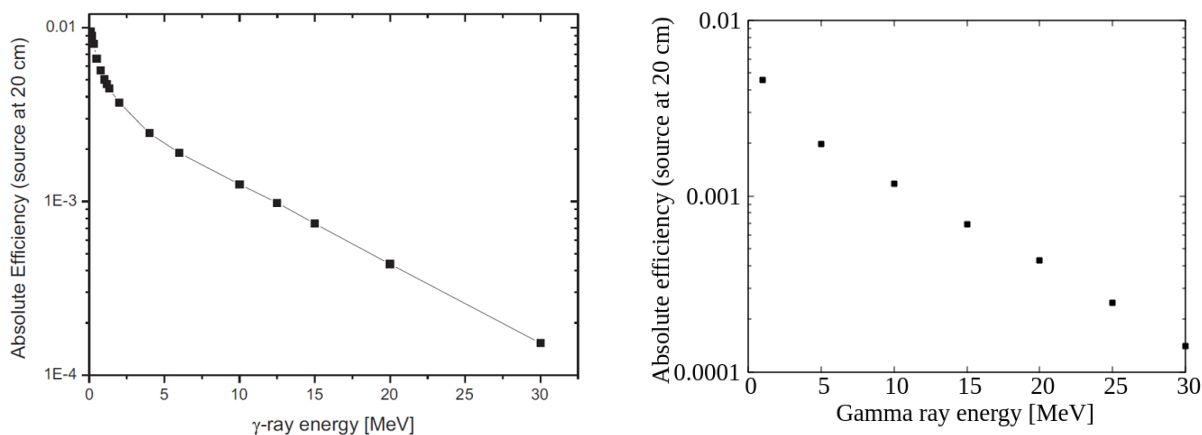


Figure 3.21: The right panel is the data from [GIA13] and the left panel is the current simulated efficiency.

As can be seen, the two simulation results are consistent. For example, at the energy of 15 MeV they agree in 10%. Strictly speaking, below the energy of 5 MeV my result seems to underestimate the efficiencies compared with the one by Milano group, roughly 20%.

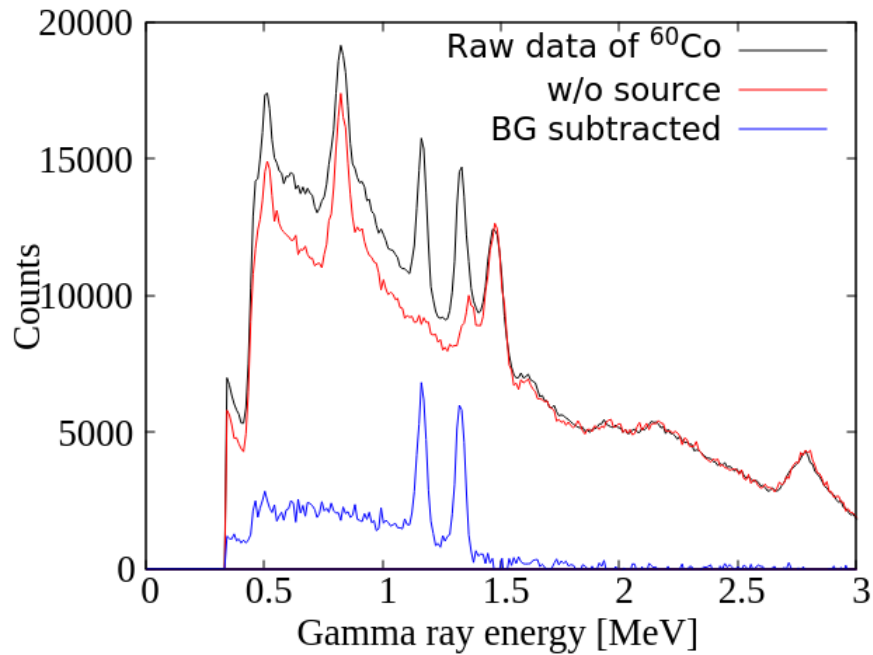
**Comparison with the radioactive source data**

Figure 3.22: Gamma ray spectrum of  $^{60}\text{Co}$  taken by the slot number 1.

Next, my simulation result and the experimental data were compared. The data of the radioactive source  $^{60}\text{Co}$  are drawn in Fig.3.22. The number of detected events was counted by fitting the peak with a gaussian after subtracting the background events. The background data was measured without any radioactive sources. However, several peaks and a structure were seen in the energy spectrum which arise from the internal activity of the  $\text{LaBr}_3$  detectors and the radioactivation of surrounding stuff. The background data was normalized to reproduce the height of the internal radioactivity peak at 1.4 MeV. Even after the BG subtraction, some backgrounds remained especially in the low energy side. This is because of the dependence of activation backgrounds on time. The resulted efficiency for several gamma ray sources is plotted in Fig.3.23 for each  $\text{LaBr}_3$  detector with the data obtained from Geant4 simulation. There is a discrepancy between the source data and the simulated result. The reason is not fully understood yet, but it may comes from the incompleteness of simulation geometry. On average, the experimental data was less than the simulated result by 12-25%.

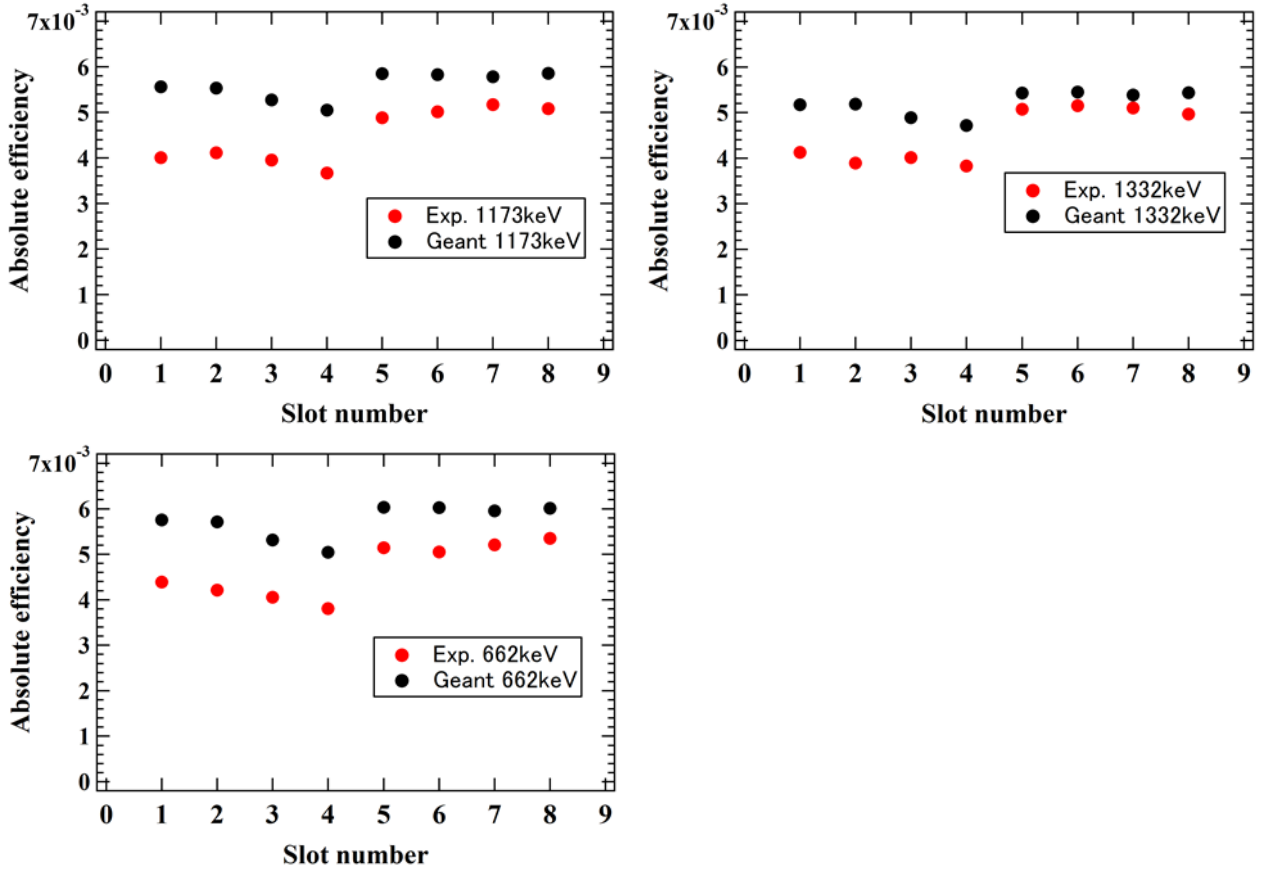


Figure 3.23: Comparison between the simulated efficiency and the experimental data.

### Comparison with the carbon data and correction factor

The gamma decay from the  $1^+$  at 15.11 MeV in  $^{12}\text{C}$  was also used for the calibration of the gamma ray efficiency because its branching ratio is well studied, 88.3% [KEL17]. Furthermore the angular distribution of emitted gamma rays in  $^{12}\text{C}(p, p')$  is known because its population for different magnetic substates was already studied by A.Tamii from the spin transfer measurement [TAM00]. Tab.3.2 shows the result of population in  $1^+$  state at 15.11 MeV in  $^{12}\text{C}$ . The experimental condition was same as our case,  $E_p=392$  MeV and scattering angle was zero degree.

Table 3.2: The population of the magnetic substates in  $1^+$  state at 15.11 MeV in  $^{12}\text{C}$ . [TAM00]

Magnetic quantum number, m	Probability [%]
1,-1	79±1
0	21±1

The corresponding angular distribution  $W(\theta)_l^m$  from each magnetic substate are given by

$$W(\theta)_1^0 = P_1^0 \cdot \frac{3}{2} \sin^2(\theta) \quad (3.12)$$

$$W(\theta)_1^{\pm 1} = P_1^{\pm 1} \cdot \frac{3}{4} (1 + \cos^2(\theta)), \quad (3.13)$$

where  $p_l^m$  is the population for each substate and the theta is the polar angle with respect to the beam direction. Fig.3.24 shows the resulted angular distribution of gamma ray from the the  $1^+$  state at 15.11 MeV in  $^{12}\text{C}$ .

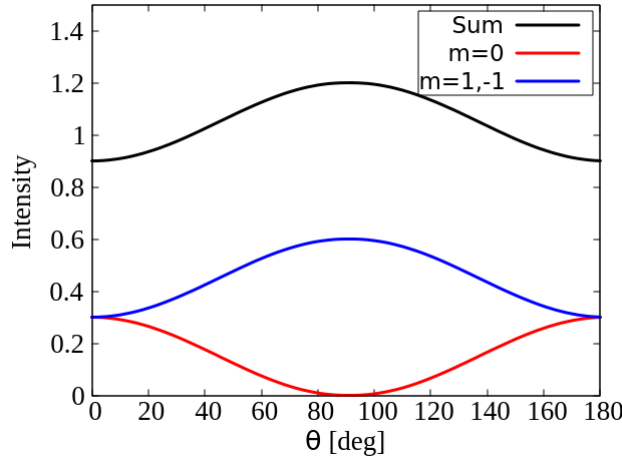


Figure 3.24: The angular distribution of emitted gamma ray from the  $1^+$  state at 15.11 MeV in  $^{12}\text{C}$ .

Based on this angular distribution, the ground state gamma decay branching ratio of  $1^+$  state at 15.11 MeV in  $^{12}\text{C}$  was compared with the reference value, 88.3%. However the branching ratio which was calculated from the experimental data and the simulation data was just half of the reference value. The reason of this discrepancy was not revealed yet, and thus the correction factor was introduced to reproduce the reference value. The correction factor  $c$  was given by,

$$c_i = \left( \frac{N_{sim} \cdot s_i}{N_{GR} \cdot \eta} \right)^{-1} \times B.R.ref. \times W_1(\theta), \quad (3.14)$$

where  $i$  denotes the slot number of the  $\text{LaBr}_3$  detectors and the parameters are summarized in Tab.3.3.

Table 3.3: Variables entering into Eq.(3.14).

$N_{GR}$	yield for $1^+$ state at 15.11 MeV in $^{12}\text{C}$	
$N_{sim}$	the number of emitted gamma rays in the simulation	
$s_i$	scaling factor for the $\text{LaBr}_3$ detector at the slot number $i$	
$c_i$	correction factor for the $\text{LaBr}_3$ detector at the slot number $i$	
$\eta$	effective GR prescale factor	
$B.R.ref.$	reference value of the gamma decay branching ratio	88.3% [KEL17]
$W_1(\theta)$	angular distribution of emitted gamma ray (Fig.3.24)	

Fig.3.25 shows the trend of the correction factor for the  $1^+$  state at 15.11 MeV in  $^{12}\text{C}$  in slot number 1. Each uncertainty was much smaller (of the order of a few %) than the fluctuation of each point. Therefore after taking the average, its uncertainty was calculated by

$$\sigma = \sqrt{\frac{\sum_i^N (x_i - \mu)^2}{N(N-1)}}, \quad (3.15)$$

where the  $\mu$  is the averaged correction factor,  $x_i$  is the each correction factor and  $N$  is the number of data points. Fig.3.26 represents the result of the correction factor for each detector. We are not sure about why the correction factor fluctuates drastically and why it clearly depends on the angle of the  $\text{LaBr}_3$  detectors. The origin of those should be sought in the future.

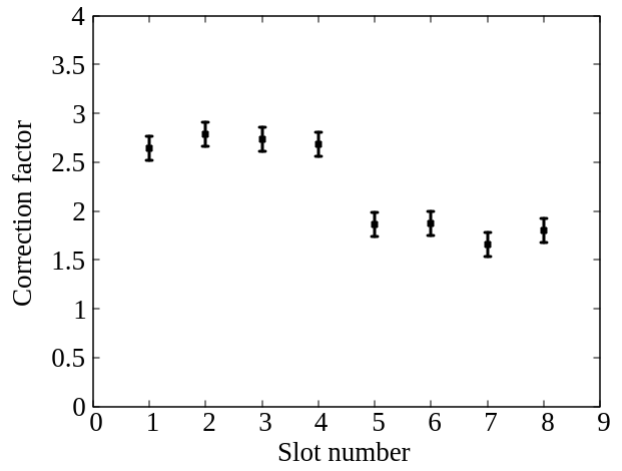
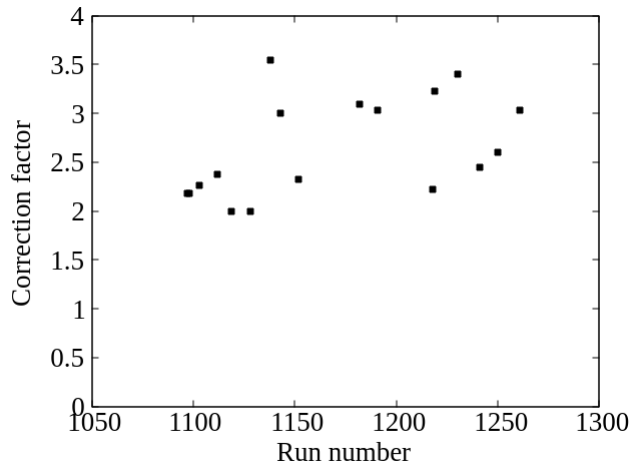


Figure 3.25: Trend of correction factor for slot number 1.

Figure 3.26: Averaged correction factor for each slot number.

## Chapter 4

# Results

### 4.1 Extraction of B(E1)

#### 4.1.1 Double differential cross section of $(p, p')$ at zero degree

Double differential cross sections are extracted using the equation

$$\frac{d^2\sigma}{d\Omega dE} = \frac{1}{\Omega_{lab}} \frac{N_{GR}}{N_{beam}} \frac{1}{L\eta\epsilon} \frac{A}{N_A t \zeta} J. \quad (4.1)$$

The experimental parameters for Eq.(4.1) are summarized in Tab.4.1. The target thickness is divided by a factor of  $\cos(22.5^\circ)$  because the target ladder was tilted by  $22.5^\circ$ .

Table 4.1: Variables entering into Eq.(4.1), and their values.

$\Omega_{lab}$	solid angle in the laboratory frame	0.00415	sr
$N_{GR}$	yield for the specific energy bin		Counts/MeV
$N_{beam}$	total beam current		
$L$	DAQ live time ratio	51	%
$\eta$	effective GR prescale factor	27	
$\epsilon$	VDC efficiency	90-92	%
$A$	target atomic weight	90	g/mol
$N_A$	Avogadro number	$6.023 \times 10^{23}$	1/mol
$t$	target thickness	$20.0 / \cos(22.5^\circ)$	mg/cm <sup>2</sup>
$\zeta$	target enrichment	97.65	%
$J$	Jacobian from lab to CM system		

$N_{GR}$  is the number of events taken with a trigger "GR single sampling" (see Sec.2.4). In the present analysis, the solid angle was determined based on the previous work [OUI17] as mentioned in Sec.3.1.4. The solid angle will be determined from our data in the future. The DAQ live ratio was obtained by dividing the number of "GR trigger live" by the number of "GR trigger" and the effective GR prescale factor was deduced by dividing the number of "GR single sampling" by the number of "GR trigger live". This effective GR prescale factor was larger than the set value in the prescale module because some of "GR trigger live" events were flew into the coincidence events.

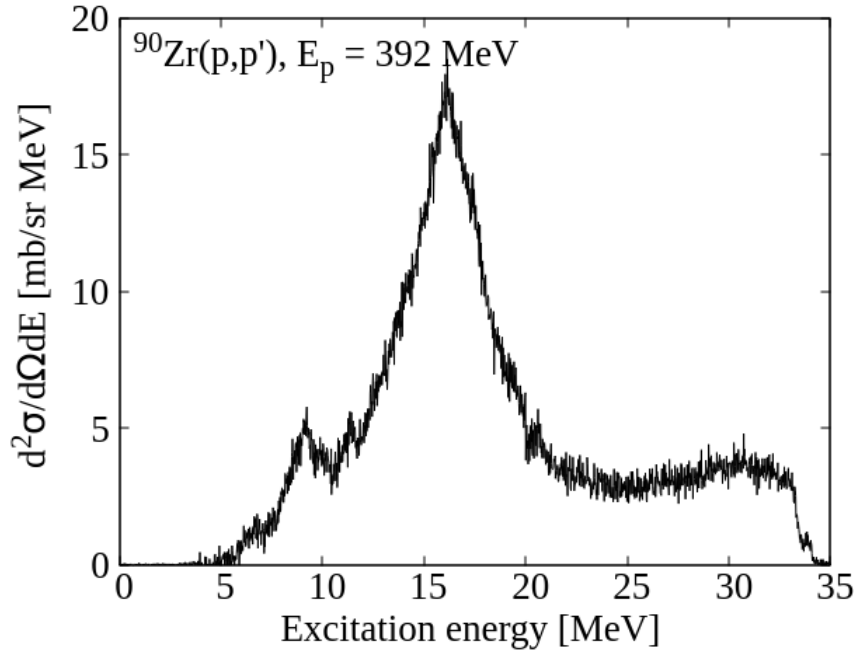


Figure 4.1: Double differential cross section in  $^{90}\text{Zr}(p,p')$  at zero degree and full angular acceptance of the spectrometer.

#### 4.1.2 Result of B(E1)

The B(E1) was calculated by

$$\frac{dB(E1)}{dE} = \frac{9\hbar c}{16\pi^3} \frac{d^2\sigma}{d\Omega dE} \times \frac{1}{\frac{dn_{E1}}{d\Omega}}, \quad (4.2)$$

where  $\frac{dn_{E1}}{d\Omega}$  is the number of virtual photons to populate an E1 excitation, whose theoretical background is discussed in Sec.1.4.2 and the  $\frac{d^2\sigma}{d\Omega dE}$  is the double differential cross section for E1 excitation. In the calculation of virtual photon, the eikonal approximation was applied in the present analysis. The result of calculated virtual photons is plotted in Fig.4.2 as a function of the photon energy. In this figure, the number of virtual photons was averaged in the region of scattering angle 0-3 degree.

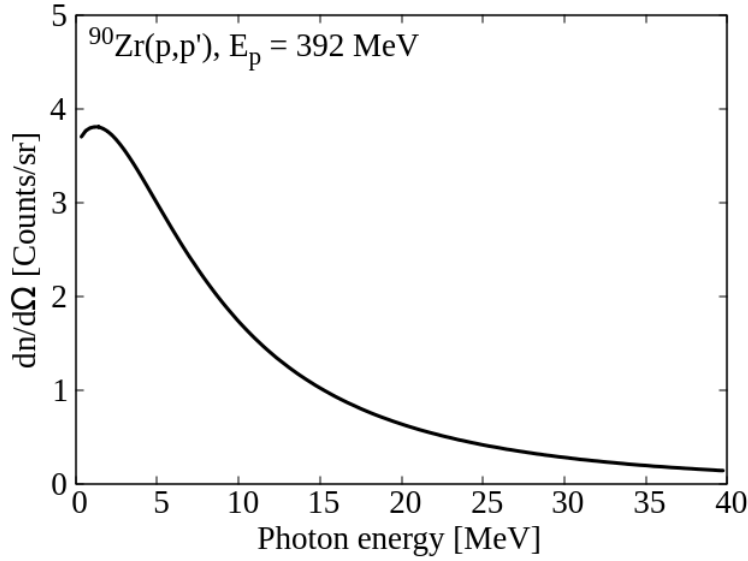


Figure 4.2: Distribution of the averaged number of virtual photons in  $^{90}\text{Zr}(p, p')$  in  $\theta_{cm} = 0\text{-}3$  degree.

In the strict sense, the double differential cross section in  $(p, p')$  at zero degree contains not only the E1 excitation but also other kinds of excitation like M1 and E2. One of methods to extract the E1 cross section is known as Multipole Decomposition Analysis (MDA) which is based on the DWBA with a phenomenological nuclear potential. We can perform the MDA within the solid angle for this experiment, but the determination of scattering angle is not completed yet. Currently, we assumed that the E1 excitation is dominant in the GDR region, excitation energy of 12-20 MeV. In the PDR region, the E1, M1 and E2 excitation were separated by Iwamoto *et al.* [IWA12]. Fig.4.3 shows the resulted cross section for E1 and M1 excitation and it was found that the M1 component has approximately twice than the E1 excitation cross section in the PDR region. Another paper related with MDA near the zirconium mass region was written by Martin [MAR13]. According to this paper, the M1 component is increasing gradually as the excitation energy increases (Fig.4.4). For instance, at the excitation energy of 20 MeV, the M1 component occupies more than half of the total cross section in  $(p, p')$  at zero degree. Note that the proton energy in these above two experiments was different from our case. In our case the energy was 392 MeV.

Consequently we decided to assume that the GDR region is dominated by the E1 excitation. With this assumption, the  $B(E1)$  was deduced by dividing the coulomb excitation cross section by the number of virtual photons. The result is shown in Fig.4.5.

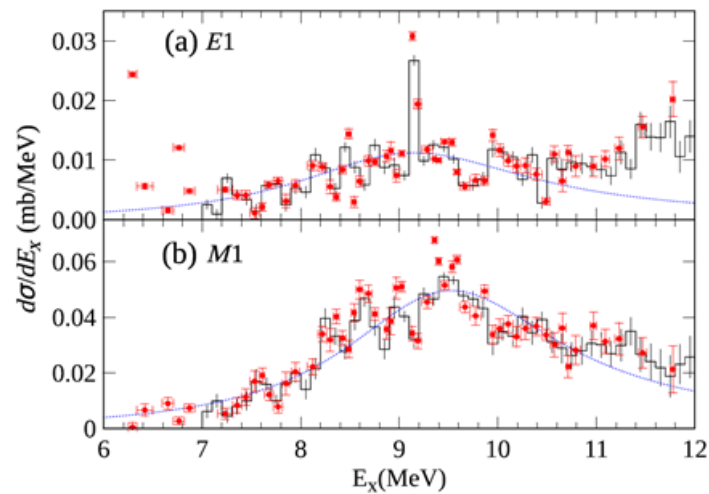


Figure 4.3: Separation of the E1 excitation cross section in  $^{90}\text{Zr}$  by MDA [IWA12].

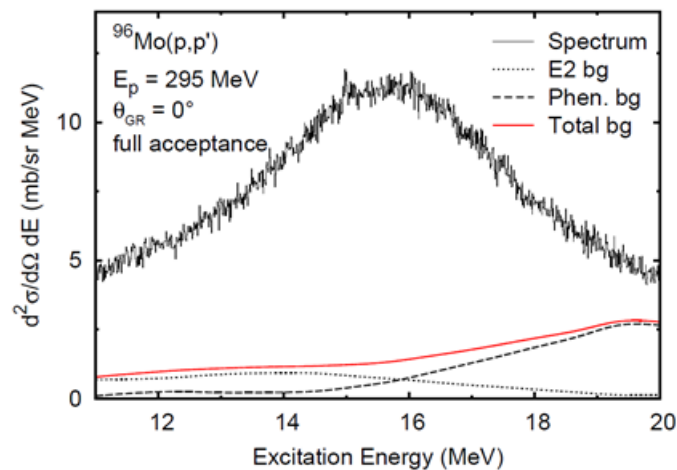


Figure 4.4: BG distribution in  $^{96}\text{Mo}(p, p')$  at zero degree by MDA [MAR13].

The B(E1) in the high energy region is increasing drastically. One of reasons is that underestimation of backgrounds as mentioned in Sec.3.1.6. Another reason is that not only the E1 but E2 and M2 transitions strength are expected to exist in this region as discussed above. Thus, MDA and more careful analysis are desired in order to understand this enhancement at high energy region.

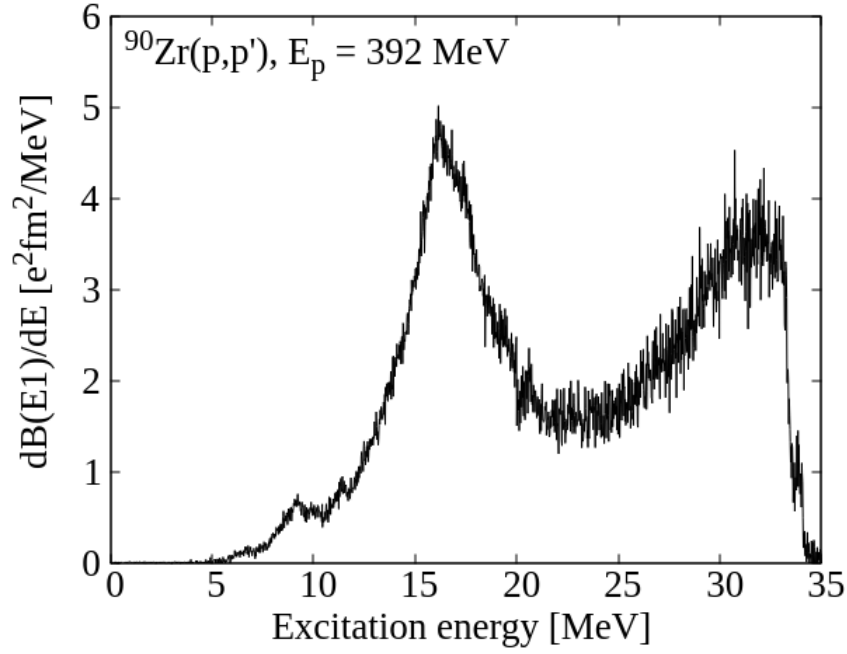


Figure 4.5:  $B(E1)$  in  $^{90}\text{Zr}$  obtained from a cross section of coulomb excitation.

### Comparison with photo-absorption cross section from $(\gamma, xn)$ experiment

Once obtaining the  $B(E1)$ , the photo absorption cross section is deduced by

$$\sigma_{\gamma}^{E1}(E_{\gamma}) = \frac{16\pi^3}{9} \left( \frac{E_{\gamma}}{\hbar c} \right)^2 \frac{dB(E1)}{dE_{\gamma}}. \quad (4.3)$$

This resulted cross section was compared with the  $(\gamma, xn)$  cross section which is almost equal to the photo absorption cross section because neutron decay is dominant channel (Fig.4.6). The present cross section is larger than the one obtained from the  $(\gamma, xn)$  by roughly 50%. The reason is not clear but it follows the behavior up to the energy of 21 MeV. Therefore the absolute value of present analysis may not be reliable enough, but the overall structure around the GDR region is somehow reliable.

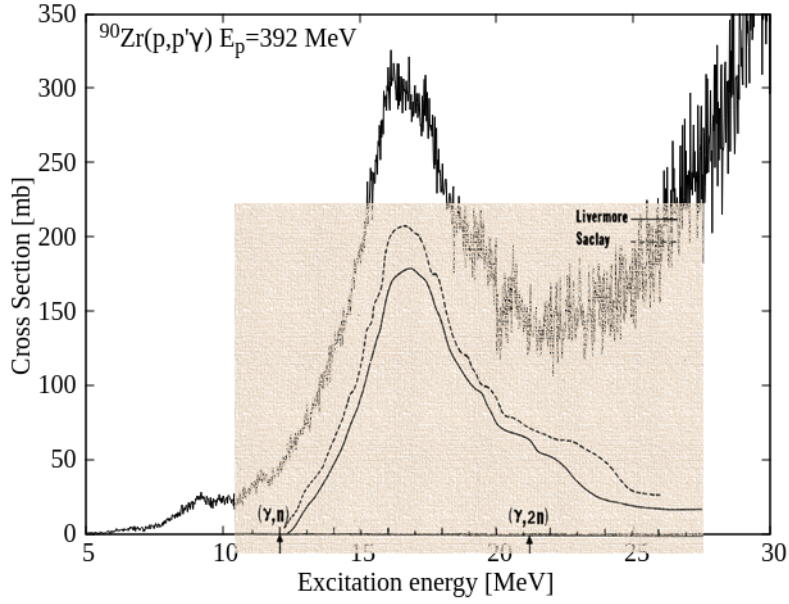


Figure 4.6: Comparison between the preset resulted photo-absorption cross section and that from the  $(\gamma, xn)$  experiment that is shaded with light orange.[BER75]

## 4.2 $\gamma$ rays from the GDR

### 4.2.1 Branching ratio of ground state $\gamma$ decay

The branching ratio (B.R.) was calculated by

$$B.R. = \frac{N_{sim} \cdot s \cdot c_{ave.}}{N_{GR} \cdot \eta}. \quad (4.4)$$

The parameters are summarized in the below table.

Table 4.2: Variables entering into Eq.(4.4).

$N_{GR}$	yield for the specific energy bin
$N_{sim}$	the number of emitted gamma rays in the simulation
$s_{sum}$	scaling factor for all the detectors (see Sec.3.2.3)
$c_{ave.}$	averaged correction factor
$\eta$	effective GR prescale factor

Other parameters which were appeared in Eq.4.1, such as VDC efficiency and target thickness are cancelled out with the data of  $\text{LaBr}_3$ . After summing up the data of all the  $\text{LaBr}_3$  detectors 1-8, the gamma ray spectrum was fitted by a response function and then the scaling factor  $s_{sum}$  was obtained. Currently, the scaling factor was deduced in 1 MeV energy bin of the excitation energy to get the enough statistics. In other words, the gamma ray data were analyzed applying the gates of 1 MeV width in the excitation energy. Although the excitation energy spectrum covered up to 30 MeV, the branching ratio was deduced just up to the 23-24 MeV energy bin due to the small statistics. More careful analysis would be able to provide the upper limit of the branching ratio even though the fitting seems to be difficult in the higher energy region. The fitting results of the gammma ray spectrum in the  $\text{LaBr}_3$  detectors are summarized in the appendix. The correction factor  $c_{ave.}$  was calculated under the assumption that the gamma ray is emitted isotropically from the GDR in  $^{90}\text{Zr}$ . This assumption is true if the three of magnetic substes ( $m=-1,0,1$ ) of the GDR are populated equally. Under this

assumption, the averaged correction factor was deduced by taking the weighted average for each slot (Fig.3.26). Here, the uncertainty for the correction factor of each slot detector was used as the weight.

The yield of the GDR and the number of simulated gamma rays was large enough and thus their uncertainty was much smaller than 1%. The uncertainty is mainly originated in the scaling factor. The uncertainty of the scaling factor ( $\sigma_s$ ) was obtained when the experimental data was fitted. It was ranged from 1% to 10% below the energy of 20 MeV, while it increased strongly above the energy of 20 MeV and reached 60% in worst case due to the small statistics. The uncertainty of the correction factor ( $\sigma_{corr.}$ ) was just 4% after taking the average which was the second largest uncertainty. Consequently the uncertainty of B.R. ( $\sigma_{BR}$ ) was deduced by

$$\sigma_{BR} = \sqrt{\sigma_s^2 + \sigma_{corr.}^2}. \tag{4.5}$$

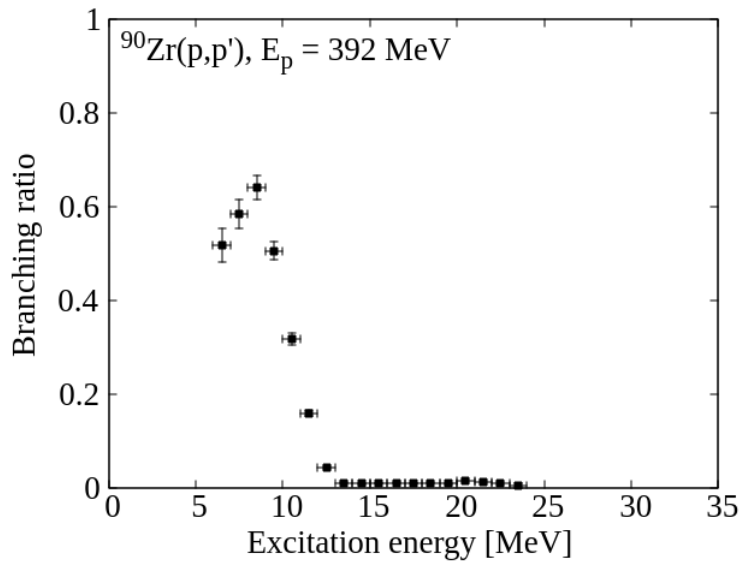


Figure 4.7: Branching ratio of the ground state gamma decay.

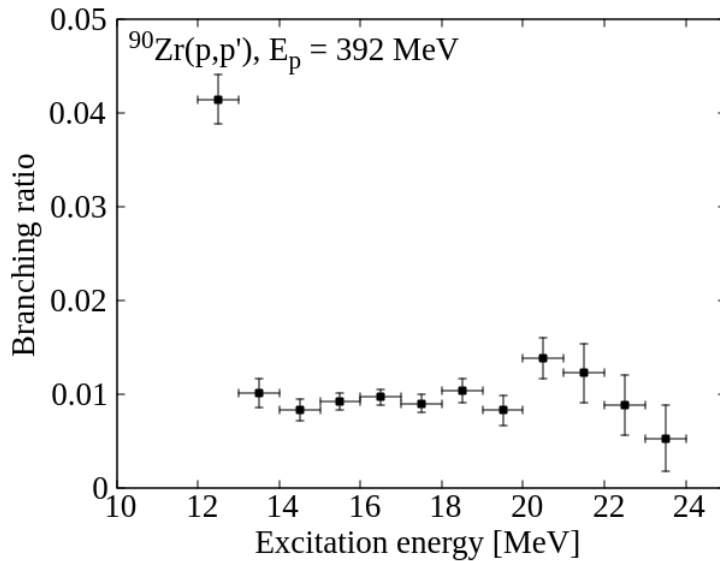


Figure 4.8: Zoomed branching ratio of the ground state gamma decay.

### 4.2.2 Total decay width

The total decay width  $\Gamma$  for a specific energy bin was calculated by

$$\Gamma = \frac{\Gamma_\gamma}{B.R.}, \quad (4.6)$$

where the  $\Gamma_\gamma$  is the averaged gamma decay width to the ground state of the specific energy bin, which is given by

$$\Gamma_\gamma = \frac{16\pi}{9} \left( \frac{E_\gamma}{\hbar c} \right)^3 g_I B(E1), \quad (4.7)$$

where

$$g_I = \frac{2I_0 + 1}{2I_R + 1}, \quad (4.8)$$

$I_0$  and  $I_R$  represent the spins of the ground state and the resonance, respectively. The result is plotted in the Fig.4.9. One may wonder why the decay width can be smaller than 1 MeV even though the data were analyzed in the energy bin of 1 MeV width. This is because I used the averaged  $\Gamma_\gamma$  in each energy bin. On the other hand, the gamma decay data was summed up in each energy bin in order to get more statistics, thus the uncertainty of x axis was fixed at 1 MeV. The present  $\Gamma_\gamma$  may be overestimated because the photo absorption cross section was larger than the reference data. In the present analysis, however, I didn't introduce any correction factor to adjust the photo-absorption cross section. Another way is to include this discrepancy as a systematic uncertainty. Such a systematic uncertainty was also not considered because I would discuss the overall structure of B.R. and the decay width  $\Gamma$ .

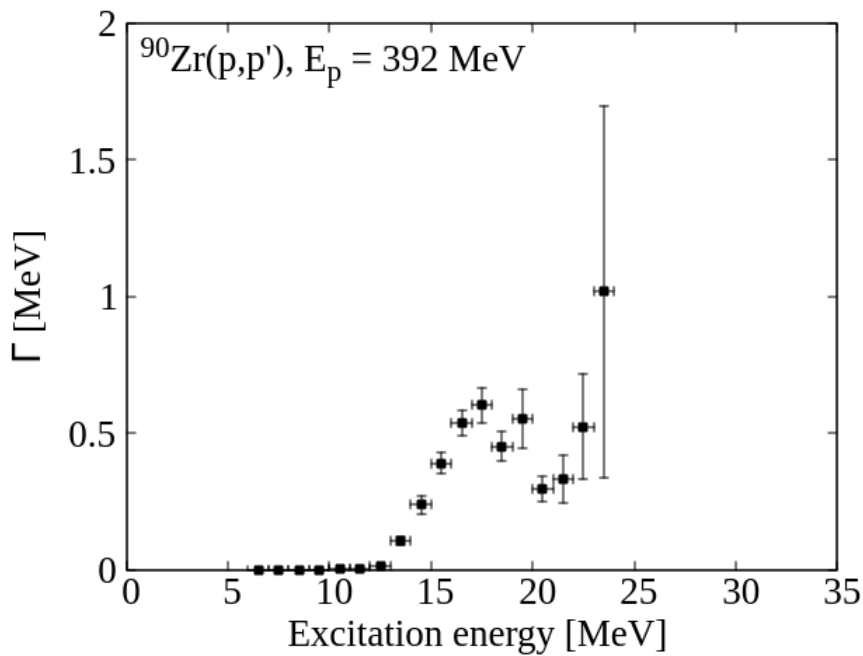


Figure 4.9: Total decay width in the IVGDR of  $^{90}\text{Zr}$ .

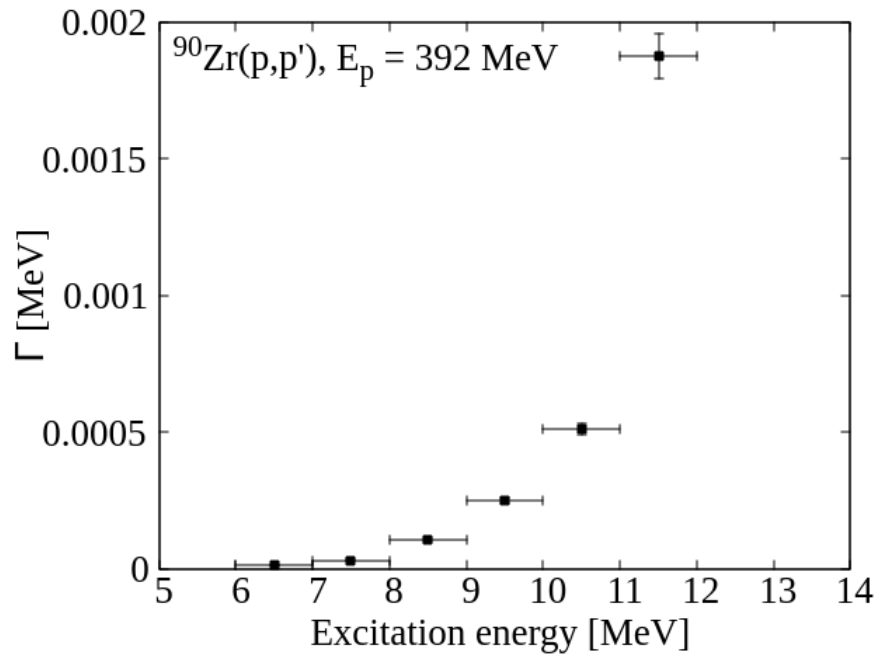


Figure 4.10: Total decay width in the IVGDR of  $^{90}\text{Zr}$  zoomed in the lower energy region.

---

## Chapter 5

# Discussion

### 5.1 Binning effect

The total decay width was obtained by

$$\Gamma = \frac{\Gamma_\gamma}{B.R.} \quad (5.1)$$

However, understanding the meaning of this  $\Gamma$  is not straightforward. What we deduced in the present analysis is the averaged decay width in the specific energy bin. How to incorporate the averaging effect in the analysis is still under discussion. One of possibilities is that the decay width is averaged with a weight of the coulomb excitation cross section. In this thesis, I didn't consider those binning effect. The total decay width obtained from the Eq.5.1 was discussed.

### 5.2 Total decay width

Neutron separation energy and two neutron separation energy in  $^{90}\text{Zr}$  are 11.97 MeV and 21.29 MeV, respectively. Since a transition mediated by the strong interaction is much faster than that by the electromagnetic interaction, the gamma decay branching ratio decreases drastically and the total decay width increases just above each separation energy.

Monotonic increases in the range of 18-21 MeV and 21-24 MeV probably reflect the phase space volume of the decay neutrons. This phase space affects both of the gamma decay width and the total decay width. Thus the branching ratio was almost flat in the GDR region. We can conclude that the Beene's assumption ([BEE90]) that "Branching ratio is flat over the range of the GDR" was correct within the present uncertainty.

Additionally, the fine structure which was seen in only the low energy tail of the spectrum in  $^{208}\text{Pb}$  can be explained by this increase of the width. The width at lower energy in  $^{90}\text{Zr}$  is found to be of the order of 100-400 keV from the present data. This fact is also consistent with the data of  $^{208}\text{Pb}$  (Fig.1.6).

In the higher energy region of the Fig.5.1, a dip can be seen at around 21 MeV. This structure will be discussed in the following section.

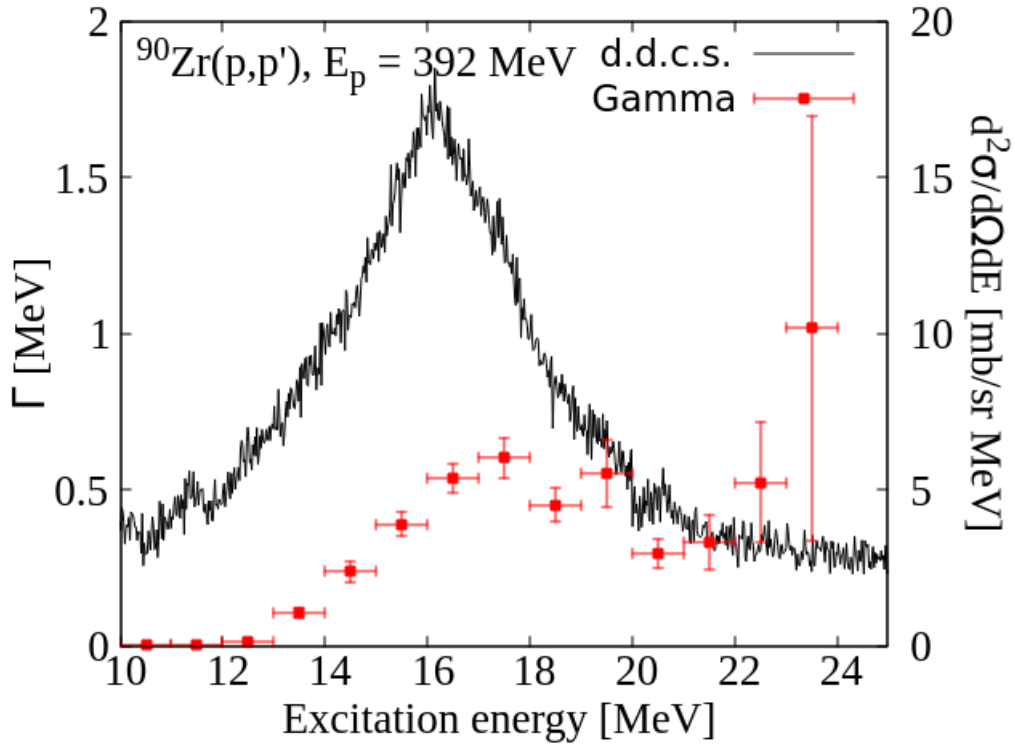


Figure 5.1: Total decay width in  $^{90}\text{Zr}$  and double differential cross section as a function of the excitation energy.

### 5.3 Isospin splitting

Isospin splitting of the IVGDR was predicted by S.Fallieros et al. [FAL65] and B.Goulard et al. [GOU68]. If the isospin of the ground state  $T_0$  is not zero, both of the isospin lower state ( $T_0$ ) and the isospin upper state  $T_0 + 1$  will be populated at the different excitation energy. They predicted the energy difference between them,

$$E_{T_0+1} - E_{T_0} = U \frac{T_0 + 1}{T_0} \approx 6 \text{ MeV, for } T_0 = 5 \quad (5.2)$$

where the  $U \approx 5 \text{ MeV}$  is the symmetry energy for  $A = 90$  nuclei. The transition strength of the isospin upper state was predicted to be 20% of E1 sum rule. In addition to the theoretical predictions, experimental approaches were also performed via proton induced reactions. The neutron decay from the isospin upper state to the isospin lower state of the residual nucleus is forbidden because of the isospin selection rule. Thus  $(\gamma, p)$  and  $(e, e'p)$  reactions are suitable for the research about the isospin upper state. Fig.5.2 and Fig.5.3 show the experimental results of  $^{89}\text{Y}(p, \gamma)$  and  $^{90}\text{Zr}(p, p'\gamma)$ .

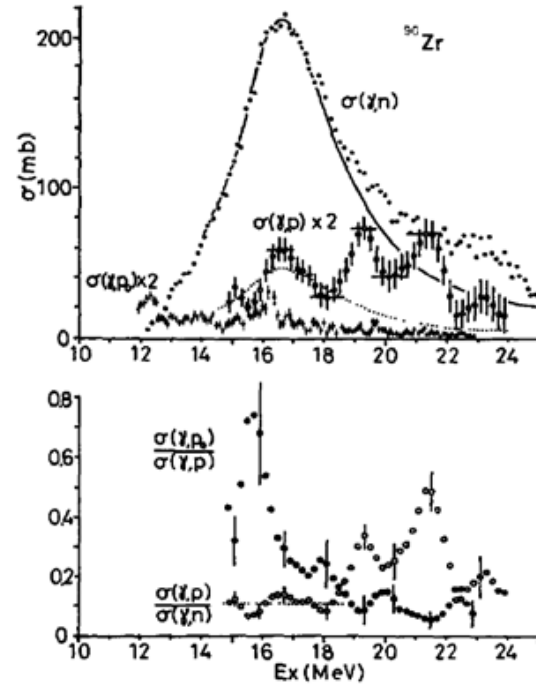
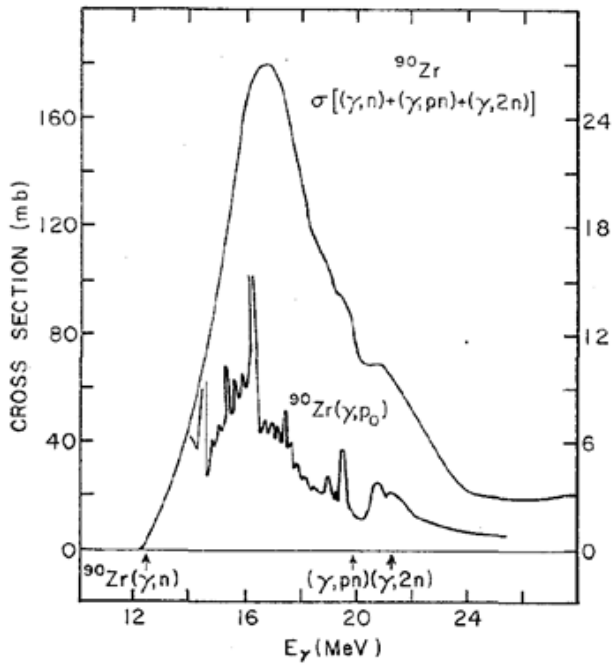


Figure 5.2: Cross section of  $^{89}\text{Y}(p, \gamma)$  reaction. Fine structure in the 14-18 MeV is the isobaric analog states of  $^{90}\text{Y}$ . [HAS73]

Figure 5.3: Cross section of  $^{90}\text{Zr}(e, e'p)$  reaction.  $(\gamma, p)$  means  $(e, e'p)$  and  $(\gamma, p_0)$  is obtained from the data of  $^{89}\text{Y}(p, \gamma)$ .  $(\gamma, n)$  cross section is plotted together for comparison. [SHO75]

Both results show a structure around 20 MeV that is close to the theoretical predicted energy of the isospin upper GDR. The authors indicated that this bump originates from the isospin upper GDR. Compared with our result, this energy corresponds to the dip of decay width spectrum obtained from our experimental data. Actually, neutron decay channel to the isospin upper state of the daughter nucleus is energetically allowed from the 20 MeV (Fig.1.7). Nevertheless, we can suggest the existence of the isospin upper GDR from our results by assuming the following things.

- Around 20 MeV, the phase space of the neutron decay to the isospin upper state of the daughter nucleus is small because the Q value is not large.
- the trend of decay width is like that of the isospin lower GDR.

Then what we see is the weighted mean of the decay width in isospin lower and upper state,

$$\Gamma = \frac{\Gamma_{\gamma<} \Gamma_{<} + \Gamma_{\gamma>} \Gamma_{>}}{\Gamma_{\gamma<} + \Gamma_{\gamma>}}. \quad (5.3)$$

As a result, if the isospin upper state becomes dominant, the averaged width can be smaller. Therefore our results also supports the presence of the isospin upper GDR in  $^{90}\text{Zr}$  at around 20 MeV.

## Chapter 6

# Summary and Outlook

In order to reveal the fine structure of the IVGDR, the branching ratio of the gamma decay to the ground state from the IVGDR in  $^{90}\text{Zr}$  and the total decay width was studied via a coincidence measurement between a proton inelastic scattering and a gamma ray detection.

The ground state gamma decay from the IVGDR was clearly observed thanks to the technical advantages of the  $\text{LaBr}_3$  detectors and the Grand Raiden magnetic spectrometer. In this thesis, the branching ratio and the decay width were obtained in the 1 MeV interval. The branching ratio showed a flat structure (of the order of 1%) in the energy range of 13-20 MeV that corresponds to the isospin lower GDR region. Around the excitation energy of 21 MeV, the branching ratio increases and starts to decrease. This result indicates the existence of the isospin upper GDR as expected by other experiments like  $(p, \gamma)$  and  $(e, e'\gamma)$  reactions. The obtained total decay width increases up to 19 MeV and then decreases till around 20 MeV indicating the isospin upper component as well. After that it increases again.

We succeeded in studying the branching ratio and the decay width of the GDR as a function of the excitation energy for the first time. However, there are the following unsolved problems in the current analysis.

- the obtained  $B(E1)$  increases monotonically in the region of the high excitation energy
- the obtained  $B(E1)$  looks systematically larger than the reference data
- the Geant4 simulation data doesn't reproduce the experimental data precisely
- the result of the carbon target seems fluctuating during the measurement

Furthermore, much more information is expected to be extracted from this experimental data by exploring the following things.

- analysis with finer energy bin
- angular distribution of emitted gamma rays
- the cascade decay from the GDR to the excited states

In conclusion, the gamma coincidence measurement in the region of the GDR was successfully performed. This fact shows a new possibility of the research on nuclear structure.

---

## Appendix A

# Formalism of coulomb excitation

### A.1 Nuclear optical potential

The following nuclear optical potential was used to calculate the virtual photon number in the eikonal approximation. The program code was developed by C. A. Bertulani. This section is based on his code and a published paper [BER02]. The optical potential is obtained in " $t\rho\rho$ " approximation [HUS91] [FES93],

$$U_N^{opt} = \int \langle t_{NN}(\mathbf{q} = 0) \rangle \rho_1(\mathbf{r} - \mathbf{r}') \rho_2(\mathbf{r}') d^3 r', \quad (\text{A.1})$$

where  $\rho_1(\rho_2)$  is the ground state density of nucleus 1 (2) and  $\mathbf{q}$  is the momentum transfer. If the proton is inelastically scattered off the heavy nucleus with enough high energy, the momentum transfer is much small.  $\langle t_{NN} \rangle$  is the isospin averaged transition matrix element for nucleus-nucleus scattering,

$$\langle t_{NN}(\mathbf{q} = 0) \rangle = \frac{Z_1 Z_2 + N_1 N_2}{A_1 A_2} t_{pp}(\mathbf{q} = 0) + \frac{Z_1 N_2 + Z_2 N_1}{A_1 A_2} t_{pn}(\mathbf{q} = 0). \quad (\text{A.2})$$

The transition matrix element for nucleon-nucleon scattering is given by

$$t_{pi}(\mathbf{q} = 0) = -\frac{i\hbar v}{2} \sigma_{pi}, \quad (\text{A.3})$$

where  $\sigma_{pi}$  is the free proton-nucleon cross section.  $\sigma_{pi}$  is deduced to reproduce the elastic scattering data,

$$\sigma_{pp} = 32.7 - 5.52 \cdot 10^{-2} \cdot E + 3.53 \cdot 10^{-7} \cdot E^3 - 2.97 \cdot 10^{-10} \cdot E^4 \quad (\text{A.4})$$

$$\sigma_{pn} = 14.2 + 5436/E + 3.72 \cdot 10^{-5} \cdot E^2 - 7.55 \cdot 10^{-9} \cdot E^3, \quad (\text{A.5})$$

where  $E$  is the incident energy of the projectile. Note that Eq.A.4 and Eq.A.5 are available in the range of  $E = 280 - 840$  MeV and  $E = 300 - 700$  MeV, respectively.

## Appendix B

# Data table

### B.1 Grand Raiden spectrometer

The horizontal scattering angle at the focal plane was obtained by

$$\theta_t = \sum_{i,j}^2 (\theta | x^i \theta^j) x_d^i \theta_d^j. \quad (\text{B.1})$$

Table B.1: Parameters for optical correction of  $\theta_c$ .

$i$	$j$	$(\theta   x^i \theta^j)$
0	0	$1.98924 \times 10^{-2}$
0	1	$-4.36379 \times 10^{-1}$
0	2	$-6.94058 \times 10^{-2}$
1	0	$3.69273 \times 10^{-5}$
1	1	$-1.17320 \times 10^{-5}$
1	2	$-3.07069 \times 10^{-4}$
2	0	$-3.16246 \times 10^{-10}$
2	1	$1.85086 \times 10^{-7}$
2	2	$-9.96895 \times 10^{-7}$

The vertical position  $y$  were corrected by the following equation.

$$y_c = y_d + \sum_{i,j}^2 (y | x^i \phi^j) x_d^i \phi_d^j. \quad (\text{B.2})$$

Table B.2: Parameters for optical correction of  $y_c$ .

$i$	$j$	$(y   x^i \phi^j)$
0	0	$-1.55974 \times 10^0$
0	1	$2.22648 \times 10^3$
0	2	$-8.91293 \times 10^3$
1	0	$1.49201 \times 10^{-2}$
1	1	$-7.13165 \times 10^0$
1	2	$-8.18593 \times 10^1$
2	0	$-4.06521 \times 10^{-5}$
2	1	$1.34701 \times 10^{-2}$
2	2	$-5.34645 \times 10^{-1}$

## B.2 LaBr<sub>3</sub> detectors

The energy scale of the LaBr<sub>3</sub> detectors was calibrated by,

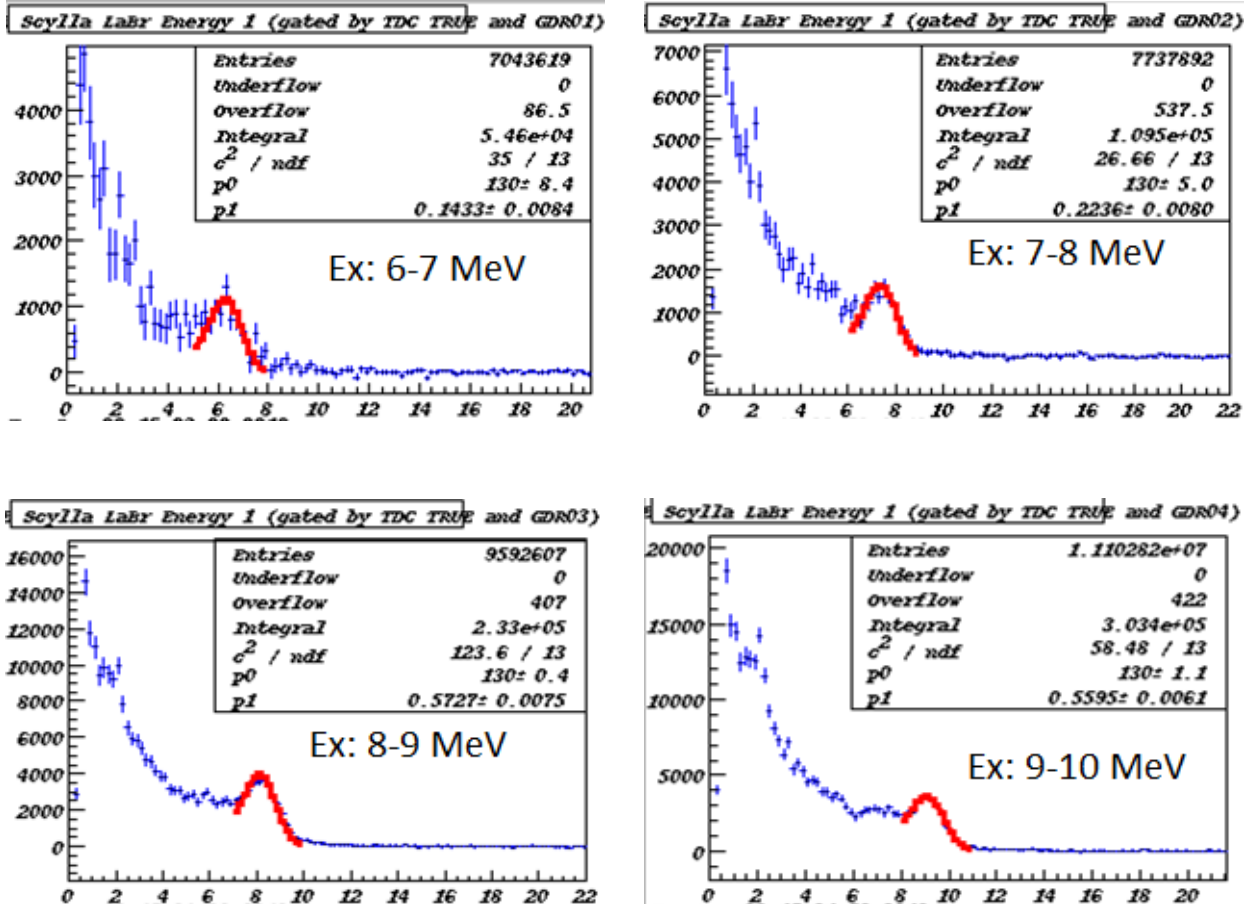
$$E_{\gamma}[\text{MeV}] = a + b \cdot \text{ADC}[\text{ch}] + c \cdot \text{ADC}[\text{ch}]^2. \quad (\text{B.3})$$

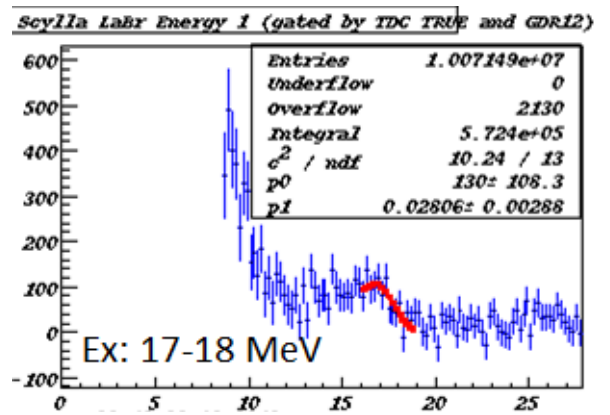
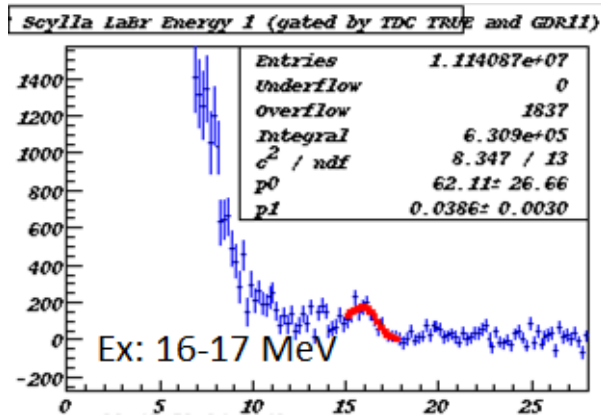
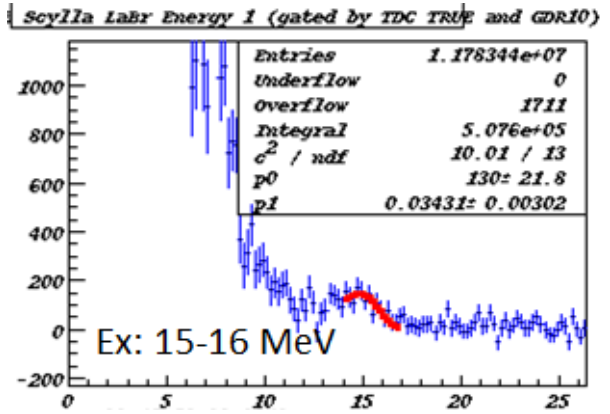
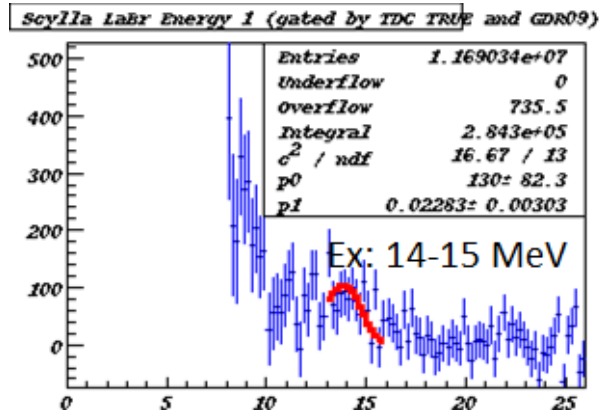
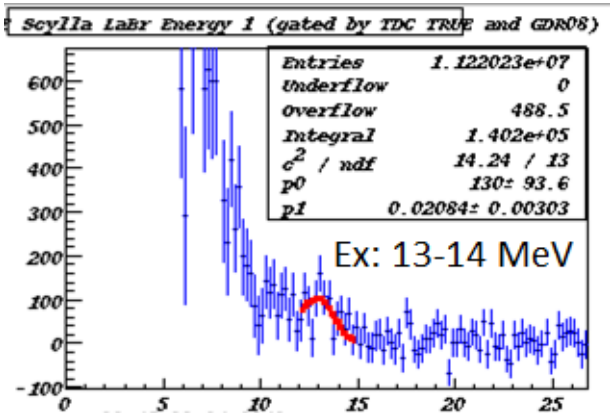
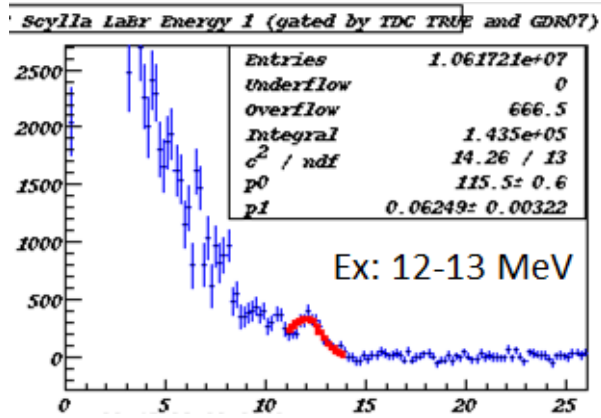
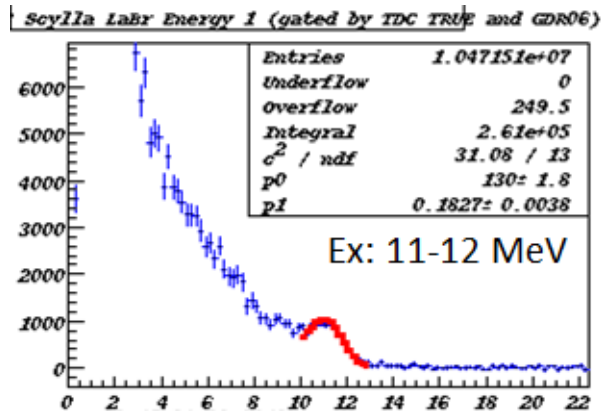
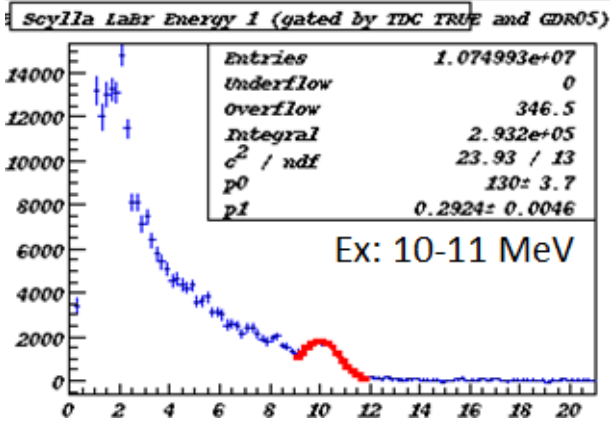
Table B.3: Parameters for energy calibration of LaBr<sub>3</sub> detectors.

slot	a	b	c
1	-192.38	10.78	-0.00025
2	-223.80	11.94	-0.00061
3	-254.75	13.14	0.00009
4	-209.40	11.25	-0.00035
5	-194.49	10.05	0.00039
6	-221.21	11.84	-0.00065
7	-195.09	10.58	0.00022
8	-186.60	9.806	0.00008

## B.3 Coincidence data

Gating on a specific energy bin of excitation energy spectrum, the gamma ray spectrum summed up by all of the detectors was fitted by a simulated response function convoluting with a gaussian. The blue plots are experimental data and the red curve is the fitting function.





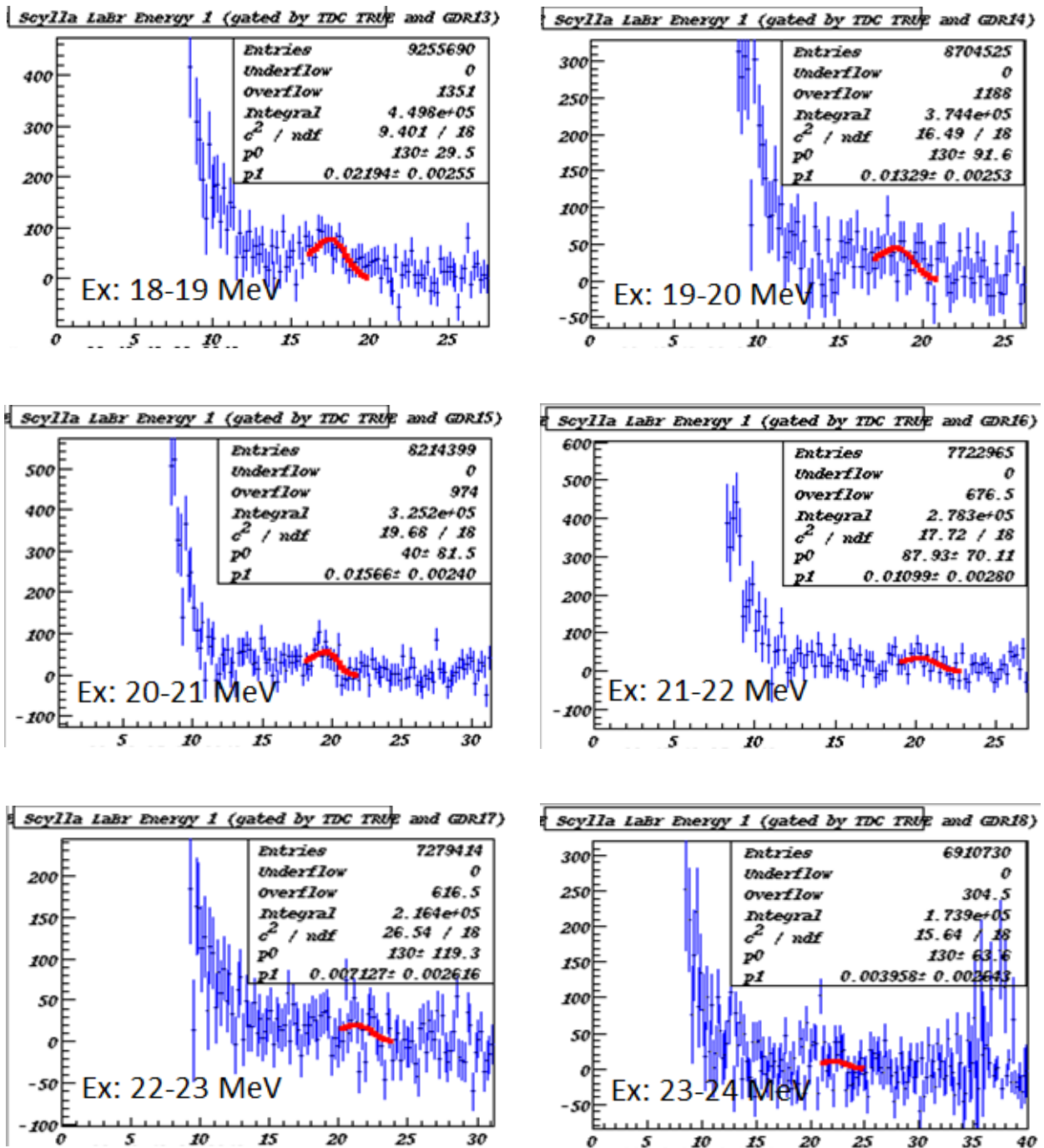


Figure B.1: Fitting result in  $^{90}\text{Zr}(p, p'\gamma)$ . The horizontal axis is gamma ray energy in MeV and the vertical axis is the counts/200 keV.

# Bibliography

- [AGO03] S. Agostinelli *et al.*, Nucl. Instrum. Meth. **A 506** (2003) 250-303.
- [ALL06] J. Allison *et al.*, IEEE Trans. Nucl. Sci. **53** (2006) 270-278.
- [ALL16] J. Allison *et al.*, Nucl. Instrum. Meth. **A 835** (2016) 186-225.
- [BEE90] J.R. Beene *et al.*, Phys. Rev. **C 41** 920 (1990).
- [BER75] B.L. Berman and S.C.Fultz, Reviews of Modern Physics, **47** No. 3, July 1975.
- [BER88] C. A. Bertulani and G. Baur, Physics Reports **163** 5 and 6 (1988) 299-408.
- [BER02] C. A. Bertulani *et al.*, Computer Physics Communications **152** 3 (2003) 317-340.
- [BER09] C. A. Bertulani, Lecture note presented at the 8th CNS-EFES, held at CNS, the Univ. of Tokyo in 2009.
- [BLO94] J. Blomgren *et al.*, Nucl. Phys. **A 578** (1994) 267-284.
- [FAL65] S. Fallieros *et al.*, Phys. Lett. **19** (1965) 398.
- [FES93] H. Feshbach, "Theoretical Nuclear Physics: Nuclear Reactions", (Wiley-Interscience, Portland, 1993).
- [FUJ99] M. Fujiwara *et al.*, Nucl. Instr. Meth. Phys. Res. **A 422**, 484 (1999).
- [GIA13] A. Giaz *et al.*, Nucle. Instr. Meth. Phys. Res. **A 729** (2013) 910-921.
- [GOL48] M. Goldhaber and E. Teller, Phys. Rev. **74** (1948) 1046.
- [GOU68] B. Goulard *et al.*, Phys. Rev. **176** (1968) 1345.
- [HAR01] M. N. Harakeh and A. van der WOUDE, Giant Resonances Fundamental High-Frequency Modes of Nuclear Excitation (Oxford University Press, 2001)
- [HAS73] M. Hasinoff *et al.*, Nucl. Phys. **A216** (1973) 221-249.
- [HUS91] M. S. Hussein *et al.*, Phys. Reports **201**, 279 (1991).
- [IWA12] C. Iwamoto *et al.*, Phys. Rev. Lett. **108**, 262501 (2012) 1-4.
- [KEL17] J. H. Kelly *et al.*, Nucl. Phys. **A 968** (2017) 71-253.
- [KNO10] Glenn F. Knoll, Radiation Detection and Measurement 4th Edition (2010).
- [MAR13] D. Martin, Master thesis, Technische Universitat Darmstadt (2013).
- [OUI17] I. Ou, Ph.D. thesis, Okayama University (2017).

- [POO12] C. M. Poole *et al.*, *Australasian Physical and Engineering Science in Medicine* **35** 3 (2012) 329-334.
- [SHO75] K. Shoda *et al.*, *Nucl. Phys. A* **239** (1975) 397-411.
- [TAM00] A. Tamii, Ph.D. thesis, Kyoto University (2000).
- [TAM09] A. Tamii *et al.*, *Nucl. Instr. Meth. Phys. Res. A* **605**, 326 (2009).
- [TAM11] A. Tamii *et al.*, *Phys. Rev. Lett.* **107** (2011) 062502.
- [WIN79] A. Winther and K. Alder, *Nucl. Phys. A* **319**,(1979) 518-532.

## Acknowledgments

本研究の遂行及び論文執筆にあたり、多くの方々のお世話になりました。

指導教官である民井准教授には、検出器架台の設計から実験準備、そして実験・解析、さらには修士論文執筆までの全てにおいて大変お世話になりました。普段からも、原子核どころか物理すら理解の怪しい私のどんな質問にも真摯に答え又議論してくださり、物理や研究の奥深さを教えていただきました。また、海外を含む多くの学会へ参加させていただき物理以外にも本当に多くのことをこの二年間で学ばせていただきました。大変感謝しています。

小林助教授には同じ部屋ということもあり、物理や解析方法などの非常に初歩的な質問ばかり聞いてしまいましたが、いつも分かりやすく丁寧に教えてくださりました。実験準備中も、神経質な私のアラインメント作業に深夜遅くまで付き合ってくださいました。特に、コーディングに関して全くの素人であった私が解析を進めていく上で、小林助教授とそのホームページは本当に不可欠の存在でした。

井上さんには、BRILLIANT 実験を通して、研究に対する姿勢を身を持って教えていただきました。思えば、神戸大学、理研、原研と多くの実験施設で実験をしました。そのたびに井上さんの粘り強い不屈の精神には圧倒され、その姿に感服するばかりでした。

I'd like to thank Aga and Johann, you helped me a lot during the test experiment on December of 2017. Both of you gave me advice about the data analysis and the Geant4 simulation. I'd like to thank Zaihong, your comments in the group meeting was always essential and make me realized my mistake.

I wish to give a great thank for all of RCNP-E498 collaborators. Without your help, this research never be succeeded. I'd like to thank Franco from Milano for giving me advice about the LaBr<sub>3</sub> detector. Lindsay and Kevin from iThemba, thank you for your hard work during the experiment. I also would like to thank Lindsay to teach me the Overleaf. I'm writing this thesis with the Overleaf. Kevin helped me to introduce the CAD file into the Geant4 simulation and guided me to the Capetown.

藤田浩彦さんには、特にビームチューニングの際その豊富な経験をもとに大いに助けていただきました。私が南アフリカに行く際にはアドバイスをくださったたり、貨幣を貸してくださったたりと実験以外にもお世話になりました。藤田佳孝さんは、豊中に行ったときにいつも巨大共鳴やクロン励起について基礎基本から大変わかりやすく教えていただきました。特に巨大共鳴の幅についての議論は、二年間ずっと抱えていたわだかまりを払拭する大変有意義なものでした。東大 CNS の岩本さんには、実験準備からビームタイムまで、トラブルに遭遇したときにいつも的確な助言をいただきました。ビーム強度を思った以上に上げられなかったときに厚い標的を使うことを勧めてくださったおかげで十分な統計を貯めることができました。立教大の梅野さんには、LaBr<sub>3</sub> 検出器のセットアップやガンマ線検出効率のシミュレーションに関して多くの助言をいただきました。

岡山大の須藤君と Mandeep、立教大の藤野君には実験準備初日からビームタイム後の片付けまでかなり働いてもらいました。須藤君にはオンライン解析をお願いしたり、藤野君には回路まわりを丸投げしたり、頼りすぎてしまいましたが二人のおかげで何とか実験を成功させることができました。本当にありがとうございました。

四年生のときから同じ研究室だった堀君と柳原君、いろいろとありましたがなんとか一緒に卒業できそうで良かったです。倒れるまで頑張り続ける堀君とどんなときでも冷静な柳原君という両極端のふたりと同期だったおかげでいい思い出がたくさんできました。ありがとう。大学院から同じ RCNP 所属になった甲田君、山本さん、Tung 君、加速器の森田君、理論の兵藤君と藤井君は同期としてときには楽しく飲み、ときには互いに刺激し合える仲間でした。ありがとう。一年間同室

だった教務補佐員の古野さんにはお昼ご飯に誘っていただきありがとうございました。また、反応論ゼミに参加してくれた、M1の廣本君、吉川君、Wang君、D1のChangさんや他大学の方々、有意義で楽しい物理の時間をありがとうございました。ゼミで学んだことは本論文執筆にあたり大いに役立ちました。みなさんにとってもこのゼミで学んだことがいつか役に立つことを願っています。そしてそのきっかけを与えてくださった坂口さん、本当に感謝しています。

その他にもここには書ききれない、非常に多くの方々との出会いや支えがあってここまで来られました。みなさま、ありがとうございました。